Christian Sterwerf

Magnetic compounds for improving spintronic applications

Ferromagnetic Heusler compounds and antiferromagnetic oxides

Bielefeld University
Department of Physics

Magnetic compounds for improving spintronic applications

Ferromagnetic Heusler compounds and antiferromagnetic oxides

Christian Sterwerf

Printed on non-aging paper ISO 9706

Bielefeld University
Department of Physics

Doctoral thesis
December 12, 2016

I wrote this thesis by myself and used none but the indicated resources. Text and figures were partly taken from corresponding publications, which originate directly from this work.

Reviewers:

Prof. Dr. Günter Reiss
Prof. Dr. Thomas Huser

Contents

1 Introduction 1

2 Fundamentals 5
- 2.1 Magnetic Ordering . . . 6
- 2.2 Ferromagnetism . . . 9
- 2.3 Exchange Bias . . . 11
- 2.4 Magnetoresistance . . . 22
- 2.5 Magnetization Dynamics in Ferromagnets . . . 25
- 2.6 Ferroelectrics . . . 26

3 Materials 31
- 3.1 Co- and Fe-Based Heusler Compounds . . . 31
- 3.2 Perovskites . . . 34

4 Analytical and Preparation Tools 43
- 4.1 Thin Film Deposition . . . 44
- 4.2 Structural Characterization . . . 45
- 4.3 X-Ray Absorption Techniques . . . 49
- 4.4 Magneto-Optic Kerr-Effect . . . 52
- 4.5 Ferromagnetic Resonance . . . 55

5 Magnetization Dynamics in Co-Fe-Si Films 59
- 5.1 Sample Preparation . . . 59
- 5.2 Crystallographic Properties . . . 61
- 5.3 TMR Effect In Co-Fe-Si-Based Magnetic Tunnel Junctions . . . 62
- 5.4 Magnetization Dynamics . . . 63
- 5.5 Conclusion . . . 69

6 Exchange Bias in Bismuth and Lanthanum Ferrites 71
6.1 Exchange Bias in $BiFeO_3$/Co-Fe Systems 72
6.2 Exchange Bias in $LaFeO_3$/Co-Fe Bilayers 84
6.3 Comparison between $BiFeO_3$/Co-Fe and $LaFeO_3$/Co-Fe Systems 101

7 Conclusion & Outlook 103

A Deformation Mode Transitions in Amorphous - Cu45Zr55/ Crystalline - Cu Multilayers 107
A.1 Preparation and Characterization Techniques 108
A.2 Theoretical Approach 110
A.3 Crystallographic Structure 110
A.4 Mechanical Behavior 111
A.5 Theoretical Modeling 114
A.6 Conclusion 116

B Bibliography 117

C Publications and Conferences 127

D Acknowledgements 129

1 Introduction

Today's fast and reliable storage of data in electronic memories is one of the fundamental keys to the success of modern computing technologies. While conventional electronics only us the electron's charge for data storage, the field of spintronics exploits the intrinsic spin of the electron as an additional degree of freedom.

Spintronics[1] was born in the 1980s when spin-dependent conductivity in solids was found. Particularly, Grünberg's[2] and Fert's[3] discovery of the GMR effect attracted a lot of interest. Later, the tunneling magnetoresistance[4] (TMR) effect was observed. Both magnetoresistance effects were used as read-out techniques in memories such as read heads of hard drives. However, these devices contain mechanical moving parts, making them prone to errors, relatively slow, and less energy-efficient. Promising candidates for the current replacement of hard drives containing mechanical parts include the magnetoresistive random-access memory[5] (MRAM), which is at an early stage of development. Basically, an MRAM consists of a magnetic tunnel junction (MTJ) in which a tunneling magnetoresistance (TMR) effect can be observed. The MRAM cell can be written by the application of a magnetic field in order to switch the magnetization direction of the magnetic electrodes. A further improvement allows magnetization switching through the use of a spin current-assisted switching[6] in spin-transfer torque MRAMs (STT-RAMs). The first commercial application of a STT-MRAMs with a capacity of 64 Mb was released by Everspin Technologies in 2012[7].

An MTJ, the building block of an MRAM, consists of different magnetic materials fulfilling different tasks. In general, MTJs contain a ferromagnetic layer with a soft switching behavior as a switchable spin-injector and a second ferromagnetic layer with a hard switching behavior that acts as a spin detector or

reference layer. For a reliable and accurate read-out of the magnetic state of the two layers, i.e. parallel and antiparallel, the magnetization of this reference layer is fixed by the exchange bias effect induced by an adjacent antiferromagnetic layer. Hence, improved ferromagnetic materials are needed for realizing high effect amplitudes and advanced antiferromagnets are necessary for an efficient exchange bias.

Moreover, antiferromagnetic materials posses the advantage that the orientation of the antiferromagnetic sublattices is nearly unaffected by externally-applied magnetic fields. Hence, a new emerging field is antiferromagnetic spintronics[8]. This new field investigates effects that allow for data storage without the use of ferromagnets but with antiferromagnets, which also influence the spin transport. Since external magnetic fields do not alter the orientation of the magnetic moments in antiferromagnets, alternative techniques have to be found that fulfill this task.

It was recently reported that for ferroelectric $BiFeO_3$ films the antiferromagnetic plane can be switched by the application of an electric field, as the antiferromagnetic ordering is coupled to the antiferromagnetic ordering of the crystal. This leads to the idea of the ferroelectric RAM (FeRAM), which is also a potential future non-volatile memory that is currently in the early stage, like the MRAM. It is very similar to the DRAM, but uses a ferroelectric layer in which the information is stored by the direction of the spontaneous polarization. Cypress Semiconductor introduced the first 4 Mb FeRAM in 2015[9].

The combination of ferroelectrics and the TMR attracted tremendous attention, as ferroelectric materials in magnetic tunneling junctions[10,11] (FTJ) lead to high signal amplitudes, allowing for non-volatility and the possibility of small device sizes and a low power consumption. This makes FTJs interesting for their application in future memories.

This thesis aims to find new materials for the improvement of spintronic applications. In particular, two types of materials are investigated in detail: ferromagnetic Heusler compounds and ferroelectric and antiferromagnetic oxides.

The first part of this thesis presents the results of a stoichiometric series of Heusler compounds ranging from Co_2FeSi to Fe_2CoSi. Many Heusler compounds are reported to be half-metallic[12] and, thus, produce a high tunneling magnetoresistance (TMR) effect. By a successive substitution of Co with Fe atoms, the electronic and magnetic properties of the Heusler compounds can be tailored, as the changed number of electrons in the system produces a shift of the Fermi energy in the gap. The investigation of MTJs based on the Co-Fe-Si films was the part of a previous work[13] and are published in Reference[14]. High TMR ratios were found for all stoichiometries. This thesis summarizes

the results as high-effect amplitudes are essential for an accurate read-out of stored information. In this work, ferromagnetic resonance technique (FMR) is used to investigate the magnetization dynamics, including a determination of the magnetization damping parameters of the Co-Fe-Si Heusler films. The damping parameters are crucial for devices used in STT-MRAMs during the switching processes, as low damping parameters will lead to low switching current densities. These findings are discussed with regards to their applicability in spintronic devices. The according results have been recently published in Reference[15].

The second part of the document deals with ferroelectric and antiferromagnetic $BiFeO_3$ and $LaFeO_3$ films, grown by reactive sputtering from elemental Bi, La, and Fe targets. Each section describing these materials starts with a presentation of the preparational details along with the optimization of the crystallography of the films. Afterwards, detailed investigations of the ability of the $BiFeO_3$ and $LaFeO_3$ films to induce an exchange bias in a coupled ferromagnet are presented, along with a discussion about the integration ability of $BiFeO_3$ and $LaFeO_3$ films into commercial devices. Furthermore, a GMR device containing a $LaFeO_3$ layer is presented. The results of the investigations on the $BiFeO_3$ films are published in Reference[16].

This thesis is organized as follows: in the second chapter the theoretical background is explained. This chapter contains an overview of the most common models for describing ferromagnetism and the exchange bias effect. Furthermore, an introduction to the AMR and GMR effects is given, as well as a fundamental explanation of the magnetization dynamics in ferromagnets and an introduction to ferroelectrics. In Chapter 3 the investigated materials, i.e. the Co-Fe-Si Heusler compounds and the $BiFeO_3$ and $LaFeO_3$ films, are introduced, along with their crystal structure. Moreover, their electronic structures, such as the density of states (DOS) and the magnetic properties, are presented. In the fourth chapter the analytical and preparation tools that are used to determine the aforementioned properties are presented. Here, the focus lies on thin film deposition techniques, the structural characterization with various X-ray techniques, and magnetization measurements including X-ray absorption techniques and the magneto-optic Kerr effect. For the determination of the magnetization dynamics, the ferromagnetic resonance technique is introduced. The fifth chapter will present the results of the measurements of the Co-Fe-Si Heusler films with a focus on the magnetization dynamics. Furthermore, the results of MTJs containing Co-Fe-Si films as electrodes are given. Chapter 6 regards the preparation of single-crystalline $BiFeO_3$ and $LaFeO_3$ films followed by detailed investigations of the exchange bias effect induced by the $BiFeO_3$

and $LaFeO_3$ films. A conclusion of the investigated thin films along with an outlook for future work will complete the investigation. Finally, the Appendix will present a study that was conducted during a two-month stay in the course of a summer internship program at the MINT Center at the University of Alabama, Tuscaloosa, USA, in 2014.

2 Fundamentals

In this chapter the underlying physical basics of this study are briefly presented in order to offer a complete understanding of the researched magnetic thin films and their investigation techniques. This chapter is organized as follows: In the first part a simple model for the description of a ferromagnet is introduced, including the impact of an externally-applied magnetic field on the magnetization. Afterwards, magnetic anisotropies are introduced with a focus on unidirectional anisotropies, which can be induced in ferromagnets that are coupled to an antiferromagnetic layer. Several theoretical models for the explanation of the exchange bias effect in crystalline exchange biased systems will be presented, as the complexity of the exchange bias effect makes it necessary to introduce a variety of models - each of which addresses a different effect observed in exchange biased systems. Altogether, this forms a complete description of the exchange bias effect. As it will be shown, although this effect is often exploited in commercial devices, microscopically it is not completely understood yet[17,18].

In the first part of this chapter only magneto-static effects are introduced. For spintronic devices, particularly for spin-transfer torque-based memories, the magnetization dynamics are of significant interest. Hence, in the second part of the chapter the physical background for the description of the precessional motion of the magnetic moment is introduced. This description forms the basis for the ferromagnetic resonant technique that is applied to study the magnetization dynamics of thin $Fe_{1+x}Co_{2-x}Si$ films.

In addition to magnetization switching induced by an external field or exploiting spin-torques, the magnetic properties of ferromagnetic films can also be influenced by employment of the coupling between the ferroelectric and ferromagnetic properties in ferroelectric materials. Zhao *et al.*[19] reported such magnetization switching in ferroelectric $BiFeO_3$ films. Since in this thesis

ferroelectric $BiFeO_3$ and $LaFeO_3$ films[20,21] are also investigated, the physical background of ferroelectricity is briefly discussed in the chapter's last section.

2.1. Magnetic Ordering

As the main topic of the present dissertation is the preparation and investigation of various magnetic materials, this section will introduce the fundamental origin of different magnetic orderings[22,23]. In this thesis two types of magnetic materials are investigated: ferromagnetic Heusler compounds and antiferromagnetic oxides.

In solids, the magnetism originates either directly from the properties of the electrons or are responsible for the type of coupling between magnetic ions. The main contribution to the magnetic moment of an electron is given by the intrinsic spin angular moment. Another contribution is due to the electrons' orbital angular moment, which is caused by the motion of the electrons in the presence of the nucleus. The orbital interaction between the atoms define the magnetic ordering as magnetism is a collective phenomenon.

Different mechanisms can be made responsible for defining the magnetic ordering. The most important of these are presented below.

2.1.1. Superexchange

An important coupling mechanism that is used to describe the orientation of located magnetic spins is the superexchange coupling. This can often be found in oxides in which the indirect magnetic arrangement of two metallic nearest-neighbor cations is caused by superexchange via a nominally non-magnetic

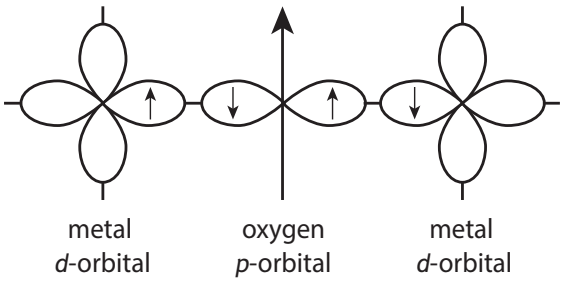

Figure 2.1 | The *d*-electrons of two metal cations are coupled via superexchange over the *p*-orbital of an oxygen atom, resulting in an antiparallel alignment of spins.

anion, for example O^{2-} or Mn^{2+}, as illustrated in Figure 2.1. The 3*d*-orbitals of the metal ions overlap with the 2*p* orbitals of the insulator's ion. The occupied *d*-orbital induces a polarization in the *p*-orbital of the neighboring non-ferromagnetic ion, which influences the spin direction of the next metallic ion (under the consideration of the Pauli Exclusion Principle). This usually results in a strong antiferromagnetic ordering when the bond angle between anion-cation-anion is reduced to 120°-180°.

2.1.2. Direct Exchange

A more generalized model also based on localized spins for the description of the magnetism in solids is discussed in this section. This model is mostly used for the description of the magnetism in insulators rather than metallic materials. It describes the orbital overlap of neighboring electron spins located in the crystallographic lattice structure. The resulting solid's magnetism can be described by a Hamiltonian. Together with the Pauli exclusion principle, the exchange Hamiltonian in the Heisenberg model for a many-electron system can be written as an interaction of the electrons with spin $\mathbf{S}_i$ and $\mathbf{S}_j$:

$$H_{ex} = -2 \sum_{i<j} J_{ij} \mathbf{S}_i \mathbf{S}_j, \tag{2.1}$$

where J_{ij} denotes the exchange constant and $\mathbf{S}_i$ and $\mathbf{S}_j$ are dimensionless spin operators. The sign of the exchange constant J_{ij} determines the direction of the ordering of both spins: for $J < 0$ the ground state of the spins is antiferromagnetic and for $J > 0$ it is ferromagnetic. The exchange constant can be expressed in terms of the interatomic distance *r* divided by the radius of the partially-filled

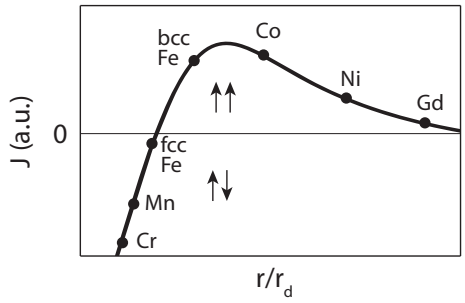

Figure 2.2 | The Bethe-Slater-curve: The exchange integral *J* as a function of the interatomic distance *r* divided by the partially filled orbital r_d. The arrows indicate the energetically-favorable spin alignment.

orbital r_d. This gives the Bethe-Slater-curve, illustrated in Figure 2.2. As this model takes only the localized electrons into account, the following section will present a another model which will describe the magnetism caused by itinerant electrons.

2.1.3. Band Magnetism

As the models presented above are mostly applied to insulating materials with localized materials, this section will introduce the ferromagnetic ordering of metals like Fe, Co and Ni. In these materials the $3d$-electrons are weakly localized and can move as itinerant electrons in the solid's conduction bands. In the case of a paramagnetic metal, both, the spin-up and the spin-down bands of the electrons are equally filled with electrons.

As the electrons feel a Coulomb potential of the ions as well as the other electrons, it can be energetically more favorable for the electrons to flip their spin, leading to an unequal occupation of the bands. This results in an increase of the molecular field and leads to a permanent magnetic moment. For the unequal occupation of the bands and, thus, for the formation of the ferromagnetic ordering, the following condition - also referred to as Stoner criterion - has to be fulfilled:

$$UN(E_F) \geq 1, \tag{2.2}$$

where $N(E_F)$ represents the density of states at the Fermi energy and U is the Coulomb Exchange Interaction.

In addition to these models for an antiferromagnetic or ferromagnetic ordering, there are other exchange interactions, for example the Ruderman-Kittel-Kasuya-Yosida (RKKY)[24–26] or the Dzyaloshinskii-Moriya interaction[27,28]. The RKKY interaction is one main coupling mechanism found in spin glasses. Moreover, this interaction is intentionally used in GMR sensors to obtain an antiparallel magnetization alignment of the electrodes. The Dzyaloshinskii-Moriya interaction, for example, leads - in antiferromagnetic $BiFeO_3$ films - to a small ferromagnetic moment due to a canting of the antiferromagnetic spins.

The following section will focus on the ferromagnetic ordering in ferromagnets as well as the presence of energetically-favored axes.

2.2. Ferromagnetism

As one main topic of this work deals with the investigation of anisotropies in ferromagnets, this chapter introduces the different kinds of anisotropies and their origin. The section starts with the description of a simple isotropic ferromagnet and its response to an external magnetic field.

2.2.1. Zeeman Energy

In the case of a simple ferromagnet, all spins are aligned in a parallel manner in such a way that the magnetic free energy is minimized. In an isotropic ferromagnet, its magnetization $\vec{M}$ can point in every direction. The magnetic free energy, known as Zeeman energy, is given by:

$$F_Z = -\mu_0 \vec{H} \vec{M}, \tag{2.3}$$

where $\vec{H}$ describes an externally-applied magnetic field. Consequently, the ferromagnet is more stable in a parallel alignment of magnetization $\vec{M}$ and applied field $\vec{H}$. Such an isotropic ferromagnet is a theoretical assumption and, thus, the following section will introduce the presence of various anisotropies.

2.2.2. Magnetic Anisotropy

Since the focus of this work is on the properties of single-crystalline films and exchange biased ferromagnets, the following sections will introduce magnetic anisotropies[29] that lead to a distribution of more favorable directions of magnetization $\vec{M}$. Magnetic anisotropy is defined as the interplay between the spontaneous magnetization direction of a material and internal contribution to the magnetic free energy. As a result, some directions of the spontaneous magnetization are more preferred than others in the absence of an applied magnetic field. The preferred directions are called magnetic easy axes, while the undesirable ones are called magnetic hard axes. The presence of magnetic anisotropy can have different origins. The main contributions are of intrinsic origin due to spin-orbit interactions on the atomic scale in a crystal (magnetocrystalline anisotropy) or due to contributions of the demagnetization field to the free energy due to the thickness and shape of the magnetic material (magnetic shape anisotropy).

Mathematically, the magnetic anisotropy energy is defined as the derivative of the free energy F. For a constant temperature and $\mathrm{d}F = \mathrm{d}W - S\mathrm{d}T$, it is $\mathrm{d}F = \mathrm{d}W$. Hence, the change of the free energy F is equal to the change of the

work that is needed to drag the magnetization away from the direction of the magnetic easy axis. The Gibbs free magnetic energy is defined as the sum of the Zeeman energy (Equation 2.3) and contributions of the cubic, uniaxial and unidirectional anisotropy energies:

$$F_{ges} = F_Z + \sum_j F_j \text{ with } j = \text{cub, ua, ud.} \tag{2.4}$$

The anisotropy energies are defined as follows[30]:

- For a cubic or fourfold anisotropy distribution, i.e., the presence of two energetically-favorable axes, the free energy per unit volume can be written as a power series. After neglecting the angle-independent as well as the small terms, it is given by:

$$F_{\text{cub}} = -\frac{1}{2}K_4(\alpha_1^4 + \alpha_2^4 + \alpha_3^4), \tag{2.5}$$

  where K_4 is the cubic magnetic anisotropy constant and α_1, α_2, and α_3 are the directional cosines of the magnetization vector $\vec{M}$ ($\alpha_i = \frac{\vec{M}}{M} \cdot \hat{e}_i$) for all directions according to the coordinate system in Figure 2.3. These are defined as follows:

$$\begin{aligned} \alpha_1 &= \sin\theta_M \cos\varphi_M \\ \alpha_2 &= \sin\theta_M \sin\varphi_M \\ \alpha_3 &= \cos\theta_M. \end{aligned} \tag{2.6}$$

- If one favorable magnetic axis is present, a uniaxial anisotropy distribution is found and the magnetic free energy is:

$$F_{\text{ua}} = K_{\text{ua}} \sin^2\varphi \tag{2.7}$$

  with the uniaxial anisotropy constant K_{ua} and the angle φ between the direction of the easy axis and the magnetization direction.

- One favorable direction of the magnetization $\vec{M}$ corresponds to a unidirectional anisotropy distribution and the magnetic free energy becomes:

$$F_{\text{ud}} = -K_{\text{ud}} \cos\varphi, \tag{2.8}$$

  where K_{ud} represents the unidirectional anisotropy constant with φ as defined above.

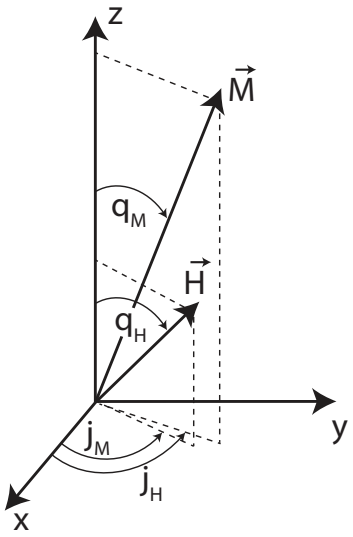

Figure 2.3 | Coordinate system with definitions of the angles with respect to the magnetization $\vec{M}$ and the externally-applied magnetic field $\vec{H}$.

A unidirectional anisotropy can be induced in ferromagnetic layers, which are in contact with an antiferromagnetic material after cooling in a magnetic field. The exchange coupling of interfacial spins results in a shift of the hysteresis parallel to the direction of the applied magnetic field. This is referred to as exchange bias. As this is another main topic of the present thesis, it will be addressed in detail in the following section.

2.3. Exchange Bias

This section presents different models in order to describe the exchange bias effect. Although much progress has been made in this topic, it is still not fully understood microscopically[17,18]. Exchange biased ferromagnetic layers play an important role as reference layers in various spintronic applications, such as for read head in hard drives or MRAMs. This has been observed in many magnetic bilayers by different groups and the research about exchange bias effects is ongoing, with a particular focus on an improved and precise theoretical description that offers a better agreement with experimental results.

This first section introduces an intuitive picture for the observation of the exchange bias effect that was proposed with the discovery of this effect. Afterwards, improved models will be presented in order to address all the observed

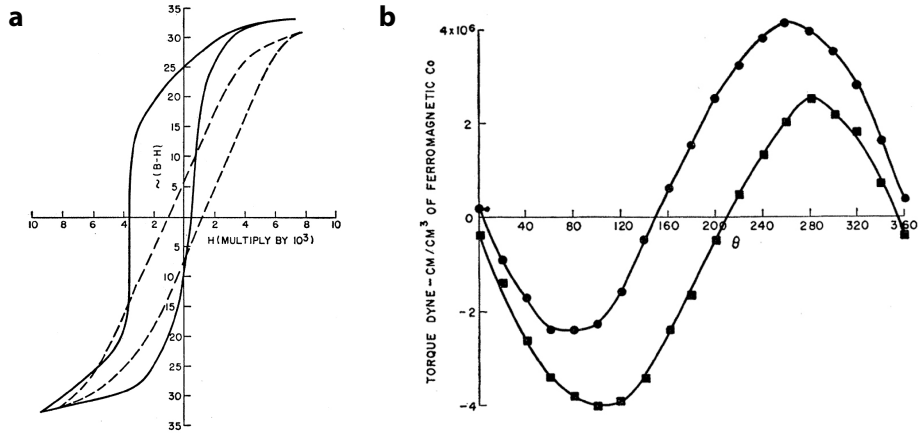

Figure 2.4 | a Original hysteresis by Meiklejohn and Bean of fine CoO nano particles after field cooling in a magnetic field of 10 kOe (solid line) and without field cooling (dashed line) at 77 K. **b** Torque magnetometry measurements of CoO particles at 77 K as a function of the angle between field cooling and the measurement direction for clockwise and counter clockwise rotation, respectively.[1]

effects in crystalline exchange biased bilayer systems. There are many detailed reviews on this topic, for example by Nogués *et al.*[17], Berkowitz *et al.*[18], and Radu *et al.*[31].

In 1956 Meiklejohn and Bean reported a new type of magnetic anisotropy for oxidized Co particles[32,33], for which they observed a shift of the magnetic hysteresis fields after cooling in a magnetic field (in the following this procedure is called field-cooling). They denoted it as exchange anisotropy and concluded that this effect results from an interaction between the ferromagnetic and the antiferromagnetic material[32,33]. The investigated Co particles were nanometer-sized ferromagnetic Co particles (≈ 20 nm) that were exposed to air and therefore contained a cobaltous oxide shell. The formed CoO is antiferromagnetic with a Néel temperature of 293 K. The measurement of the shifted magnetic hysteresis after field-cooling is displayed in Figure 2.4a with the solid line, while the measurement without cooling in an external field did not exhibit a shifted hysteresis, as shown by the dashed line in Figure 2.4a. In addition to the loop shift, the hysteresis after field-cooling shows an enhanced coercivity. Both

[1] Reprinted figure with permission from W. H. Meiklejohn and C.P. Bean, Physical Review, 105, 904 (1957). Copyright 1957 by the American Physical Society.

effects - a shifted hysteresis loop along with an increased coercivity - are denoted as the exchange bias effect.

Furthermore, Meiklejohn and Bean observed a unidirectional anisotropy in torque magnetometrie measurements of the CoO particles of the function $K_u \cos\theta$, where θ is the angle between magnetization and the unidirectional anisotropy axis. Instead, for pure Co particles a uniaxial $K_{ua} \sin(2\theta)$ dependence is expected. Figure 2.4b presents the torque magnetometry measurements of CoO particles at 77 K. Meiklejohn *et al.* proposed that this observed effect is caused by a coupling between the core of the Co particle and the antiferromagnetic oxide, as the exchange bias vanishes at higher temperatures when the Co undergoes a phase transition into the paramagnetic state.

The following chapter will introduce a model that will intuitively explain the origin of the exchange bias effect.

2.3.1. Intuitive Picture

Before engaging more deeply with the different models for the exchange bias effect, in this section a simple and intuitive picture is given. This model is based on the microscopic exchange coupling between the ferromagnetic (FM) and antiferromagnetic (AFM) layers. Both the ferromagnet and the antiferromagnet are assumed to be single-domains with rigid spins. In the following, the significant stages of a shifted hysteresis loop will be addressed in order to explain the configuration of the magnetic moments using an exemplar hysteresis loop as illustrated in Figure 2.5. First of all, the process of field-cooling in order to induce an exchange bias in the ferromagnet will be explained.

For high temperatures, as when the temperature of the bilayer is kept above the Néel temperature T_N of the antiferromagnet but below the Curie temperature T_C of the ferromagnet, i.e., $T_N < T < T_C$, the magnetic moments of the ferromagnet align along an externally-applied magnetic field $\vec{H}$, while the moments of the antiferromagnet are randomly distributed (Figure 2.5a). A cooling of the bilayer below the Néel temperature T_N in the presence of a magnetic field leads to a ferromagnetic (parallel) alignment of the spins in the ferro- and antiferromagnet in the first monolayer at the interface. The spins in the following planes of the antiferromagnet align antiferromagnetically in order to prevail the zero net moment (Figure 2.5b). This induces a (unidirectional) pinning of the ferromagnetic layer. When the applied magnetic field $\vec{H}$ is reversed, the ferromagnetic spins start to rotate, while the antiferromagnet remains in its original state, exerting a microscopic force on the spins of the ferromagnet trying to keep the first monolayers of the spins at the interface ferromagnetically-aligned.

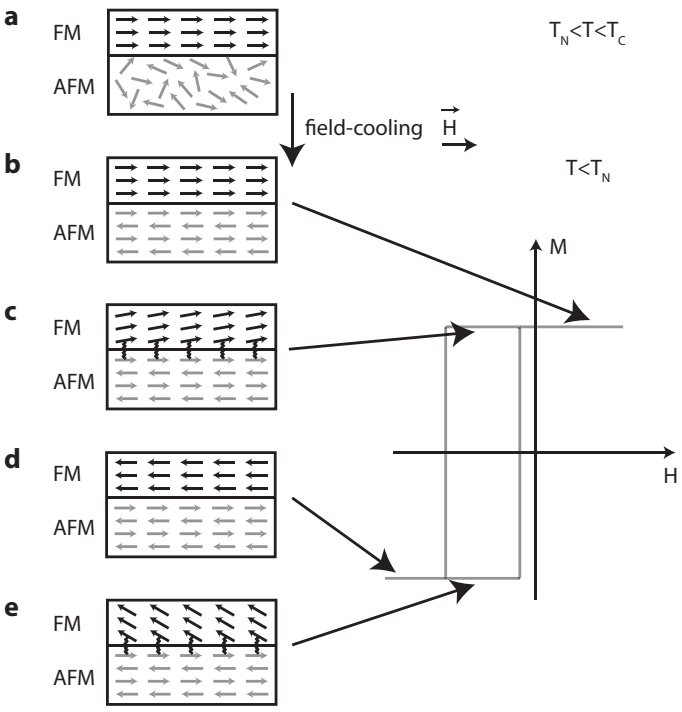

Figure 2.5 | Intuitive picture for the exchange bias effect. The spin arrangements in the ferromagnetic- and the antiferromagnetic-layer are illustrated at the significant stages of the hysteresis loop after field-cooling below the Néel temperature T_N in the presence of the magnetic field $\vec{H}$

In order to overcome this additional force, the magnetic field has to be larger than for an uncoupled ferromagnet (Figure 2.5c). With a further increase of the magnetic field the ferromagnet finally switches its magnetization direction (Figure 2.5d). If the field is rotated back to the initial value, the ferromagnetic spins switch back to their first orientation at lower fields because the antiferromagnetic spins now exert a torque in the same direction as the applied field (Figure 2.5e).

This simple model intuitively explains the shift of the hysteresis to negative field values (negative exchange bias) but disregards, for example, the enhanced coercivity in exchange biased bilayers and the magnetic and structural morphology. Hence, the following sections will discuss different improved models.

Blocking Temperature In the first part of this section is was stated that, as the temperature is increased to $T > T_N$, the exchange bias effect disappears[34]. In many cases, the exchange bias effect vanishes at even lower temperatures than T_N at the Blocking temperature T_B. Deviations from the Néel temperature are mainly caused by structural properties, such as grain sizes and the antiferromagnet's thickness[35]. Other reasons include the existence of multiple phases[36] and variations of the stoichiometry[37]. For single crystals and thick films it is $T_N \approx T_B$[38].

Training Effect Moreover, the magnitude of a loop shift can also depend on the number of switching processes of the ferromagnet. The irreversible effect of the reduction of the exchange bias field with the number of switching processes is denoted as the training effect. There are two types of training effects[34]:

- The first type leads to a decrease in the exchange bias field between the initial and the second loop. This can be related to an inherent frustration or to a symmetry of the antiferromagnetic anisotropy[39].

- Another type of training effect results in a decreased exchange bias field with every new loop, denoted by n. It was experimentally-found that the dependence of the exchange bias field in thin films is given by[40]:

$$H_{eb} \propto \frac{1}{\sqrt{n}} \text{ for } n > 2. \tag{2.9}$$

  This is the result of the reconfiguration of antiferromagnetic spins during field reversal.

As this section introduced the exchange bias effect along with its discovery and an intuitive picture of the origin of the loop shift, the following section will address a more theoretical approach.

2.3.2. The Meiklejohn Bean Approach

This section presents a mathematical model for the exchange bias effect that is based on the intuitive picture introduced in the previous section. This model is also proposed by Meiklejohn and Bean and focuses on the energy of the exchange bias system, as can be derived from the intuitive picture[17,41]. It is also known as the macroscopic model because it does not take the lateral structure of the magnetic layers into account.

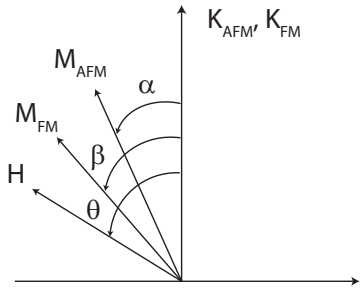

Figure 2.6 | Definition of the angles used in the Meiklejohn Bean Approach.

Similar to the intuitive picture, a ferromagnetic coupling, i.e. a parallel alignment of the spins at the ferromagnet/antiferromagnet interface is assumed. Moreover, the ferromagnet is treated as a single magnetic domain with a coherent rotation of its moments. For simplicity, the anisotropy axes of the ferro- and antiferromagnet are assumed to be parallel. Under these restrictions, the energy F of the exchanged bias system under an applied external field $\vec{H}$ can be expressed as

$$\begin{aligned} F = &-HM_{\mathrm{FM}} \cos(\theta - \beta) + K_{\mathrm{FM}} t_{\mathrm{FM}} \sin^2 \beta \\ &+K_{\mathrm{AFM}} t_{\mathrm{AFM}} \sin^2 \alpha - J_{\mathrm{INT}} \cos(\beta - \alpha), \end{aligned} \tag{2.10}$$

where H denotes the applied magnetic field, t_{AFM} and t_{FM} represent the thicknesses of the antiferromagnet and the ferromagnet, respectively, and K_{AFM} and K_{FM} denote the anisotropy constants of the antiferromagnet and ferromagnet, respectively. The angles are defined as illustrated in Figure 2.6. β is the angle between the magnetization with the anisotropy axis of the ferromagnet, while α is the angle between the antiferromagnetic sublattice (magnetization M_{AFM}) with its anisotropy axis and θ is the angle between the applied magnetic field and the anisotropy axis of the ferromagnet. The free energy F is a combination of the Zeeman energy (see Equation 2.3) and the (uniaxial) anisotropy contribution of the ferromagnet (the second term), while the third term describes the anisotropy of the antiferromagnet. The last term takes the interface coupling with the interface coupling constant J_{INT} into account.

Under the assumption that the anisotropy constant of the antiferromagnet is larger than the anisotropy constant of the ferromagnet $K_{\mathrm{AFM}} >> K_{\mathrm{FM}}$, which can be found in many cases, a minimization of the energy with respect to α and β, the exchange bias field, i.e., the shift of the hysteresis, H_{eb} is determined by:

$$H_{\mathrm{eb}} = -\frac{J_{\mathrm{INT}}}{M_{\mathrm{FM}} t_{\mathrm{FM}}}. \tag{2.11}$$

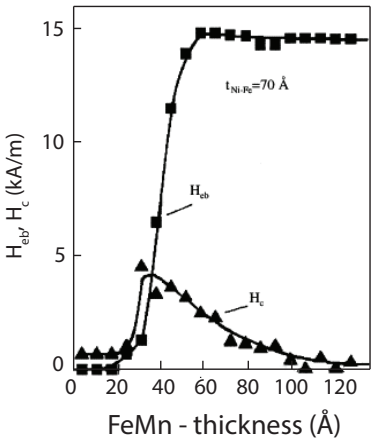

Figure 2.7 | Exchange bias field (squares) and coercive field (triangles) as a function of the film thickness of the antiferromagnet for $FeMn/Fe_{80}Ni_{20}$ bilayers.[1]

Accordingly, this model predicts a shift of the hysteresis to the opposite field cooling direction (a negative exchange bias). This is the case in many experimentally-investigated systems[17]. However, there are some materials that show a positive exchange bias, e.g. Fe/FeF_2 or Fe/MnF_2 bilayers[42,43].

Consequently, the following condition has to be fulfilled for the the observation of an exchange bias effect:

$$K_{\mathrm{AFM}} t_{\mathrm{AFM}} \geq J_{\mathrm{INT}}. \tag{2.12}$$

Thus, the film thickness of the antiferromagnet, as well as its anisotropy constant, are crucial parameters for the observation of exchange bias effect. The following paragraph will focus on the thickness dependence of the ferromagnet and the antiferromagnet.

Thickness Dependence According to Equation 2.11, the exchange bias field is proportional to the inverse of the thickness of the ferromagnet t_{FM}:

$$H_{\mathrm{eb}} \propto \frac{1}{t_{\mathrm{FM}}}. \tag{2.13}$$

This dependence is investigated and confirmed by various experiments, even for large film thicknesses of several hundred nanometers. For very small film

[1] Reprinted from Exchange bias, 192, J. Nogués and Ivan K. Schuller, pp. 203. Copyright (1999), with permission from Elsevier.

thicknesses this relation does not hold, as the ferromagnet may become inhomogeneous[17].

The influence of the thickness of the antiferromagnet t_{AFM} on the exchange bias is more complicated. Figure 2.7 shows the dependence of H_{eb} and H_c as a function of t_{AFM} for the FeMn/$Fe_{80}Ni_{20}$ bilayers. For small film thicknesses no hysteresis shift H_{eb} can be observed, as Condition 2.12 is not fulfilled. Moreover, the influence of the film thickness on K_{AFM} can also play an important role. Furthermore, the interplay between the Blocking temperature T_B and small thicknesses of the antiferromagnet, as well as the relation between the domain structure and the domain wall size of the antiferromagnet, can influence H_{eb}. As shown in Figure 2.7, the loop shift H_{eb} is zero for small thicknesses of the antiferromagnet below the material-dependent critical film thickness. A further increase of the thickness of the antiferromagnet leads to a strong increase of the exchange bias field H_{eb} until it reaches its maximum. For larger thicknesses it slightly decreases and becomes independent of the thickness.

In general, the loop shift H_{eb} as a function of thickness t_{AFM} is given by[44]:

$$H_{eb} = a + \frac{b}{t_{AFM}} + \frac{c}{t_{AFM}^2}. \tag{2.14}$$

The coercivity H_c dependence of the film thickness is also shown in Figure 2.7. H_c increases with increasing film thickness until the critical film thickness is reached and a loop shift can be observed. A further increase of the film thickness leads to a decrease in the coercive field. For larger film thicknesses, the coercivity - again - approaches small values.

Overall, the Meiklejohn Bean Approach offers a good understanding of the exchange bias effect but overestimates the loop shift in most cases, as the observed values are much smaller than expected[17,45]. Moreover, it does not take structural conditions, such as domains in the (anti-)ferromagnet or surface roughnesses, into account.

In the following section, a different approach for the description of the spin structure, which can generate an exchange bias, will be presented.

2.3.3. The Partial Domain Wall Approach

Néel[46,47] presented an important improvement to the Meiklejohn and Bean approach by considering the formation of domains in either the ferromagnet or the antiferromagnet parallel to the interface instead of having a rigid spin arrangement. Further improvements were performed by Mauri *et al.*[48], Kiwi *et al.*[49–51], Geshev[52] and Kim *et al.*[53,54]. They proposed that the formation of

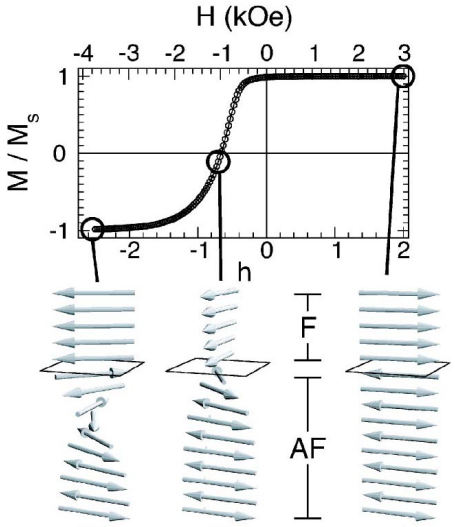

Figure 2.8 | Magnetization curve for the antiferromagnet/ferromagnet bilayer with a calculated spin structure during magnetization reversal.[1]

a partial domain wall results in an additional energy cost during magnetization reversal and thus, induces a shift of the hysteresis. This model results in more accurate exchange bias parameters. Figure 2.8 illustrates the presence of a domain wall in the antiferromagnetic layer along with corresponding spin structures at significant stages of the magnetization curve. Depending on whether the domain wall is formed in the ferromagnet or in the antiferromagnet, the loop shift in this model is given as:

$$H_{\mathrm{eb}} \propto \sqrt{K_{\mathrm{AFM}} A_{\mathrm{AFM}}}/M_{\mathrm{FM}} t_{\mathrm{FM}} \text{ or} \tag{2.15}$$

$$H_{\mathrm{eb}} \propto \sqrt{K_{\mathrm{FM}} A_{\mathrm{FM}}}/M_{\mathrm{FM}} t_{\mathrm{FM}}, \tag{2.16}$$

with the exchange stiffness A_{FM} and A_{AFM} for the ferromagnet and the antiferromagnet, respectively. This approach can only be applied for exchange bias systems with film thicknesses that are large enough to form such a domain wall.

It leads to a more accurate determination of the loop shift than the Meiklejohn Bean Model, but does not take the coercivity enhancement into account. Moreover, this model can be used to describe compensated, partially compensated, and uncompensated spins at the interfaces. However, it is based on perfect

[1] Reprinted figure with permission from Joo-Von Kim, R. L. Stamps, B. V. McGrath, and R. E. Camley, Physical Review B, 61, pp. 8888, 2000. Copyright 2000 by the American Physical Society.

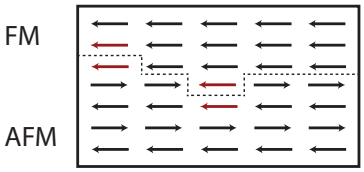

Figure 2.9 | The interface between the antiferromagnet and ferromagnet with surface roughness and antiferromagnetic domains in the Malozemoff Model. The frustrated interactions are marked.

surfaces and disregards the presence of structural defects and surface roughnesses. Therefore, the following section will present a model for the description of exchange bias effects, which is based on the presence of uncompensated spins due to surface roughnesses.

2.3.4. Malozemoff's Random Interface Model

Malozemoff[55–57] introduced a model in which the interface between the antiferromagnet and the ferromagnet does not need to be perfectly smooth. The roughness, as well as imperfections at the interface, generate a random field that induces the formation of domain walls perpendicular to the surface. This leads to domains in the antiferromagnet with sizes of approximately $\pi\sqrt{A_{\mathrm{AFM}}/K_{\mathrm{AFM}}}$. Statistically, the domains generate uncompensated spins at the interface, which couple to the ferromagnetic moments and induce a unidirectional anisotropy in the ferromagnetic layer. This behavior is illustrated in Figure 2.9 on the basis of an atomically-stepped surface. Therefore, an imbalance between positive and negative coupled spins is caused and, hence, an exchange bias. The frustrated interactions in Figure 2.9 are marked in a different color.

The calculated loop shifts, based on this model, are in the right order of magnitude with the experimental results. The loop shift is given by[57]:

$$H_{\mathrm{eb}} = 2\sqrt{K_{\mathrm{AFM}}A_{\mathrm{AFM}}}/M_{\mathrm{FM}}t_{\mathrm{FM}}. \tag{2.17}$$

The Random Interface Model is a reasonable improvement of the aforementioned descriptions of the exchange bias effect, as it takes the inevitable structural defects in surfaces into account.

2.3.5. The Spin-Flop Model

Koon[58] performed detailed calculations for a flat and completely compensated interface between the antiferromagnetic and ferromagnetic layers with focus

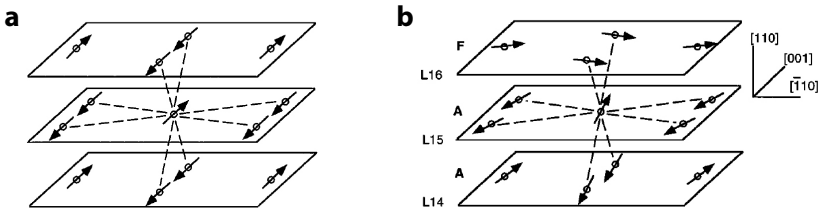

Figure 2.10 | a The spin structure researched in the Koon model and **b** the energetically-favored spin arrangement. The exchange bonds are visualized through the dashed lines.[1]

a on the angular-dependence of the magnetization of the ferromagnet on the interfacial energy. Koon assumed that the interaction in the bct structure is between the opposing sublattices and that the ferromagnetic and antiferromagnetic spins are orientated perpendicularly to each other. Figure 2.10a illustrates the magnetic investigated structure. The according energetically-favored spin structure is illustrated in Figure 2.10b. The spins in the interfacial plane L15 are canted by small angles but still fully compensated. The compensated spins in plane L16 are canted by 90°, indicating a perpendicular coupling between the spins between the antiferromagnet and the ferromagnet. Koon denotes this as spin-flop coupling at the interface between ferromagnet and antiferromagnet. Afterwards, Schultness and Butler[59] demonstrated that the spin-flop model does not result in a loop shift (for a perfectly flat surface) but generates a coercivity enhancement.

Hence, a combination of the spin-flop coupling model and the assumption of surface roughnesses and defects, as introduced in Malozemoff's Random Interface Model, allows for a complemented description of the exchange bias effect, as both the unidirectional anisotropy and the coercivity enhancement are addressed[59].

The exchange bias effect is widely used in applications, especially in information storage devices in reference layers. The application of the exchange bias effect in commercial devices started around 1956 with the presentation of the IBM 305 RAMAC computer, as it incorporated the IBM 350 - the world's first hard disk with a capacity of 5 MB. Magnetoresistive effects are used for the read-out of the magnetic pattern written on the platter. The magnetization direction of the free magnetic layer in the read head switches in the presence of the stray field caused by different magnetization directions of the magnetic

[1] Reprinted figures with permission from N. C. Koon, Physical Review Letters, 78, pp. 4865, 1997. Copyright 1997 by the American Physical Society.

patterns, while the readback (an exchange biased ferromagnetic layer) remains in a constant magnetic alignment. The resulting resistivity change in the magnetoresistive read head represents the magnetic pattern of the hard disk. As the magnetoresistance effects are essential for spintronics, the following section will introduce these effects.

2.4. Magnetoresistance

The field of spintronics uses the spin of the electrons as additional degree of freedom in order to improve the existing electronics with enhanced capabilities and a lower power consumption. This field attracted a lot of interest with the discovery of the giant magnetoresistance (GMR) effect and the research of structures combining the charge and the spin of electrons increased.

Magnetoresistance (MR) refers to the interaction between the electric conductivity and an applied magnetic field. The anisotropic magnetoresistance (AMR) effect has been known for a long time. It can be found in ferromagnetic metals where the electrical conductance depends on the angle between the current and the magnetization direction. Thus, it was also used as a read-out head for the magnetic information stored in the first magnetic devices. Later, these AMR-based sensors were replaced by read heads consisting of a GMR sensor and afterwards a TMR sensor in order to obtain higher signal amplitudes. A GMR element is a spin "switch" as a spin-dependent resistance can be switched on and off with the help of an external magnetic field.

This section focuses on the anisotropic magnetoresistance (AMR) effect and the giant magnetoresistance (GMR) effect. Among others, measurements of the AMR effect are used in this work to determine the amplitude of the exchange bias. GMR structures were grown in order to demonstrate the ability of the films for the use in spintronic devices, which is why the topic is only touched upon briefly. A more detailed description of the AMR and GMR can be found, for example, in references[23,60,61] and[62], respectively.

2.4.1. The Anisotropic Magnetoresistance Effect

The AMR effect[63–65] describes the dependence of the electric conductance on the magnetization $\vec{M}$ of a sample. It was first discovered in 1857 by Thomson (also known as Lord Kelvin)[63] in $3d$ transition metals. The AMR effect causes a resistivity change as a function of the angle between the electrical current $\vec{j}$ and the magnetization $\vec{M}$. The important contribution to the electrical conductivity in metals such as Fe, Co, and Ni is given by the d-electrons as

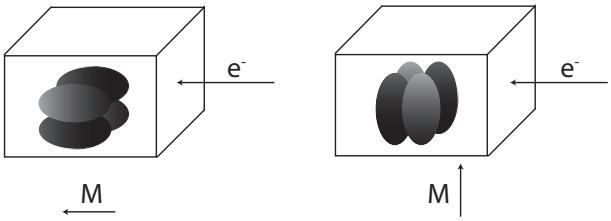

Figure 2.11 | The alignment of the orbitals for parallel and antiparallel alignment between the current and the magnetic field.

they link the magnetization of a ferromagnet to its conductivity because of the ability of temporary occupation of empty *d*-states by 4*s*-electrons. Hence, the scattering of conducting electrons becomes spin- and orbital-dependent[66,67]. The electric transport in a metal is mainly conducted by (nearly free) 4*s*-electrons and less by 3*d*-electrons, which are only moderately localized. Nevertheless, the *d*-electrons can contribute the electrical conductivity, while the *f*-electrons are highly localized and do not contribute to the electrical conductivity. As in a ferromagnet the density of 3*d*-electrons is different for spin-up and spin-down electrons, the conductivity depends on the magnetic properties. An externally-applied magnetic field aligns the ferromagnetic spins, and, hence, the orbitals, and changes the scattering probabilities of the electrons. For a parallel alignment $\vec{j} \parallel \vec{M}$ of the magnetization $\vec{M}$ and an electrical current $\vec{j}$ the conductivity is lowered due to a higher collision probability of electrons. Instead, for a perpendicular alignment $\vec{j} \perp \vec{M}$ the scattering probability is minimal and, accordingly, the electrical conductivity is high, as illustrated in Figure 2.11. As a result, the scattering probability is a function of the angle α between current $\vec{j}$ and magnetization $\vec{M}$. According to the two-current model and with the Boltzmann transport equations, the resistivity is given as[64,65]:

$$R = R_0 + \Delta R \cos^2(\alpha), \tag{2.18}$$

with the initial resistivity R_0 and the resistivity change ΔR. As the amplitude of the AMR effect is usually of a few percent, the use of AMR based sensors is limited. An improved effect amplitude is given by the GMR effect, which will be introduced in the following section.

2.4.2. Giant Magnetoresistance Effect

The use of the AMR effect in modern read heads is challenging as the effect amplitude is not sufficiently high enough to read small bit sizes in hard disks.

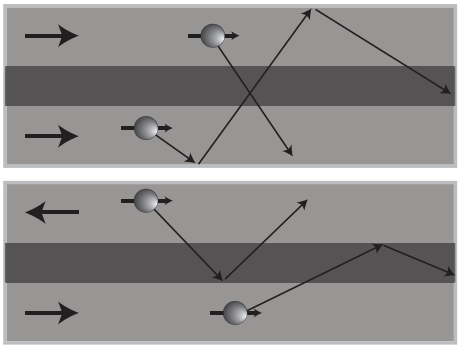

Figure 2.12 | Illustration of the scattering processes for parallel and antiparallel alignment of the electrodes in a GMR multilayer.

Hence, read heads using the GMR or TMR effect, which exhibit higher signal amplitudes, replaced the sensors based on the AMR effect. The first commercial GMR read sensor was introduced in 1997. About ten years earlier, the GMR effect was discovered by Grünberg[2] and Fert[3] who were awarded the Nobel Prize in 2007 for their work in the field. A GMR device basically consists of two ferromagnetic metals separated by a thin non-ferromagnetic metal with a thickness smaller than the spin diffusion length, i.e., the distance an electron can travel without changing its spin. Spin-polarized electrons are then injected from one ferromagnetic layer into the other ferromagnetic layer while maintaining their spin. The electrical resistivity of this multilayer stack depends on the magnetization alignment of both electrodes. This is a result of spin-dependent scattering of the conduction electrons in the layers. For an antiparallel magnetic alignment, a mismatch in the density of states leads to a larger resistivity as the electrons have a smaller mean free path than in parallel alignment. Figure 2.12 illustrates the magnetization-dependent scattering of the conduction electrons. In order to obtain an antiparallel alignment of the electrodes one can either use a film thickness of the spacer material that leads to an antiferromagnetic alignment due to the RKKY interaction or an exchange biased electrode in combination with a soft magnetic electrode.

With a further increasing storage density and thus smaller magnetic patterns, the GMR effect in sensors was replaced by read heads based on the TMR effect, as this results in large effect amplitudes even for small sizes along with a low power consumption and a high thermal stability. With the introduction of devices such as STT-MRAMs the magnetization dynamics of the magnetic electrodes become an important factor for the fabrication of devices. This topic is addressed in the following chapter.

2.5. Magnetization Dynamics in Ferromagnets

While the last sections described the static properties of ferromagnets, this section will focus on the dynamics of the magnetization[30,68,69], as this becomes important for spintronic devices, i.e., for STT-MRAMs, leading to low switching current densities.

This section semi-classically introduces the motion of spins. The ferromagnet is described in the macrospin approximation as one total classical vector $\vec{M}$ and thus, the ferromagnet is considered to be single-domain with no spatial inhomogeneities of the internal field.

The magnetization $\vec{M}$ and the total angular momentum $\vec{J}$ are related by:

$$\vec{M} = -|\gamma|\vec{J}, \tag{2.19}$$

with the gyromagnetic ratio $\gamma = \frac{g q_e}{2 m_e} = \frac{g \mu_B}{\hbar}$, where g denotes the gyromagnetic factor and q_e and m_e are the the charge and the mass of the electron, respectively. μ_B is the Bohr's magneton and $\hbar$ is the Planck constant.

The time derivative of the angular momentum $\vec{J}$ is proportional to the torque generated by the effective magnetic field H_{eff} inside the sample (as explained in the previous sections, the field inside the sample can differ from the externally-applied field) acting on the magnetization $\vec{M}$:

$$\frac{\mathrm{d}\vec{J}}{\mathrm{d}t} = \vec{M} \times \vec{H}_{eff}, \tag{2.20}$$

and, consequently, the time derivative of the magnetization $\vec{M}$ is given by:

$$\frac{\mathrm{d}\vec{M}}{\mathrm{d}t} = -|\gamma|(\vec{M} \times \vec{H}_{eff}). \tag{2.21}$$

This equation describes a precessional motion of the magnetization $\vec{M}$ around the effective magnetic field $\vec{H}_{eff}$ with a constant amplitude, as illustrated in Figure 2.13a.

By adding a second torque on the magnetization vector that contains a damping term ($\lambda > 0$) that tends to aligns the magnetization vector with the effective field H_{eff}, the well-known Landau-Lifshitz equation[70] is obtained:

$$\frac{\mathrm{d}\vec{M}}{\mathrm{d}t} = -|\gamma|(\vec{M} \times \vec{H}_{eff}) - \frac{\lambda|\gamma|}{M_S}(\vec{M} \times (\vec{M} \times \vec{H}_{eff})). \tag{2.22}$$

The resulting motion of the magnetization $\vec{M}$ (with the saturation magnetization M_s) is a precession around an effective field $\vec{H}_{eff}$, as illustrated in Figure 2.13b.

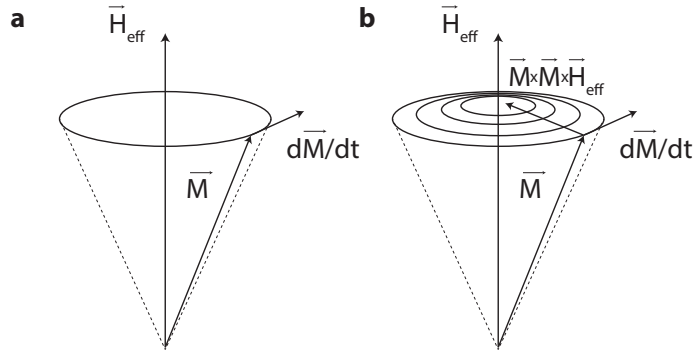

Figure 2.13 | The dynamics of the magnetization vector $\vec{M}$ in the presence of an effective field $\vec{H}_{\text{eff}}$ **a** without damping and **b** with a damping term.

For $\lambda \gg 1$ Equation 2.22 leads to unreasonable results, as $\frac{\mathrm{d}M}{\mathrm{d}t} \to 0$ and the system approaches equilibrium infinitely slowly[71]. In 1954 Gilbert modified the damping term using the Lagrange formalism with classical Rayleigh damping. The result is known as the Landau-Lifshitz-Gilbert equation[72] and can be written as:

$$\frac{\mathrm{d}\vec{M}}{\mathrm{d}t} = -|\gamma|\vec{M} \times \vec{H}_{\text{eff}} + \frac{\alpha}{M_{\text{s}}}\left(\vec{M} \times \frac{\mathrm{d}\vec{M}}{\mathrm{d}t}\right), \tag{2.23}$$

where the quantity parameter α is the Gilbert damping parameter. In this work the ferromagnetic resonance technique is used in order to determine the damping parameters of Co-Fe-Si-based Heusler compounds.

As this chapter described until now different kinds of ferromagnetic phenomena, the following section will introduce a different kind of physical effects - ferroelectricity. In any case, both the origin and the ferroelectric properties exhibit a lot of analogies to the ferromagnetism.

2.6. Ferroelectrics

The second part of this work includes magnetic studies containing $BiFeO_3$ and $LaFeO_3$ films. Both materials are reported to be ferroelectric[20,21]. Thus, this section provides an overview of different aspects of ferroelectricity[73–75]. Some observations can be directly transferred from ferromagnetism, e.g., the hysteretic behavior as well as the dependence of the ferroelectric susceptibility.

In 1920 Valasek[76,77] discovered the ability to reverse the electrical polarization of sodium potassium tartrate tetrahydrate ($NaKC_4H_4O_6 \cdot 4H_2O$), also

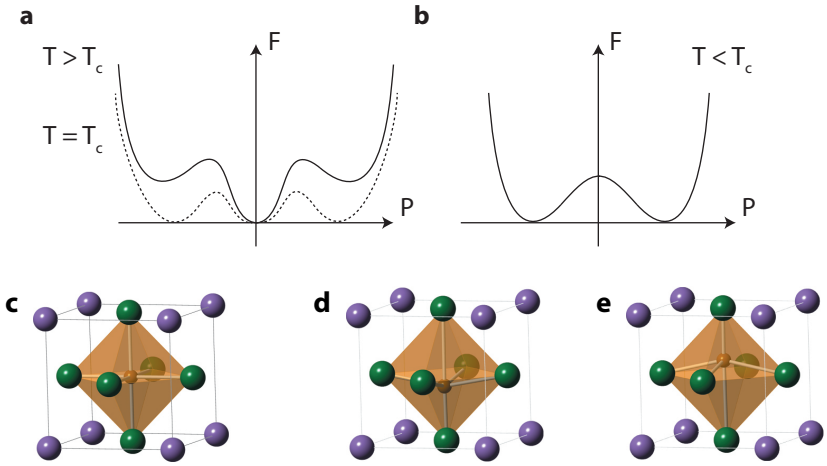

Figure 2.14 | a, b Gibbs free energy *F* versus polarization *P* for temperatures around the Curie temperature along with illustrations of the displacement in the unit cell. **c** Illustration of the unit cell in the centrosymmetric phase, i.e. for $T \geq T_c$. For $T < T_c$ the unit cell shows a broken inversion symmetry and can be polarized in two different directions **d** and **e**.

known as Rochelle salt, by the application of an electric field. Moreover, he found a hysteretic behavior of the polarization depending on an externally-applied electric field as well as a transition temperature at which the polarization vanishes. (In fact, Rochelle salt has two transition temperatures and ferroelectricity is only observed for temperatures between -18°C and 24°C[73].) This phenomena was first called "Seignette-electricity" because Seignette was the first who prepared this salt, around 1655, in La Rochelle, France. Later, around 1935, with the discovery of ferroelectric properties in ammonium salts[78,79] and potassium di-hydrogen phosphate[80,81] this effect was renamed to "ferroelectricity". In analogy to ferromagnetism, the phase transition between the ferroelectric and the paraelectric phase is denoted as ferroelectric Curie temperature.

The phase transition from the paraelectric to the ferroelectric phase can be phenomenologically explained using the Landau-Ginzburg-Devonshire thermodynamic theory[82–87]. In general, ferroelectric materials possess two or more equilibrium orientations for the direction of the spontaneous electrical polarization in the absence of an external electric field. In perovskites, such as $BiFeO_3$ and $LaFeO_3$, the polarization is caused by a relative displacement of positive and negative charge centers. Moreover, ferroelectric materials also exhibit piezoelectric and pyroelectric properties. Both distorted states, i.e., the

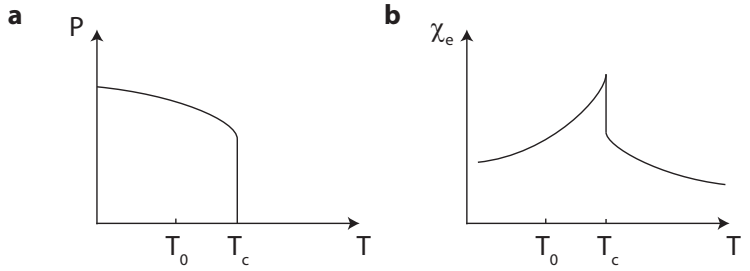

Figure 2.15 | Illustration of a first-order phase transition: **a** Polarization P and **b** susceptibility χ_e as a function of temperature T. With transition temperature T_0 and ferroelectric Curie temperature T_c.

two possible polarization directions, have a lower energy than the state with no displacement (at $T = 0\,K$). The phase in which the material exhibits no spontaneous polarization is called paraelectric state and is usually related to the centrosymmetric structure. Thus, for the presence of ferroelectricity it is necessary to have a broken inversion symmetry of the crystallographic ordering, which transforms into a centrosymmetric one for temperatures above the ferroelectric Curie temperature T_c.

Figure 2.14 illustrates the Gibbs free energy F for different temperatures around the Curie temperature T_c along with the crystallographic distortion of a perovskite unit cell. If the phase transition is of a first-order, the Gibbs free energy F exhibits three minima at the Curie temperature, as illustrated by the dashed line in Figure 2.14a. The material can either be in the paraelectric, i.e., centrosymmetric, state or it exhibits a spontaneous polarization. Such metastable phases can lead to a hysteretic behavior in experiments. At temperatures higher than the Curie temperature, the centrosymmetric phase is energetically more favorable, as depicted by the solid line Figures 2.14a and 2.14c. For temperatures $T < T_c$ the double-well structure becomes more pronounced and results in two possible spontaneous polarization directions as a result of two possible atomic displacements of the Fe ion. The according potential is illustrated in Figure 2.14b along with crystals showing a displacement of the Fe ion, which is shifted to the bottom in 2.14c and to the top in 2.14d.

At the ferroelectric Curie temperature the spontaneous polarization vanishes with a discontinuity, which changes abruptly in the case of a first-order phase transition, as shown in Figure 2.15a. The polarization $\vec{P}$ induced by the applied electric field $\vec{E}$ in the dielectric material is given by:

$$\vec{P} = \chi_e \varepsilon_0 \vec{E} \tag{2.24}$$

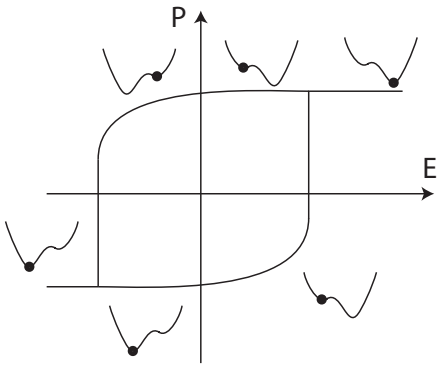

Figure 2.16 | Idealized ferroelectric hysteresis with the free energy potential exhibiting the two possible polarization directions.

with the electric susceptibility χ_e, illustrated in Figure 2.15b, and the dielectric permittivity of vacuum ε_0. For temperatures above the transition point the dielectric susceptibility for a small electric field follows the Curie-Weiss Law:

$$\chi_e = \frac{C}{T - T_0}, \tag{2.25}$$

where C is a positive constant and T_0 the transition temperature. For a second-order transition it is $T_0 = T_c$, while it is $T_0 \neq T_c$ for a first-order phase transition. In a ferroelectric material the spontaneous polarization will generate a charged surface that is antiparallel to its spontaneous polarization and increases the system's free energy. Moreover, the material will form ferroelectric grains to minimize the field generated by the charged surfaces. These grains point to different directions compensating each other. Thus, the resulting net spontaneous polarization and the depolarizing field becomes zero.

Figure 2.16 shows an illustration of the polarization P as a function of the applied electric field E along with the Gibbs free energy potential and shows the switching process from one polarization state to the other. The hysteresis is caused by irreversible switching processes of the polarization due to the presence of lattice defects interacting with domain walls or the propagation or nucleation of new ferroelectric domains. For the switching process the energy barrier between both stable polarization states has to be overcome. The applied electrical field results in a tilting of the potential and can be used for an intuitive explanation of the hysteresis loop. Moreover, denoted are the remanent polarization P_0 as well as the coercive field E_0, at which the polarization changes sign.

This topic completes the chapter introducing the fundamentals that are needed to understand the thesis' investigation techniques, as well as the properties of the analyzed materials. The following chapter will focus on the investigated materials.

3 Materials

In the last chapter the physical basics for a profound understanding of the materials and effects used in this thesis were introduced. This chapter applies these basics in order to provide a deeper insight into the crystallographic and magnetic properties of the investigated materials. Conclusively, it unveils why these materials are promising for the improvement of spintronic devices.

This chapter is organized as follows. Firstly, the fundamentals of Heusler compounds are introduced. Here, the focus lies on the structure and electronic properties of $Fe_{1+x}Co_{2-x}Si$ with $0 \leq x \leq 1$. Secondly, the basics of the class of perovskites are presented. These basics allow for a discussion of the properties of the perovskite $BiFeO_3$ and its suitability as an antiferromagnet for spintronics. The last section introduces the class of orthoferrites, i.e., perovskites that contain a rare earth element. Particularly, it deals with the crystallographic and magnetic properties of $LaFeO_3$.

3.1. Co- and Fe-Based Heusler Compounds

Heusler compounds are a well known and versatile class of materials that is valued as a promising material for future spintronics. Hence, it has been a subject of intense research over the last years. In this section the basics on the crystallographic structure with a focus on Co_2FeSi and Fe_2CoSi are briefly introduced, based on Reference[13]. Furthermore, the electronic properties are discussed in more detail, using Density Functional Theory (DFT).

In the year 1903 Friedrich Heusler discovered that the compound Cu_2MnAl is ferromagnetic, although its elements Cu, Mn, and Al are all non-ferromagnetic[88,89]. To find the origin of Heusler's observation, the structure and the atomic ordering were investigated by Bradley and Rodgers in 1934[90].

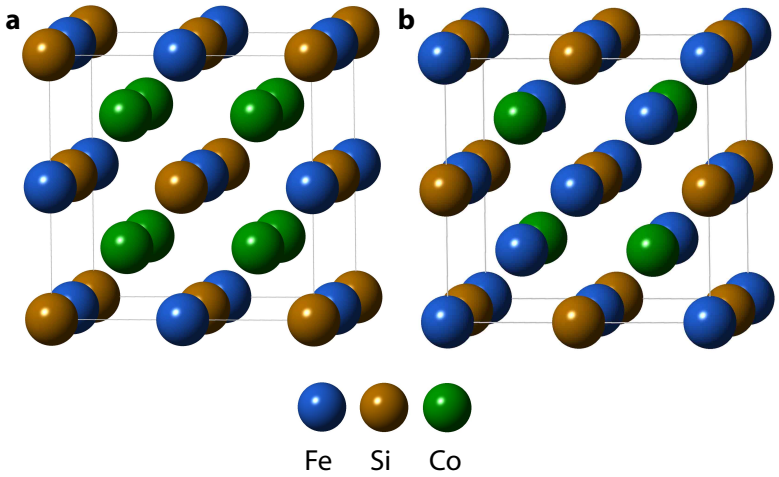

Figure 3.1 | Illustration of the unit cells **a** of Co_2FeSi in $L2_1$ structure and **b** of Fe_2CoSi and X_a structure.

Their findings reveal that a (full) ternary Heusler compound has the formula X_2YZ, with X and Y being transition metals and Z a main group element. The crystallographic structure can be described as an fcc lattice with a four-atom basis[91]. Each origin is shifted by $1/\vec{4}$. Here, the four sublattices are denoted by A, B, C, and D. There are two possible orderings: Co_2FeSi, for example, crystallizes in the $L2_1$ structure with the occupation sequence of Co - Fe - Co - Si with symmetry $Fm\bar{3}m$ and space group no. 225. Figure 3.1a is a sketch of the unit cell (in order to visualize the inversion symmetry, the origin is shifted by $1/\vec{4}$). The lattice parameter of Co_2FeSi is 5.64 Å[92].

Fe_2CoSi crystallizes with a different occupation of the sublattices, which is Co - Fe - Fe - Si. Fe_2CoSi is a so-called inverse Heusler compound forming the X_a structure (Figure 3.1b). The symmetry is lowered to $F\bar{4}3m$ with spacegroup no. 216 as no inversion symmetry is present. Fe_2CoSi has a lattice parameter of 5.645 Å[93]. A compound crystallizes in the inverse structure when the Y atom, e.g. Co, has more valence electrons than element X, e.g. Fe[94].

This thesis presents investigations of a stoichiometric series ranging from Co_2FeSi to Fe_2CoSi. Since both compounds crystallize in different crystallographic structures, i.e. in the $L2_1$ and the X_a structures, this permits investigating the influence of the structure and composition on the magnetic properties. To gain a first impression of this interplay, in the next section the electronic properties of Co_2FeSi and Fe_2CoSi are described in detail, as they are crucial for

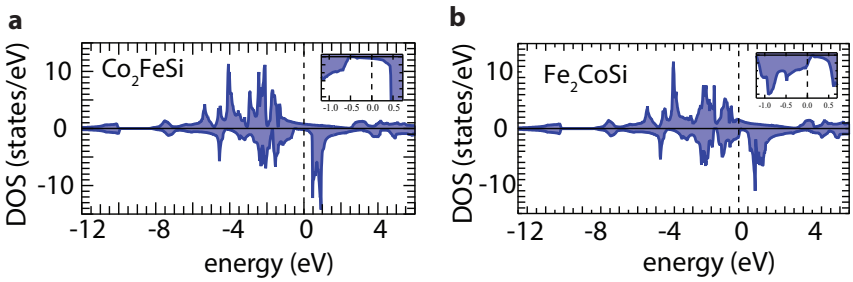

Figure 3.2 | Density of states **a** for Co_2FeSi[95] and **b** for Fe_2CoSi, calculated using *GW* approximation. Figure courtesy of M. Meinert.

understanding the behavior of these materials in, e.g. MTJs, and often form a basis for future investigations and the improvement of materials.

3.1.1. Electronic Properties of Co_2FeSi and Fe_2CoSi

For electrodes in spintronic devices it is desirable that only electrons of one type of spin are present at the Fermi energy, i.e., the material is half-metallic. This leads to high effect amplitudes, such as TMR ratios. In fact, many Heusler compounds are reported to be half-metallic[96]. This can be relatively-easily deduced from the spin-resolved density of states. Here, the *GW* many-body perturbation theory is used in order to calculate the DOS for Co_2FeSi and Fe_2CoSi (Figure 3.2a and b). The calculational details are given in Reference[95]. At first glance, both DOS look very similar. Co_2FeSi and Fe_2CoSi possess a (pseudo-)gap in the minority channel. However, while the Fermi energy for Co_2FeSi is located inside the pseudo-gap, it is shifted to lower energies and cuts some occupied bands in the case of Fe_2CoSi. Due to the gap in the minority states, a high TMR effect can be expected assuming perfect ordering of the films. Nevertheless, it has kept in mind that in real samples a variety of effects, e.g, lattice mismatches, impurities, and defects, can drastically influence the TMR ratio. Hence, the agreement with experimental results is discussed in the Results chapter.

Furthermore, the Gilbert damping is expected to be low in half-metals. Thus, in this work the magnetization dynamics of these films are also investigated. A low damping is important if the magnetization direction is switched using spin-torque, for example in STT-MRAMs.

3.2. Perovskites

The second material class investigated in this work are perovskites: thin $BiFeO_3$ and $LaFeO_3$ films. This section presents an overview of the most important properties of perovskites[97,98].

In 1829, Gustav Rose discovered the mineral $CaTiO_3$ and named it perovskite in honor of the mineralogist Count Lev von Perovski. This name became a generic term for structures with the general formula ABC_3, where A is a cation that can be monovalent, divalent, or trivalent and B a transition metal cation that is surrounded by an octahedron of C anions. The C atom is often an oxygen, nitrogen, or flour atom. If A is a rare earth element, like in $LaFeO_3$, the compound is denoted as orthoferrite.

The ideal (undistorted) cubic crystal structure of perovskites has $Pm\bar{3}m$ symmetry with space group 221. A sketch of the unit cell with complete ordering is presented in Figure 3.3 on the basis of a $BiFeO_3$ unit cell. This is also known as the aristotype structure.

The type of ions forming the perovskite structure play a crucial role for the lattice parameters of the unit cell, as they can cause deviations from the ideal

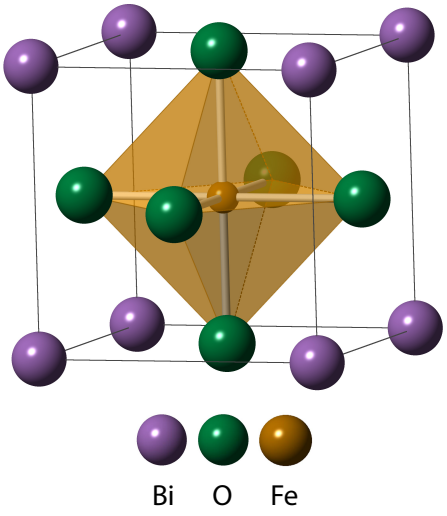

Figure 3.3 | Illustration of a $BiFeO_3$ unit cell in the perfectly undistorted γ-phase with $Pm\bar{3}m$ symmetry (the aristotype structure)

Table 3.1 | Overview of the Goldschmidt tolerance factor *t* and the resulting crystal structure[100].

t	Crystallographic Structure
t<0.75	ilemnite structure
0.75 <t<0.9	distorted perovskite incl. orthorhombic distortion
0.9 <t<1	cubic (ideal size of A and B ions)
1<t<1.13	hexagonal

structure to a crystal with lowered symmetry. The degree of deformation can be estimated using the Goldschmidt tolerance factor[98,99]:

$$t = \frac{r_A + r_C}{\sqrt{2}(r_B + r_C)} \tag{3.1}$$

with the ionic radii $r_{A,B,C}$ of cation A and B and the C anion. A perfect cubic perovskite has $t = 1$, as for example $SrTiO_3$. If the radius of cation A decreases it is $t < 1$ and the oxygen octahedron that surrounds cation B tilts in order to fill the voids causing the cubic lattice to deform. Hence, the Goldschmidt tolerance factor determines the crystallographic structure of the compound. Table 3.1 gives an overview of the resulting structure depending on the Goldschmidt tolerance factor t. The induced distortion can lead to a ferroelectric behavior in the perovskite. This is due to two different effects. For $t < 1$, the ferroelectricity arises from off-centered A anions. This is also known as A-site driven ferroelectric material. However, in the case of $t > 1$, the B ion is too small for the ideal structure and the ferroelectricity is caused by off-centering of the B anion.

The following section will focus in detail on the crystallographic and magnetic structure of $BiFeO_3$, as it is a main topic of this thesis.

3.2.1. $BiFeO_3$

The structure and the origin of ferroelectricity of $BiFeO_3$ crystals is well known and has been investigated in many studies[102–104]. The crystallographic unit cell of a $BiFeO_3$ crystal is trigonal (a small distortion from the cubic perovskite structure leads to a trigonal symmetry) with a Goldschmidt tolerance factor of $t = 0.913$[105]. Thus, the distortion is relatively small. In general, trigonal crystal structures, such as $BiFeO_3$, can be depicted by any of the following unit cells: pseudocubic (pc), rhomohedral (rh), or hexagonal (hex) (Figure

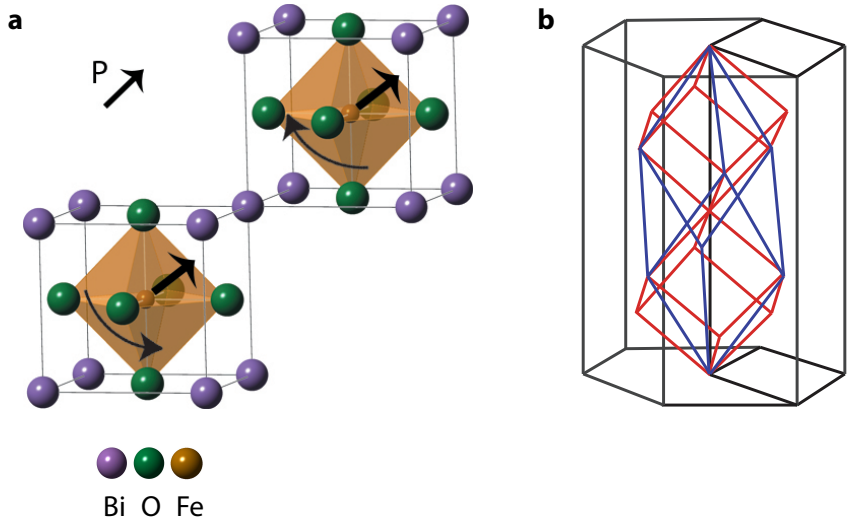

Figure 3.4 | a Two $BiFeO_3$ unit cells in the ferroelectric/α-phase illustrating the broken inversion symmetry caused by the shift of the Fe atom and the rotation of the oxygen octahedra. **b** The relation between the pseudocubic (red), rhombohedral (blue), and hexagonal (black) representation of a trigonal unit cell.

Table 3.2 | Lattice constants/angles of the $BiFeO_3$ unit cell in pseudocubic (pc), rhombohedral (rh), and hexagonal (hex) representation, respectively[101].

a_{pc} = 3.965 Å	α_{pc} = 89.35°
a_{rh} = 5.634 Å	α_{rh} = 59.35°
a_{hex} = 5.579 Å	c_{hex} = 13.869Å

3.4b). The lattice parameters for a $BiFeO_3$ crystal in all three different representations are summarized in Table 3.2. The relations between all systems are: $[001]_{hex}=2[111]_{pc}=[111]_{rh}$ and $[110]_{hex}=[1\bar{1}0]_{pc}=[\bar{1}10]_{rh}$.

The room temperature phase of $BiFeO_3$ is the ferroelectric α-phase. The unit cell is rhomhohedrally-distorted with $R3c$ symmetry and spacegroup no. 161[101,106]. Figure 3.4a shows two unit cells of $BiFeO_3$ in the α-phase in the pseudocubic representation. The Bi^{3+} cations occupy the corner positions of the almost-cubic unit cell while the Fe^{3+} cation is placed in the middle of the cell surrounded by an O_6 oxygen octahedron. The 12-coordinated voids between the octahedra are filled with Bi ions. The broken inversion symmetry in the

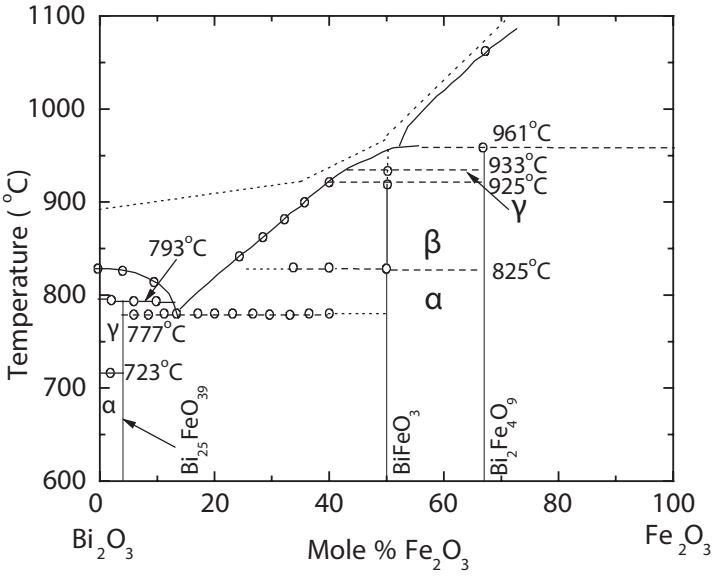

Figure 3.5 | Phase diagram of the Bi-Fe-O compounds from Bi_2O_3 to Fe_2O_3.[1]

ferroelectric phase is caused by a tilt of the FeO_6 octahedron along the [111] direction and a shift of the Bi and Fe atoms along the [111] direction. Moreover, $BiFeO_3$ is a transparent insulator.

A $BiFeO_3$ crystal can undergo transitions between several different phases. Figure 3.5 shows a phase diagram of the Bi-Fe-O compounds. The phase transition from the ferroelectric low temperature α-phase to the paraelectric β-phase takes place at around 825°C. The presence of an intermediate phase between the ferroelectric and paraelectric phase is still under discussion[107]. The paraelectric crystal structure is orthorhombic and centrosymmetric. The distortion from the ideal perovskite structure results from out-of-phase tilts of the oxygen octahedra along the [110] direction and in-phase tilts along the [001] direction (in pseudocubic notation). This is visualized in Figure 3.6. The symmetry is lowered to the *Pnma* space group no. 62. Finally, the coexistence of both phases at a finite temperature range and the sudden change in structural parameters confirms a first order phase transition[108].

[1] Reprinted figure with permission from R. Palai, R. S. Katiyar, H. Schmid, P. Tissot, S. J. Clark, J. Robertson, S. A. T. Redfern, G. Catalan, and J. F. Scott, Physical Review B, 77, pp. 014110 (2008). Copyright 2008 by the American Physical Society.

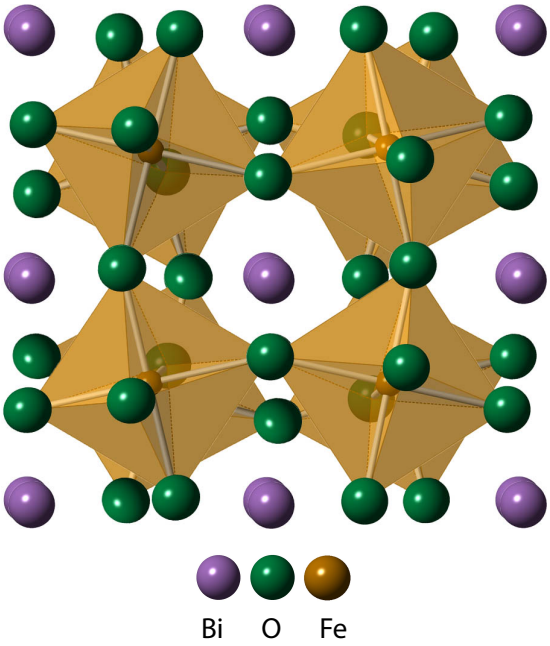

Figure 3.6 | Crystallographic $BiFeO_3$ unit cell in the paraelectric, i.e. the β-phase, with the *Pnma* structure illustrating the tilt and distortion of the oxygen octahedra.

A further increase of the temperature to around 925-933°C leads to the γ-phase. In this phase the $BiFeO_3$ unit cell is perfectly undistorted with $Pm\bar{3}m$ symmetry, as illustrated in Figure 3.3.

At temperatures higher than 961°C, the $BiFeO_3$ crystal decomposes.

The tilt of the FeO_6 octahedra also influences the bond angle (also known as buckling angle) between the oxygen ion and the two Fe ions. The bond angle is reduced along with the symmetry lowering. In the low temperature phase,i.e. in the α-phase with an $R3c$ structure, the bond angle is reduced to approximately 155°[109]. Whereas it is 180° in the undistorted γ-phase

$BiFeO_3$ is not only ferroelectric, but also a G-type antiferromagnet (i.e., a spin structure where both inter- and intra-plane coupling are antiferromagnetic) with a Néel temperature of T_N =640 K[110,111]. The magnetism is carried by the Fe^{3+} ions, which are coupled antiferromagnetically via superexchange through the p-orbitals of the O^{2-} atoms. Every Fe ion is surrounded by its six nearest neighbors with an opposite magnetic moment. The antiferromagnetic plane is illustrated (shaded) in Figure 3.7a). Neutron diffraction measurements revealed

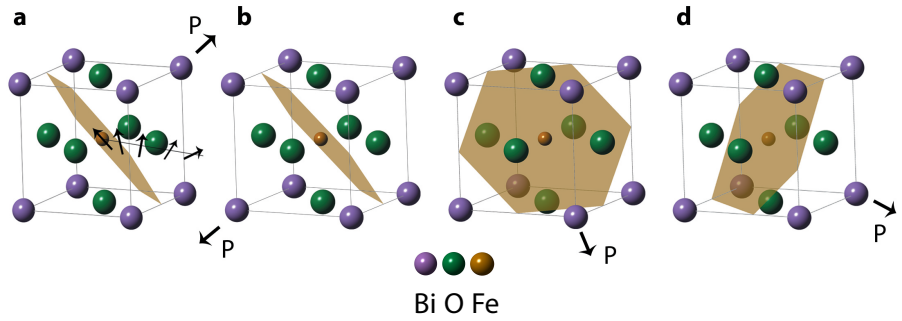

Figure 3.7 | a The $BiFeO_3$ unit cell before any electrical switching, the polarization *P* is along the [111] direction. The antiferromagnetic plane is shaded and the cycloidal spin structure is illustrated. **b** Shows the case with a reversed polarization by 180° using an externally-applied electrical field resulting in an unchanged antiferromagnetic plane. The antiferromagnetic plane for a polarization *P* along the 109° direction is illustrated in **c** and in the 71° direction in **d**.

that the magnetic moments follow a cycloidal structure with a wavelength of 62 nm[112,113].

Moreover, the distortion of the $BiFeO_3$ crystal leads to a canting of the moments, which results in a small ferromagnetic moment of the Dzyaloshinskii-Moriya type[27,28,114]. The direction of the ferromagnetic magnetization is perpendicular to both the antiferromagnetic axis and the direction of the ferroelectric polarization[115].

Materials that posses at least two ferroic orderings, e.g. (anti-)ferromagnetism and ferroelectricity, are denoted as multiferroic materials. Zhao *et al.*[19] reported that the orientation of the antiferromagnetic spins is coupled to the ferroelectric polarization in $BiFeO_3$ films and, thus, a polarization switching results in a change in the orientation of the antiferromagnetic ordering. The orientation of the antiferromagnetic sublattice is always perpendicular to the ferroelectric polarization. Figure 3.7 shows the dependence of the antiferromagnetic plane on the ferroelectric polarization direction. In 3.7b the polarization is reversed by 180° to the original state in Figure 3.7a, while the antiferromagnetic plane (shaded) has not changed. In Figure 3.7b and 3.7c the polarization was switched to 109° and 71°, respectively, leading to a switched antiferromagnetic plane, illustrated by the shaded planes, respectively.

By using a multilayered sample consisting of a $BiFeO_3$ layer coupled to a thin ferromagnetic material, it was reported that the magnetization direction of the ferromagnet can be rotated by switching the direction of the antiferromagnetic

plane of the $BiFeO_3$[116]. Furthermore, the stored information was non-volatile. The read-out of this state can easily be performed using the AMR effect. This electric-field-induced magnetic switching can improve the spintronic applications as it is not necessary to generate either magnetic fields in order to switch a magnetization direction or to generate a spin-polarized current for the switching process via an STT torque anymore and, thus, leads to a low power consumption. As the Néel temperature of $BiFeO_3$ is much higher than room temperature, this type of spintronic device is robust and can be used at ambient conditions.

$LaFeO_3$ was investigated as a second material. $LaFeO_3$ is comparable to $BiFeO_3$ with all Bi atoms replaced by La ions. The crystal structure, magnetic properties, and the ability of $LaFeO_3$ single crystals to generate an exchange bias is discussed in the next section.

3.2.2. The Orthoferrite $LaFeO_3$

$LaFeO_3$ belongs to the class of orthoferrites that is a subclass of perovskites. Orthoferrite materials have the same general formula ($RFeO_3$) as perovskites but instead of R being a transition metal, for orthoferrites, R has to be a rare-earth metal (La,…,Lu).

Orthoferrites have been intensively studied since the 1950s. Due to their optical transparency, their magnetic structure could be extensively investigated through the Farraday effect. These investigations uncovered that most of the perovskites are antiferromagnets with a small canting. The canting generates a small ferromagnetic contribution[117], resulting in magnetic bubble domains. This characteristic magnetic structure enabled the invention of the magnetic bubble memory[118], which is a non-volatile memory where the data is stored in small magnetized areas (bubbles) that form when an external magnetic field is applied. The read-out is realized by shifting the bubbles to the edge of the memory, where the magnetic bubble can be detected. The magnetic bubble memory was one of the most promising applications based on orthoferrite materials in the 1970s[119]. However, it never found its way into modern electronic devices. Nevertheless, it shows that orthoferrites might still offer a great potential for their use in spintronic devices.

As already seen for the perovskites, the crystallographic structure of the orthoferrites also depends on the ionic radii of the constituents. The ionic radius of the R^{3+} atoms (R=rare earth element) increases from La to Lu. Accordingly, the rhombic distortion from the cubic perovskite structure is smallest for $LaFeO_3$ and largest for $LuFeO_3$. The larger the distortion, the stronger the reduction of the Fe-O-Fe bond angle. Figure 3.8a presents experimental data proving

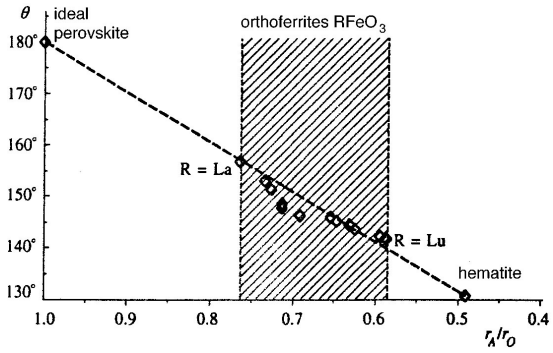

Figure 3.8 | The B-O-B valence bond angle in the structural series ABO_3 as function of the ratio r_A/r_O of the ion radii. The points are experimental values. The dashed line lies between the extreme members of the series, perovskite and hematite. The intermediate region which applies to the rare earth orthoferrite series $RFeO_3$ is shaded. The ion radii are taken from Belov and Bokiya.[1]

this behavior for the series of $RFeO_3$ as a function of ion radii r_A/r_O. The series ranges from the structure of the ideal perovskite with $r_A/r_O = 1$ (c.f. $SrTiO_3$) to hematite, i.e., Fe_2O_3.

As the ionic radii for La^{3+} and Bi^{3+} are nearly the same as for $BiFeO_3$ and $LaFeO_3$, the Goldschmidt tolerance factor is also similar. For $LaFeO_3$ it is t=0.94, while for $BiFeO_3$ it is $t = 0.913$. This leads to a reduced bond angle of about 155° for $LaFeO_3$ that is similar to the bond angle of $BiFeO_3$ in the *R*3*c* structure (α-phase)[120,121]. Thus, $BiFeO_3$ and $LaFeO_3$ are nearly at the same position in the graph in Figure 3.8.

Lyubutin *et al.*[122] have shown by using Mössbauer spectroscopy that the Néel temperature of the perovskites correlates with this bond angle. A reduced angle results in a weaker Fe-O-Fe exchange interaction and, thus, a reduced Néel temperature. The Néel temperature is 700-740 K for $LaFeO_3$ and 640 K for $BiFeO_3$ crystals[110,111,122,123].

Ferroelectric properties have also been observed for $LaFeO_3$ crystals[21] at room temperature. This is surprising because the ferroelectric $LaFeO_3$ crystallizes in the same *Pnma* structure with spacegroup no. 62 (c.f. Figure 3.6 with La atoms at the corner positions and a lattice parameter of a_{pc} = 3.93Å[124]),

[1]Journal of Experimental and Theoretical Physics, Dependence of exchange interactions on chemical bond angle in a structural series: Cubic perovskite-rhombic orthoferrite-rhombohedral hematite, 88, 1999, pp. 590, I. S. Lyubutin, T. V. Dmitrieva and A. S. Stepin. With permission of Springer.

as the paraelectric $BiFeO_3$. In the conventional theory, ferroelectricity should be forbidden for such a cento-symmetric unit cell. Hence, the origin of this polarization ordering is still poorly understood. A ferroelectric-to-paraelectric transition temperature for $LaFeO_3$ crystals is higher than 475 K and an exact value has not been determined[121].

The magnetic structure of $LaFeO_3$ is comparable to $BiFeO_3$. Both materials are antiferromagnets in which the Fe ions couple antiferromagnetically via superexchange via the *p*-orbitals of the O^{2-} atoms. A canting caused by the Dzyaloshinskii-Moriya interaction leads to weak ferromagnetism[120,124]. Furthermore, $LaFeO_3$ is, similar to $BiFeO_3$, transparent and insulating.

4 Analytical and Preparation Tools

The previous chapter introduced the physical basics for the techniques that provide experimental access to the properties of the investigate materials. The main focus lies on obtaining a deeper insight into the magnetic properties with particular interest in the magnetic anisotropies of thin film samples. Hence, this chapter deals with the fabrication techniques, as well as various methods for determining the crystallographic and magnetic properties of thin films. All three aspects are essential for obtaining improved materials for spintronic applications.

The foundation for the successful investigation of thin film samples is the choice of a reliable and reproducible deposition technique. Furthermore, the technique should be easily expandable to a larger numbers of samples, since its for application a high-quality production and a high output are desired. Accordingly, sputter deposition was used for the preparation of the samples. The sputtering system used for this work, as well as the critical parameters, are described in the first part of this chapter. It is inevitable to optimize the parameters for the deposition by extensively analyzing the crystallographic ordering and the stoichiometry. For this purpose, X-ray diffraction and X-ray florescence spectroscopy are used, which are shortly introduced in the second section of this chapter. The characterization of the magnetic properties of the optimized samples is conducted through measurements of the magneto-optic Kerr effect, which will also be discussed in the chapter. Based on the results of these table top magnetometry measurements, selected films have been investigated at the ALS in Berkeley. This synchrotron radiation facility allows to determine the hybridization states of the atoms via X-ray absorption spectroscopy, as well as the magnetic ordering via X-ray magnetic circular/linear dichroism. An overview on these X-ray techniques is given in the third section of this chapter. In the last section the ferromagnetic resonance technique is

introduced. This method yields information on the magnetization dynamics in the ferromagnetic thin films, i.e., in the Co-Fe-Si Heusler compounds, which cannot be provided by the aforementioned techniques.

4.1. Thin Film Deposition

The Heusler compounds, as well as the oxides, were prepared in a BesTec UHV sputtering chamber with a base pressure of $1 \cdot 10^{-9}$ mbar. A schematic drawing of this sputtering machine is given is Figure 4.1. The sputtering chamber is equipped with eight three-inch magnetron sputtering sources. In order to deposit insulating materials, two of the sources are connected to an RF power supply, while the other six are driven by a DC power supply. Furthermore, the sputtering chamber is equipped with an electron beam evaporator. In order to grow crystalline films, a sample heater allows the deposition at high temperatures of up to 1000°C. In this work, all films were grown by co-sputtering from elemental targets (Fe, Co, Si, Bi, and La). The $BiFeO_3$ and $LaFeO_3$ films were grown in a mixture of a high-purity oxygen and argon atmosphere. For the growth of $BiFeO_3$/Co-Fe multilayers, a home-built sample holder was used, allowing for the deposition of films in an applied magnetic field of 150 Oe at elevated temperatures with subsequent cooling of the sample in the presence of the magnetic field.

All films and bilayers were capped with insulating MgO layers with a thickness of 2 nm to protect the samples without affecting their electrical and magnetic properties.

To ensure optimum growth of the $Fe_{1+x}Co_{2-x}Si$, $BiFeO_3$ as well as $LaFeO_3$ films, single-crystalline substrates were used. Based on the lattice mismatch between the substrate and the deposited films, cubic MgO (001) and $SrTiO_3$ (001) substrates are an ideal choice to ensure a textured growth.

For the fabrication of the GMR stacks containing a $LaFeO_3$ layer, a second sputtering chamber was used. The $LaFeO_3$ films were grown in the BesTec sputtering chamber. After the deposition, the films were transferred to a Leybold CLAB 600 sputtering system (base pressure 10^{-7} mbar) without vacuum break to deposit the $Co_{70}Fe_{30}$/Cu/$Co_{70}Fe_{30}$ layers, as this sputtering machine allows for a more accurate control of shutter times and, thus, film thicknesses. This is crucial to accurately tune the thickness of the Cu spacer. Moreover, it complements the BesTec system by an additional 6 sputtering sources, providing a higher variability for the choice of capping layers.

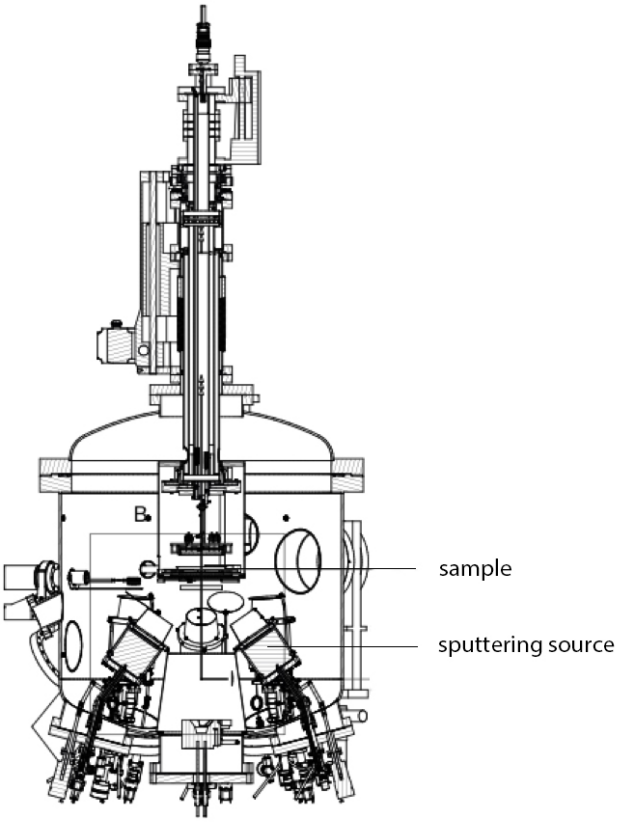

Figure 4.1 | Schematic view of the BesTec sputtering system.

Adjacent to the film growth of the samples, X-ray diffraction was conducted to determine the structure of the films. As this is an important technique for the growth of the samples, it is introduced in the following section.

4.2. Structural Characterization

4.2.1. X-Ray Diffraction

In this work X-ray diffraction (XRD) was extensively used in order to determine the crystallographic orientation and the crystallinity of the films. A comparison of the peak intensities allows a determination of the crystallographic ordering of the samples. This technique is widely known[125] and therefore only briefly addressed in this thesis.

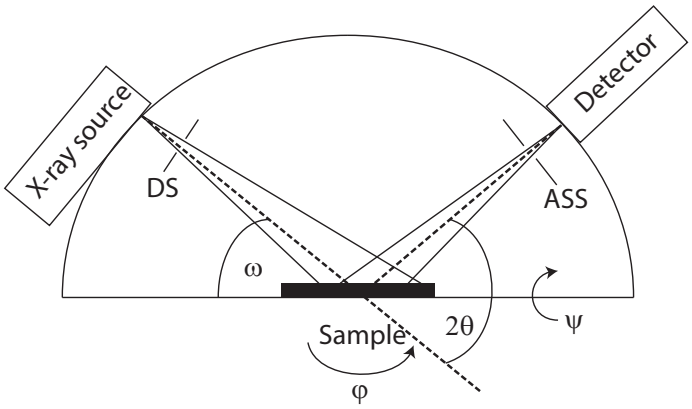

Figure 4.2 | Bragg Brentano arrangement for the XRD and XRR measurements. Illustrated is the beam path along with the definition of the angles.

For an X-ray diffraction measurement, the sample is irradiated with X-rays under different angles. In the case of a constructive interference in the specimen, due to suitable interplanar spacing of the crystallographic lattice, a diffraction peak is measured by the detector. A sketch of the used setup is given in Figure 4.2. For symmetric scans with $\theta = \omega$ the following condition, also known as Bragg equation[126],has to be fulfilled in order to observe a diffraction peak:

$$n\lambda = 2d_{\mathrm{hkl}} \sin\theta, \tag{4.1}$$

with an integer number n, λ represents the wavelength of the X-rays and the interplanar spacing d_{hkl} in direction [hkl].

For this work, a Phillips X'pert Pro MPD diffractometer with a copper anode (effective wavelength of λ = 1.54187 Å), was used. The X-ray source, the detector and the sample are arranged in Bragg-Brentano geometry. Both the X-ray source and the detector move at equidistant angles with respect to the sample surface. The incident X-ray beam is controlled by an automatic divergence slit (DS), which allows an illumination of the sample either with a fixed divergence or with a constant irradiated area of the sample. An analogous optic in the diffracted beam path, i.e. the anti-scatter slit ASS) allows the investigation of a defined area of the sample. Standard XRD scans were performed by irradiating a constant area of the sample in order to obtain a high signal-to-noise ratio for all angles.

In order to observe the films' off-specular reflections, an open Eulerian cradle with collimator point-focus was used that allows for a full rotation as well as

tilting of the sample. Moreover, this allows an investigation of the epitaxy of the films by a rotation of the sample.

In order to grow films with a defined thickness, X-ray reflectivity measurements were conducted to determine the correct shutter times. As for this type of measurement the sample is irradiated at small angles with a fixed divergence of the beam, it is conducted in the same setup as the XRD measurements. This technique is addressed in the following section.

4.2.2. X-Ray Reflectivity

For an X-ray reflectivity (XRR) measurement the sample is irradiated under small angles usually around $0 < 2\theta < 5°$ with varying 2θ angle. For angles larger than the critical angle of the film(s), which is proportional to the square root of the density $\sqrt{\rho}$ of the film(s), an interference between the involved interfaces results in a pattern with so-called Kiessig fringes[127]. The observed pattern becomes less pronounced when the interfaces of the investigated films is rough. According to the Parratt[128] algorithm, the thickness of the film can be determined from the distance between the oscillation maxima θ_n and θ_{n+1}. The relation between the maxima is given by:

$$\theta_n^2 = \frac{(\theta_{n+1}^2 - \theta_{n-1}^2)^2}{12(\frac{\lambda}{2d})^2} + \theta_c^2 \tag{4.2}$$

with the critical angle θ_c, at which the X-rays can penetrate into the film.

The slope of θ_n^2 as a function $(\theta_{n+1}^2 - \theta_{n-1}^2)^2$ is proportional to the layer thickness.

Thus, this technique can be used to determine the thickness of the films as well as their roughnesses along with their density. With the help of these measurements, the deposition times can be determined in order to deposit films with a defined thickness.

Another important tool for the deposition of stoichiometric films is the X-ray fluorescence spectroscopy, which will be addressed in the following section.

4.2.3. X-Ray Fluorescence

In order to determine the stoichiometry of the films and thus, to adjust the correct sputtering powers for the growth of stoichiometric films, X-ray fluorescence (XRF) spectroscopy is used. For this type of measurement the sample is irradiated with hard X-rays in a He-atmosphere, which enables the detection of light elements without the use of a vacuum setup. If the energy of the incident

beam is sufficiently high enough to excite the electrons of the atoms of the sample into the continuum, the resulting vacancy is filled by electrons from higher levels, which generates either an Auger electron or a fluorescence photon. The emitted fluorescence photons are detected using an Amptek XR-100CR Si-PIN detector with a digital pulse processor. As the energy of the fluorescence photons is element-specific, it is possible to determine the composition of the films. This technique can only be used for the detection of elements with an atomic number larger than approximately 14, which corresponds to Si, as the probability of the generation of a fluorescence photon, i.e. the fluorescence yield, is proportional to the element's atomic number.

A Fundamental Parameter Analysis[129,130] is applied to the spectrum after the removal of the background, the sum- and escape-peaks, in order to determine the composition of the investigated sample.

These X-ray-based techniques were used for the determination of the deposition parameters. Selected samples were analyzed using additional tools, such as the atomic force microscope, which is introduced in the following section.

4.2.4. Atomic Force Microscopy

To determine the surface topology of the films and to prove their suitability for their implementation in devices, atomic force microscopy (AFM) was used. The measurements were performed in a Bruker Multimode 5 in contact mode with a constant applied force. The resulting roughness values are given as root mean square (RMS) roughness, which is calculated by:

$$R_{\mathrm{RMS}} = \sqrt{\frac{1}{N}\sum_{n=1}^{N}(z_n - \bar{z})^2}, \tag{4.3}$$

where N denotes the number of the data points with the corresponding heights Z_n. The mean of the heights is denoted by $\bar{z}$.

The description of the AFM completes the presentation of the techniques used to analyze the structural properties of the samples. The following sections will deal with the tools used to investigate the magnetism of the samples.

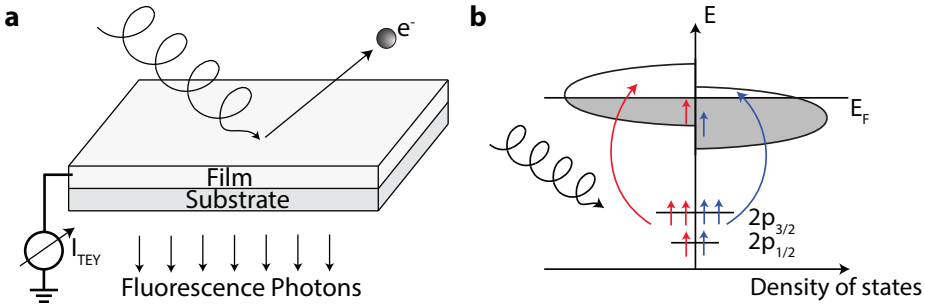

Figure 4.3 | a The principle of an XAS measurement in electron yield and visible light fluorescence technique and **b** the XMCD principle.

Table 4.1 | X-ray absorption edges and transitions.

Absorption line	Transition
K	$1s \rightarrow 4d_{1/2}$
L_2	$2p_{1/2} \rightarrow 3d_{3/2}, 4s$
L_3	$2p_{3/2} \rightarrow 3d_{3/2,5/2,4s}$

4.3. X-Ray Absorption Techniques

As one main focus of this work is the investigation of the magnetic properties of the films, this section will introduce a powerful technique to determine the element-specific properties[131,132]. The polarized synchrotron radiation in the soft X-ray regime can be used to get insights into the magnetic and electrical properties such as the hybridization state. For this type of measurement, the sample is irradiated with a beam of polarized X-rays with tunable energy. This excites electrons from deep core states into the continuum. A summary of important excitations (considering the dipole selection rules) along with their notations is given in Table 4.1. This, on the one hand, generates photo electrons emitted from the sample and, on the other hand, creates fluorescence photons.

There are two methods to measure the signal. In case of a metallic sample the absorption of the X-rays can be determined by measuring the sample drain current. This principle is illustrated in Figure 4.3a. The excitation of photoelectrons takes place in the range of a few 100Å[133], which is why this method is surface-sensitive and can be used to study the film's oxidation.

The second method is to detect the luminescence of the substrate, which is caused by the transmitted photons in the investigated film, as illustrated

in Figure 4.3a[134]. For this type of measurement, MgO substrates posses suitable energy levels to generate photons in the visible range, by excitation of the photons emitted from the observed film, while $SrTiO_3$ substrates are not suitable. Therefore, this method is more sensitive to the magnetic properties of the whole film and can also be used for insulating films. However, the film thickness is limited, such that the intensity of the X-rays transmitted by the investigated film is high enough to excite the substrate.

The measurements presented in this work are performed at Beamline 4.0.2. of the Advanced Light Source in Berkeley, CA, USA. The used polarization defines the different types of measurement, which can be used for the investigation of different electric and magnetic properties. This will de addressed in the following sections.

4.3.1. X-ray Absorption Spectroscopy

In order to obtain information about the electronic structure of the films, i.e., the hybridization state of the atoms, X-ray absorption spectroscopy (XAS) measurements are an ideal choice. For this type of measurements, the sample is irradiated with circularly-polarized light as a function of the energy of the X-rays. At every energy, a pair of spectra is recorded, which can either be given between left- and right-polarization of the beam or by different magnetization directions of the sample (obtained by an externally-applied magnetic field) for a given helicity. These two spectra are denoted by $\mu^+(E)$ and $\mu^-(E)$. The XAS signal is defined as the mean of both components:

$$\mathrm{XAS}(E) \quad = \quad \frac{1}{2}(\mu^+(E) + \mu^-(E)). \tag{4.4}$$

This method gives information, among others, about the oxidation (state) of the atoms or the hybridization state. However, it provides no information about the magnetic properties of the material. The following section will discuss measurement techniques in order to obtain the samples' magnetic information.

4.3.2. X-Ray Magnetic Circular Dichroism

Information about the magnetic properties of the specimen is given by the difference of the spectra. The XMCD signal is defined as the difference between both helicitites/magnetization direction as a function of energy:

$$\mathrm{XMCD}(E) = \mu^+(E) - \mu^-(E). \tag{4.5}$$

An XMCD signal is observed when an imbalance between spin-up and spin-down *d*-states is present and, thus, when the investigated material is ferromagnetic, as electrons are excited from core *p*-states to *d*-states above the Fermi-energy. This process is illustrated in Figure 4.3b. Using the XMCD signal the spin and orbital magnetic moments of the elements can be determined by applying the XMCD sum rules[135,136].

This is a powerful technique to investigate the element-specific magnetic properties of ferromagnetic films. However, for the investigation of antiferromagnetic films, which is one of the main topics of this dissertation, a slightly modified technique has to be applied. This will be presented in the following section.

4.3.3. X-Ray (Magnetic) Linear Dichroism

As circular-polarized X-rays can be used for the investigation of ferromagnetism, a linear-polarized beam of X-rays can be used to study the direction of the spins, which are coupled to the orientation of the lattice. Thus, this technique can be used to study materials such as antiferromagnets or ferrimagnets. The dichroic signal can also be obtained either by switching of the polarization between parallel- and antiparallel-polarization with respect to the sample surface for a fixed magnetization direction or by magnetizing the sample along two directions while keeping the polarization of the beam fixed. The first method, illustrated in Figure 4.4, is referred to as XLD as no magnetic switching takes place[137]. This is especially applicable when investigating antiferromagnets and samples with high switching fields. In analogy to the XMCD principle, the X(M)LD signal is defined as the difference between both spectra:

$$\mathrm{X(M)LD}(E) = \mu^{\parallel}(E) - \mu^{\perp}(E). \tag{4.6}$$

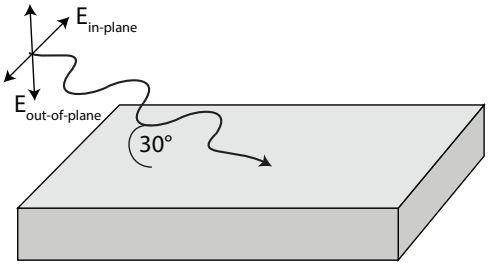

Figure 4.4 | Measurement principle for an XLD measurement: the polarization of the linear-polarized light is switched between the in-plane and out-of-plane direction.

The X(M)LD signal results from charge anisotropies around the absorbing atoms and is caused by spin-orbit and exchange interactions. If the asymmetric charge distribution is caused by the bonding properties of the atom, this is referred to as natural linear dichroism. If the asymmetry is related to the magnetic properties of the atom, the effect is called magnetic linear dichroism[131].

Due to limited beam times, these methods were only applied to selected samples. In the following section, the magneto-optic Kerr-Effect magnetometry technique is presented, as this was used for detailed studies of the magnetic properties of the grown films in this work.

4.4. Magneto-Optic Kerr-Effect

In 1877 the magneto-optic Kerr-effect[138,139] was discovered by John Kerr[140], who reported that a beam of light changes its polarization direction when reflected at a surface of a magnetic material. Additionally, a linearly-polarized incident beam becomes elliptically-polarized during reflection. The reflected beam can be described by the Kerr angle, i.e. the angle at which the polarization is rotated, along with the Kerr ellipticity. Both effect amplitudes are nearly proportional to the magnetization $\vec{M}$ of the sample, which allows the indirect measurement of the magnetization by the determination of the Kerr angle θ or ellipticity a/b. The measurement principle is shown in Figure 4.5, which illustrates the $\vec{E}$-field vector of both the incident and the reflected beam path along with the rotation of the $\vec{E}$-field vector by $\vec{K}$ and the definition of the ellipticity a/b.

In general, the dielectric law connects the electric field vector $\vec{E}$ of the incident light with the induced electrical displacement $\vec{D}$ in the sample by:

$$\vec{D} = \varepsilon_{ij}\vec{E}, \tag{4.7}$$

where ε_{ij} denotes the generalized dielectric permittivity that can be written as[141–143]:

$$\varepsilon_{ij} = \varepsilon \begin{bmatrix} 1 & -iQ_v m_3 & iQ_v m_2 \\ iQ_v m_3 & 1 & -iQ_v m_1 \\ -iQ_v m_2 & iQ_v m_1 & 1 \end{bmatrix} + \begin{bmatrix} B_1 m_1^2 & B_2 m_1 m_2 & B_2 m_1 m_3 \\ B_2 m_1 m_2 & B_1 m_2^2 & B_2 m_2 m_3 \\ B_2 m_1 m_3 & B_2 m_2 m_3 & B_1 m_3^2 \end{bmatrix}, \tag{4.8}$$

with the regular dielectric constant ε and the components of the magnetization

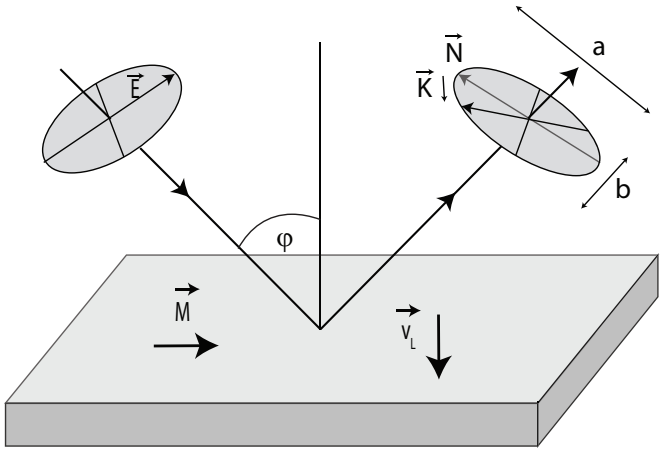

Figure 4.5 | The MOKE principle. The direction of the incident $\vec{E}$ and normally reflected electric field vector $\vec{N}$ are shown. The Kerr amplutide $\vec{K}$ results in the rotation of the $\vec{E}$ vector. The magnetization direction $\vec{M}$ as well as the vibrational motion of the electrons $\vec{v_L}$ are illustrated.

along the cubic axis m_i. The parameters Q_v, B_1 and B_2 describe the Voigt effect and are more complex and mostly unknown.

The electrical displacement $\vec{D}$ can be interpreted as the reflected light amplitude. Along with Equation 4.7, the reflected beam $\vec{D}$ influenced by the interaction between the electric field vector $\vec{E}$ of the incident beam and the magnetization $\vec{M}$ of the sample can be written as:

$$\vec{D} = \varepsilon(\vec{E} + iQ_v\vec{M} \times \vec{E}). \tag{4.9}$$

Thus, this measurement is proportional to the magnetization $\vec{M}$ of the sample. Moreover, the cross product $\vec{M} \times \vec{E}$ shows the gyroelectric origin of the Kerr effect and the analogy to the Lorentz force.

Figure 4.5 illustrates the origin of the polarization rotation for the case of a longitudinal MOKE setup, where the magnetization direction lies in the plane of the sample and parallel to the direction of the incident beam. The incident beam is polarized parallel to the plane of incidence. The electric field $\vec{E}$ of the incident beam leads, along with magnetization $\vec{M}$ due to the Lorentz force, to a vibrational movement of the electrons in the specimen, denoted by $\vec{v}_L$. A projection of the movement onto the plane perpendicular to the direction of the reflected beam generates the Kerr amplitude $\vec{K}$. The interference between the unaffected, reflected beam $\vec{N}$ and $\vec{K}$ leads to a small Kerr (polarization) rotation θ.

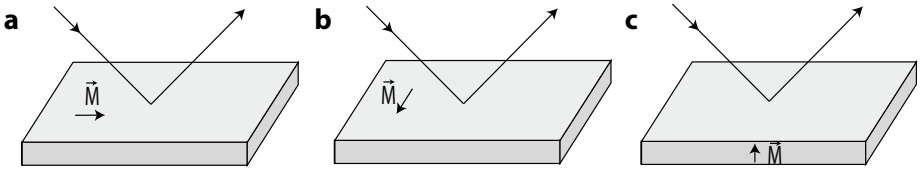

Figure 4.6 | Different MOKE geometries depending on the direction on the magnetization $\vec{M}$ direction: **a** LMOKE, **b** TMOKE, **c** PMOKE.

Basically, there are three kinds of different measurement geometries for a MOKE measurement, as summarized in Figure 4.6:

a Shows the geometry for the measurement of the longitudinal MOKE (LMOKE) effect. The magnetization direction $\vec{M}$ of the film is parallel to both the incident and the reflected beam. This geometry is suitable for the investigation of samples with in-plane anisotropy/magnetization. The reflected beam contains information about the Kerr rotation as well as the Kerr ellipticity.

b Describes the transversal MOKE (TMOKE) geometry. The magnetization $\vec{M}$ lies in the plane of the sample and is perpendicular to the incident beam. The magnetic response of the sample causes only an intensity change in the reflected beam but no Kerr rotation.

c Depicts the case for an out-of-plane magnetization of the sample. This measurement geometry is called polar MOKE (PMOKE). The reflected beam contains information about both the Kerr rotation and Kerr ellipticity.

Moreover, the magnitude of the Kerr effect depends on the angle between the incident beam and the sample, as well as the polarization of the beam. The incident beam can either be *s*- or *p*-polarized light, where *s*-polarization means that the electric field $\vec{E}$ is oscillating normally to the plane of incidence, while *p*-polarization denotes a wave with an electric field vector $\vec{E}$ parallel to the plane of incidence.

The measurements of the magneto-optic Kerr-effect in this work were performed using two different setups. The investigations of the $BiFeO_3$ and $LaFeO_3$ films were done in a setup with an incident angle of 13° and a 650 nm laser, while the $Fe_{1+x}Co_{2-x}Si$ samples were measured in a setup with an angle of 45° using a laser with a wavelength of 488 nm. Hence, the measured intensity is a mixture of the longitudinal and the transverse MOKE effect. In both setups, the incident beam was *s*-polarized. For the investigations of the anisotropy

distributions of the $BiFeO_3$ and $LaFeO_3$ films, a home-built sample holder was constructed, which allows for a precise rotation of the sample along with the ability of a tilting of the sample carrier in order to ensure a perfect alignment of the sample with respect to the laser.

With this technique, the static properties of the films were investigated. In order to analyze the magnetization dynamics along with the magnetic damping of the films, the ferromagnetic resonance technique was applied. This technique is discussed in the following section.

4.5. Ferromagnetic Resonance

The ferromagnetic resonance (FMR) technique[68] is used to gain information about the magnetization dynamics of the samples, including the determination of the damping of the ferromagnetic films. For this type of measurement the sample is placed in a static magnetic field $\vec{H}_{DC}$, while an alternating AC field $\vec{H}_{RF}$ is applied perpendicularly to $\vec{H}_{DC}$. The AC field drives the precession of the magnetization $\vec{M}$ around the direction of the external field H_{DC} (as introduced in Figure 2.13) while its field strength is swept. A schematic illustration of the setup is shown in Figure 4.7a. The resonance frequency is reached when the AC field matches the precession of the $\vec{M}$, this is denoted as resonance frequency. In this case, the energy of the AC field is absorbed in the sample at a certain external field denoted by $\vec{H}_R$. The sample is placed at the end of a shorted waveguide and the absorbed power P_A is measured, which is proportional to the complex

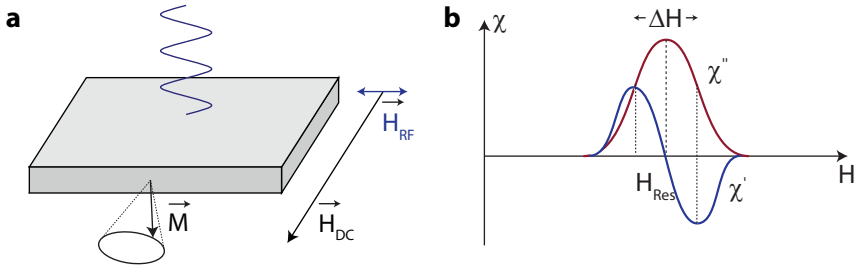

Figure 4.7 | a FMR measurement principle and **b** illustration of the susceptibility χ. The complex part shows a maximum at the resonance frequency H_{Res}. The linewidth ΔH is also marked.

part of the susceptibility χ of the magnetic material in the externally-applied field $\vec{H}$:

$$\vec{M} \propto \chi\vec{H} = (\chi' + i\chi'')\vec{H} \tag{4.10}$$

$$P_{\mathrm{A}} \propto \chi''. \tag{4.11}$$

Figure 4.7b is an illustration of the susceptibility as a function of the externally-applied field. The absorption line exhibits a broadening that is referred to as linewidth ΔH. Least square fits of χ' using a first derivative of a Lorentzian line shape were done to precisely determine the resonance field $\vec{H}_{\mathrm{res}}$, as well as the peak-to-peak linewidth ΔH.

This section follows up on to the theoretical description of the dynamics in Section 2.5. The resonance condition can be expressed in terms of the second derivatives of the free-energy-density E by the Smit-Beljers formula[144] based on the the Landau-Lifshitz-Gilbert equation (2.23):

$$\left(\frac{f}{\gamma'}\right)^2 = \frac{1}{(M\sin\theta)^2}\left[\frac{\partial^2 E}{\partial\theta^2}\frac{\partial^2 E}{\partial\varphi^2} - \left(\frac{\partial^2 E}{\partial\theta\partial\varphi}\right)^2\right]\Bigg|_{\theta_0,\varphi_0}, \tag{4.12}$$

where $\gamma' = \gamma/2\pi$, θ and φ are the polar and azimuthal angles of the magnetization $\vec{M}$, as shown in Figure 2.3, while θ_0 and φ_0 represent the corresponding equilibrium values. Hence, this equation has to be evaluated at the equilibrium conditions:

$$\frac{\partial E}{\partial\theta} = 0 \text{ and} \tag{4.13}$$

$$\frac{\partial E}{\partial\varphi} = 0 \tag{4.14}$$

When the system is in resonance, the dependency of the angular frequency $\omega = 2\pi f$ with the frequency f from the magnetic field is given by the Kittel formula[145]. Neglecting any anisotropies this yields:

$$\omega = \gamma' H_{\mathrm{Res}}\sqrt{H_{\mathrm{Res}} + 4\pi\mu_0 M_{\mathrm{eff}}} \tag{4.15}$$

with the resonant field H_{Res} and $\gamma' = \gamma/2\pi$. M_{eff} denotes the effective magnetization of the sample.

Moreover, the ferromagnetic resonance technique can be used to determine the anisotropy distribution of the sample. In the case of an in-plane fourfold anisotropy distribution, e.g., present in materials with a cubic crystallographic

structure, a determination of the fourfold anisotropy field can be conducted by FMR measurements along the sample's magnetic easy and hard axes. A simultaneous fit of the measured data to the Kittel equations for both easy and hard magnetic configurations gives information about the magnitude of the fourfold anisotropy field and the effective magnetization M_{eff} of the sample[146]:

$$f = \gamma' \sqrt{(H_{\mathrm{res-ha}} - H_4)(H_{\mathrm{res-ha}} + \frac{H_4}{2} + 4\pi M_{\mathrm{eff}})} \tag{4.16}$$

$$f = \gamma' \sqrt{(H_{\mathrm{res-ea}} + H_4)(H_{\mathrm{res-ea}} + H_4 + 4\pi M_{\mathrm{eff}})} \tag{4.17}$$

where M_{eff}, γ', and H_4 are shared fit parameters. H_4 describes the magnitude of the in-plane fourfold anisotropy field. $H_{\mathrm{res-ha}}$ and $H_{\mathrm{res-ea}}$ denote the resonance field along the magnetic hard and the easy axes, respectively.

The information about the magnetic relaxation of the precessional motion of the magnetization $\vec{M}$ is given by the frequency-dependence of the linewidth of the ferromagnetic resonance absorption. The frequency-dependence of the linewidth[147,148] can, under certain conditions, be characterized by an inhomogeneous residual linewidth at zero field ΔH_0 and an intrinsic contribution:

$$\Delta H = \Delta H_0 + \frac{2}{\sqrt{3}} \frac{\alpha_{\mathrm{eff}}}{\gamma'} f, \tag{4.18}$$

where α_{eff} is the effective damping parameter. Thus, for a correct determination of the effective damping parameter, it is necessary to measure the linewidth over a wide frequency range to determine the slope. It is not sufficient to measure ΔH at a fixed frequency, because a non-zero extrinsic linewidth ΔH_0 results in an overestimated damping parameter α_{eff}.

In this work the ferromagnetic $Fe_{1+x}Co_{2-x}Si$ Heusler compounds were investigated using a FMR broadband coplanar waveguide setup up with a maximum frequency of 40 GHz, as these materials are promising candidates for the use in spintronic applications such as MRAMs. The following chapter will present the experimental data obtained from the various magnetic investigations, starting with the results of the $Fe_{1+x}Co_{2-x}Si$ films.

5 Magnetization Dynamics in Co-Fe-Si Films

The previous chapters introduced the physical basics along with a presentation of the measurement techniques used in this work. The following chapters will present the results of the magnetic measurements of the $Fe_{1+x}Co_{2-x}Si$, $BiFeO_3$ and $LaFeO_3$ films, which were also introduced in the previous chapters.

This chapter focusses on the crystallographic and magnetic properties of the stoichiometric series, ranging from Co_2FeSi to Fe_2CoSi Heusler compounds. These compounds are promising candidates for the use in future spintronic devices as they are reported to be half-metallic and, thus, exhibit high signal amplitudes. Moreover, Co-based Heusler compounds exhibit high Curie temperatures, which is also ideal for commercial applications. This chapter presents the investigation of crystallographic and magnetic properties of the Co-Fe-Si films, along with a discussion of their applicability in spintronic devices. The first part of this chapter deals with the preparation of the $Fe_{1+x}Co_{2-x}Si$ films along a with the discussion of their crystallographic properties. Afterwards, the studies performed on magnetic tunnel junctions containing an $Fe_{1+x}Co_{2-x}Si$ electrode are summarized for the sake of completeness. These measurements have been published in Reference[14]. The following part of the chapter presents detailed investigations of the magnetization dynamics and anisotropy distributions in the Co-Fe-Si films. These results are published in Reference[15].

5.1. Sample Preparation

The thin $Fe_{1+x}Co_{2-x}Si$ (x=0, 0.25, 0.5, 0.75, 1) films were grown using sputter deposition from elemental Co, Fe, and Si targets as described in Section 4.1. In order to achieve highly epitaxial films, MgO (001) substrates were used. Additional MgO and Cr seed layers were deposited to accommodate small lattice

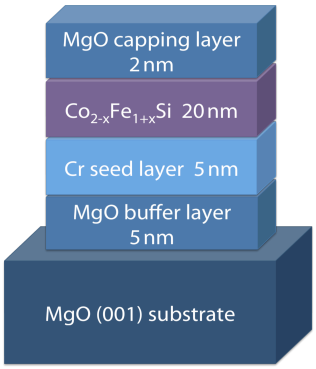

Figure 5.1 | Sketch of the investigated Co-Fe-Si Heusler films grown on MgO (001) substrates with additional MgO and Cr seed layers.

mismatches and to promote coherent and epitaxial growth. The Cr seed layer has a lattice parameter of 2.885 Å, which grows in 45° direction on the MgO layer with a lattice parameter of 4.212 Å. As introduced in Section 3.1, the lattice parameters for Co_2FeSi and Fe_2CoSi are 5.64 Å and 5.645 Å, respectively. This results in a lattice mismatch between one unit cell of the Heusler compound with two unit cells of Cr (2 × 2.885 Å) of about 2%. The 5 nm thick MgO and Cr films were annealed *in situ* at 700°C to obtain smooth surfaces. $Fe_{1+x}Co_{2-x}Si$ films with a thickness of 20 nm were deposited at room temperature and vacuum annealed *ex situ* at 500°C, as this is the optimal deposition temperature, determined in a previous work[13]. The correct sputtering powers for the Co, Fe,

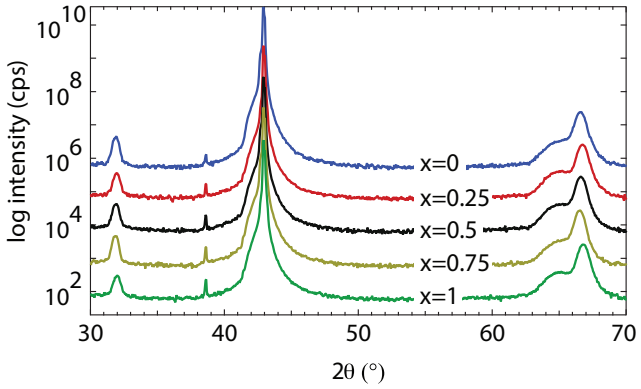

Figure 5.2 | X-ray diffraction pattern for all stoichiometries in $Fe_{1+x}Co_{2-x}Si$. The (002) and (004) peaks of the Heusler films can be found at 32° and 66.6°, respectively.

and Si targets were determined using XRF spectroscopy. Afterwards, a 2 nm thick MgO capping layer was used to prevent degradation of the films. Figure 5.1 presents a sketch of the investigated film stack in this work.

The following section will focus on the crystallographic properties of the stoichiometric series.

5.2. Crystallographic Properties

X-ray diffraction measurements were conducted to investigate the crystallographic properties of the $Fe_{1+x}Co_{2-x}Si$ films. The according XRD patterns for all films are presented in Figure 5.2, in which the (002) and (004) peaks of the Heusler compound are located around 2θ=32° and 66.6°, respectively. In the lower angle shoulder of the Heusler (004) peak, the (002) peak of the Cr buffer can be found at 65°. There are no differences in the pattern for the Co_2FeSi films in the $L2_1$ structure and Fe_2CoSi films in the X_a structure, as the atomic scattering factors for Co and Fe are nearly the same for this energy. Measurements of the off-specular (111), (422), and (444) peaks in previous works revealed high ordering parameters, based on the intermixing between the Co and Si, as well as the Fe and Si atoms[14]. The ordering is found to be high for Co_2FeSi and decreases when going to Fe_2CoSi. In order to test the films for crystallographic symmetry, φ scans are performed on the (220) planes of the $Fe_{1+x}Co_{2-x}Si$ films. Figure 5.3 shows the results along with the (220) plane of the MgO (001) substrate. The resulting scans show that the (100) Heusler plane is rotated by 45° with respect to the MgO (100) plane. The fourfold symmetry

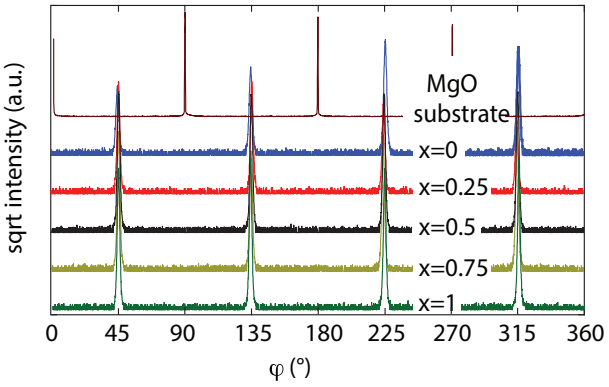

Figure 5.3 | φ-scans of the (220) $Fe_{1+x}Co_{2-x}Si$ peak and (220) MgO substrate peak showing the fourfold symmetry of the films.

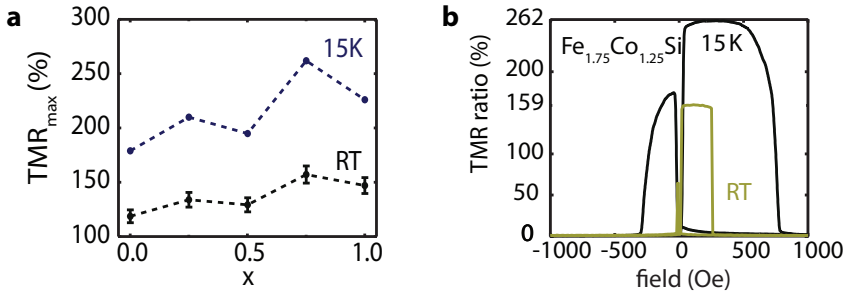

Figure 5.4 | a TMR ratio of MTJs based on the $Fe_{1+x}Co_{2-x}Si$ films measured at room temperature and 15 K, respectively. **b** Major loops for $Fe_{1.75}Co_{1.25}Si$ measured at room temperature and 15 K.

of the φ-scans clearly verifies the highly textured growth of all $Fe_{1+x}Co_{2-x}Si$ films in this study. Thus, the XRD measurements revealed that the films are highly-epitaxial and single-crystalline. In the following sections the integration of these films in magnetic tunnel junctions and the investigation of the magnetic properties will be presented.

5.3. TMR Effect In Co-Fe-Si-Based Magnetic Tunnel Junctions

This section summarizes the results of the integration of $Fe_{1+x}Co_{2-x}Si$ films into magnetic tunnel junctions, which was investigated in previous works[13,14]. The layer stacks were grown as follows: MgO (100) substrate/5 nm MgO/5 nm MgO/20 nm $Fe_{1+x}Co_{2-x}Si$/2 nm MgO/5 nm $Co_{70}Fe_{30}$/10 nm $Mn_{83}Ir_{17}$/25 nm Ru. The MTJs were patterned using UV lithography into structure of $(10 \times 10)\mu m^2$. Figure 5.4a presents the resulting TMR ratios measured at room temperature and at 15 K for all $Fe_{1+x}Co_{2-x}Si$ films with x=0, 0.25, 0.5, 0.75, 1. The highest TMR ratio was observed at the intermediate stoichiometry $Fe_{1.75}Co_{1.25}Si$ with 159% at room temperature and 262% at 15 K. The corresponding major loops are presented in Figure 5.4b. A possible explanation for this very high TMR ratio $Fe_{1.75}Co_{1.25}Si$ is that the Fermi energy at this stoichiometry is placed exactly inside the (pseudo-)gap around -0.5 eV in Figure 3.2a. Disregarding the bumps, the TMR ratio increases with higher amount of Fe. For Co_2FeSi the TMR ratio is 119% and 147% for Fe_2CoSi at room temperature, respectively.

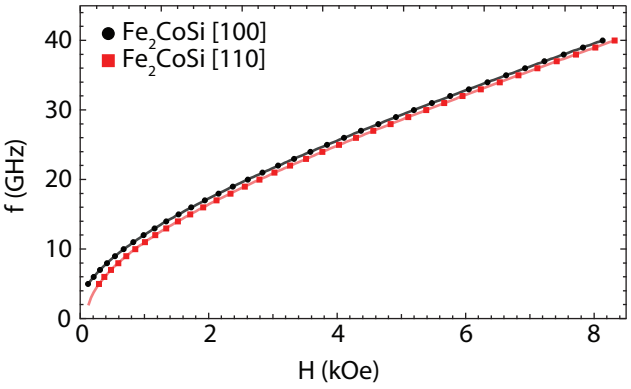

Figure 5.5 | Resonance frequency versus magnetic field (Kittel plot) along the in-plane magnetic hard [110] and the magnetic easy [100] axis for Fe_2CoSi. The experimental data are fitted using a combined fit (Equations 4.16 and 4.17) to determine M_{eff} and γ'.

This section summarized the measured TMR effect in $Fe_{1+x}Co_{2-x}Si$ based MTJs for the sake of completeness. The following sections focus on the magnetic properties of the Heusler films including the magnetization dynamics.

5.4. Magnetization Dynamics

This section presents the results of the magnetization dynamics of the thin $Fe_{1+x}Co_{2-x}Si$ films obtained from in-plane broadband ferromagnetic resonance measurements. According to the introduction into the FMR technique in Section 4.5, the resonance frequency was determined as a function of the applied magnetic field $\vec{H}$ for all samples in order to determine the effective magnetization M_{eff} and the gyromagnetic ratio γ'. For an estimation of the magnitude of the in-plane fourfold anisotropy field, the measurements were performed in two directions: in [100] and [110] direction of the $Fe_{1+x}Co_{2-x}Si$ Heusler compound, as the [100] direction is the magnetic easy axis and the [110] direction the magnetic hard axis, respectively. Figure 5.5 shows the exemplary Kittel plots along [100] and [110] directions for the Fe_2CoSi sample. Both curves were simultaneously fitted to Equations 4.16 and 4.17. The results of these fits for the gyromagnetic ratio γ' are presented in Figure 5.9a for all x in $Fe_{1+x}Co_{2-x}Si$. Within the error bars it is nearly linear for $x \geq 0.25$ and slightly smaller for Co_2FeSi. The fitted effective magnetization, which includes any perpendicular anisotropy present in the films, is shown in Figure 5.6 for the $Fe_{1+x}Co_{2-x}Si$ samples. The error

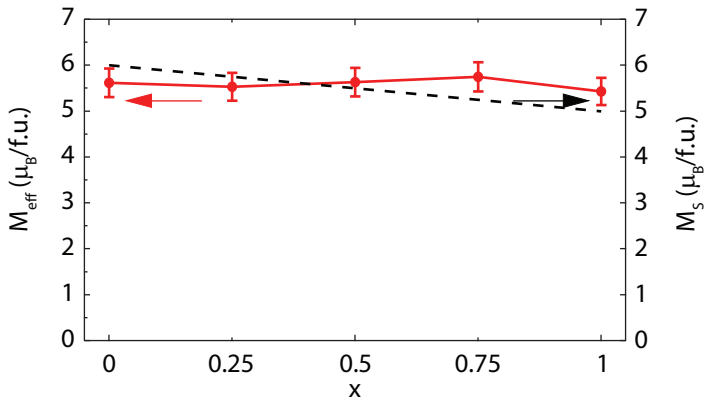

Figure 5.6 | Dependence of the fitted effective magnetic moment per formula unit for $Fe_{1+x}Co_{2-x}Si$ films with x=0, 0.25, 0.5, 0.75, 1 shown on the left axis. The dashed line shows the interpolated expected magnetic moments according to the Slater-Pauling rule (right axis).

bars originate from the fitting of the Kittel equations and the determination of the volume of the unit cell. For bulk Co_2FeSi and Fe_2CoSi, the experimentally determined magnetizations are 5.95 μ_B/f.u.[92] and 4.99 μ_B/f.u.[93], respectively, which match the expected saturation magnetizations according to the Slater-Pauling rule (visualized by the dashed line in Figure 5.6 on the right axis). The deviation from the expected values might be attributed to residual atomic disorder in the films or the presence of a perpendicular anisotropy caused by a small tetragonal distortion in the [001] direction.

In the following, the peak-to-peak linewidth ΔH as a function of frequency will be discussed in detail in oder to determine the damping of the films. Figure 5.7 shows the resulting peak-to-peak linewidth ΔH for all frequencies and all x. These measurements were performed in the direction of the magnetic hard axis of the Heusler films. The dependence of the linewidth versus frequency gives information about the magnetization dynamics of the samples. Thus, the experimental data were fitted by Equation 4.18 in order to determine the effective damping parameters. Due to the existence of inflection points in the curves, the slope at higher frequencies was used to determine the damping parameters. The according fit functions are also presented in Figure 5.7. The magnitude of the inhomogeneous residual linewidth at zero field ΔH_0 is presented in Figure 5.9b for all stoichiometries. The upper error margins result from the different slopes in the ΔH vs. f curves, while the lower value of the error margin is caused by the assumption that the linewidth measured at 40 GHz is caused

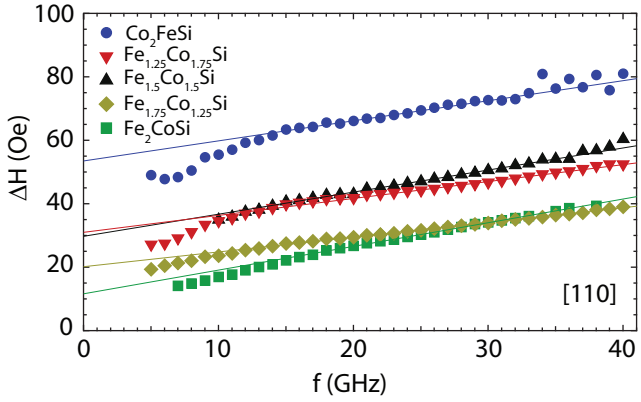

Figure 5.7 | Frequency dependent FMR linewidth for all samples measured along the magnetic hard axis [110] of the $Fe_{1+x}Co_{2-x}Si$ films along with the fit functions according to Equation 4.18.

solely by Gilbert type damping. The residual linewidth decreases as the Fe concentration increases and reaches its lowest value of ΔH_0 = 12 Oe for Fe_2CoSi. McMichael *et al.*[149] found that small grain size distributions can lead to low inhomogeneous line broadening.

The slope of the fits offers information about the effective Gilbert damping parameter α_{eff} of the samples. The results are presented in Figure 5.9c. Co_2FeSi exhibits a damping parameter of 0.0018. For the estimation of the upper limit of the error margins, it might be assumed that the damping parameter is solely caused by Gilbert type damping at 40 GHz. This leads to an error margin with an upper limit of 0.0034. The lower limit of the error margin is 0.0004 and is caused by different slopes of the curve. In the following, these asymmetric error margins are expressed as $0.0018\pm^{0.0034}_{0.0004}$. Fe_2CoSi shows a slightly larger value of $0.0019\pm^{0.0007}_{0.0001}$. The damping parameters determined in this work are similar in comparison with publications from other groups. For example, Kasatani *et al.* found damping parameters from 0.0023 to 0.0061 for Co_2FeSi films and 0.002 for Fe_2CoSi[150]. The lowest damping was again found for $Fe_{1.75}Co_{1.25}Si$ with $\alpha = 0.0012\pm^{0.0007}_{0.0001}$. In general, the Gilbert damping is expected to be low in half-metallic materials, where spin-flip processes are suppressed[151–154]. Hence, the small damping parameters of the metallic films show that a pseudo-gap as present in the $Fe_{1+x}Co_{2-x}Si$ system is sufficient to give rise to a low Gilbert damping.

Furthermore, the phase transition between the $L2_1$ and the X_a ordering will be discussed through these magnetic measurements. The performed magnetic

measurements do not give any indication that the phase transition between both structures occurs abruptly. The effective magnetization, presented in Figure 5.6, as well as the damping parameter, shown in Figure 5.9c, show no pronounced changes as a function of stoichiometry. A linear behavior for γ', ΔH_0, and K_4 is found for the stoichiometries between $Fe_{1.5}Co_{1.5}Si$ and Fe_2CoSi, respectively. Consequently, it seems that the structural transition takes place gradually at stoichiometries with a high amount of Fe ($x \geq 0.5$). This is different from the behavior close to Co_2FeSi, where γ' and ΔH_0 show more distinctive variations between two stoichiometries, while K_4 remains constant. This is also consistent with the ordering parameters presented in an earlier publication[14].

For a comparison between measurements along the magnetic hard and the magnetic easy axis, the frequency dependent linewidth along both axes is exemplarily presented for Fe_2CoSi in Figure 5.8. A non-linear behavior is observed in all linewidth vs. frequency response curves. In the case of Fe_2CoSi the nonlinearity is more pronounced in the measurements along the magnetic easy axis. This nonlinear dependence of the FMR linewidth on frequency is a typical observation when two magnon scattering contributes significantly to the relaxation[155,156]. Two-magnon scattering is an extrinsic relaxation mechanism and can be induced by means of different scattering centers such as voids or pores[157], surface roughness[155] and grain size[158] or by network of misfit dislocations[159], which causes scattering of the FMR mode (k=0) into propagating spin waves (k≠0).

As this section discussed the magnetization dynamics along one or two axes, the following section will present complete angle dependent data depending on the anisotropy distribution in the films.

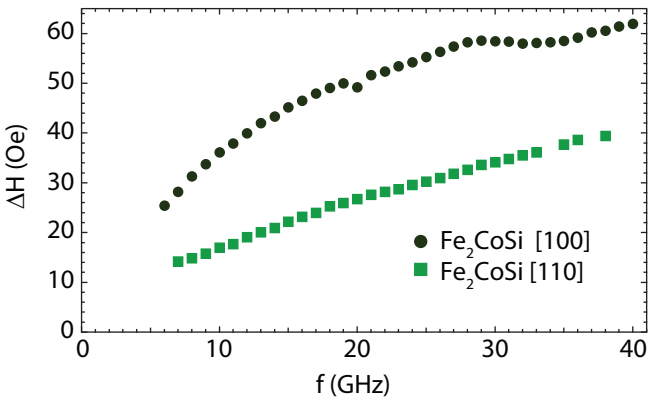

Figure 5.8 | FMR linewidth for Fe_2CoSi measured along both the magnetic hard [110] and easy [100] axis.

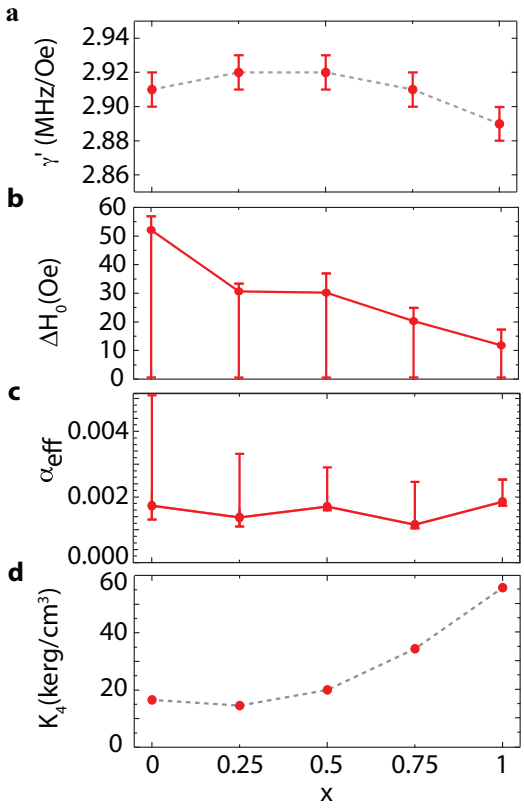

Figure 5.9 | a Gyromagnetic ratio γ', **b** Extrinsic contribution to the linewidth ΔH_0 of the FMR spectra, **c** effective Gilbert damping parameter and **d** cubic magnetic anisotropy constant K_4 for $Fe_{1+x}Co_{2-x}Si$ films with x=0, 0.25, 0.5, 0.75, 1.

5.4.1. In-Plane Anisotropy Distribution

This section will focus on the anisotropy distribution of the thin Co-Fe-Si films. Thus, FMR measurements were carried out as a function of the in-plane angle between the applied magnetic field and the $Fe_{1+x}Co_{2-x}Si$ [110] axis. The operating frequency for the rotation measurements was 30 GHz. At this frequency the resonance fields are high enough to saturate the magnetization along the easy and hard axes. All measurements were performed at room temperature.

The resulting ferromagnetic resonance field H_{res} versus the in-plane rotation angle is presented exemplarily for the Fe_2CoSi film in Figure 5.10a. A fourfold symmetry is observed for all samples. The dependence of the resonance field on

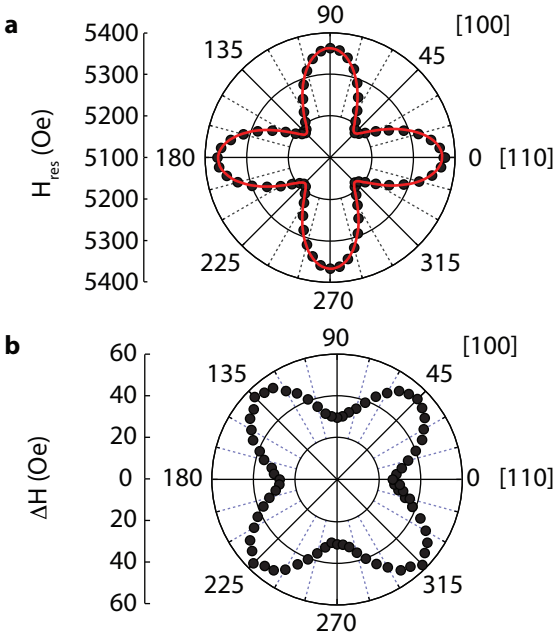

Figure 5.10 | Polar plots of **a** the resonance fields H_{res} (black markers) along with numerical solution using Equation 4.12 (red line) and **b** the linewidth ΔH as a function of the in-plane angle of the applied field with respect to the [110] axis of a 20 nm thick Fe_2CoSi film, measured at a microwave frequency of 30 GHz.

the in-plane angle was simulated numerically using Equation 4.12, assuming a cubic magnetic anisotropy contribution to the Gibbs free energy as introduced in Equation 2.5. The experimentally-determined in-plane angle dependent H_{res} data were fitted with the numerical solution (red line in Figure 5.10a) to determine the cubic anisotropy constant. The corresponding linewidth data is presented in Figure 5.10b, which also shows a clear fourfold symmetry. The linewidth exhibits maxima along the easy axes and minima along the hard axes of the cubic magnetic anisotropy. Randomly-distributed crystalline or surface roughness defects oriented along the in-plane principal crystallographic axis[160,161] or a fourfold distribution in misfit dislocations[159], which induce the same symmetry on the strength of two-magnon scattering, can explain the observed anisotropic relaxation.

The magnetic fourfold symmetry matches the crystallographic symmetry of the highly-textured $Fe_{1+x}Co_{2-x}Si$ films mentioned before. Moreover, in-plane rotational MOKE measurements were conducted. The resulting polar plot of

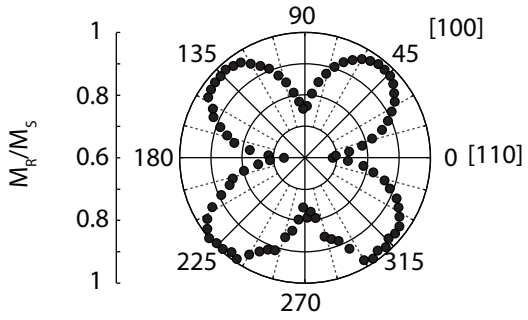

Figure 5.11 | Polar plots of the squareness M_R/M_S for Fe_2CoSi obtained by MOKE measurements.

the MOKE squareness versus the rotational angle of Fe_2CoSi is shown in Figure 5.11. This measurement confirms the cubic anisotropy present in the films as seen in the FMR measurement and matches the crystallographic symmetry of the textured films (Figure 5.3). The magnetic easy axis is located along the [100] crystallographic axis and the magnetic hard axis is located along the [110] crystallographic axis. A cubic anisotropy with the magnetic easy axis in the Heusler [100] direction is found for all samples. The cubic magnetic anisotropy constant K_4 obtained from the FMR measurements changes significantly in this series from 55.8 $\frac{\text{kerg}}{\text{cm}^3}$ for Fe_2CoSi to 16.6 $\frac{\text{kerg}}{\text{cm}^3}$ for Co_2FeSi, respectively. The cubic anisotropy constants for all stoichiometries are presented in Figure 5.9d. Hashimoto *et al.* found a similar cubic anisotropy constant of 18 $\frac{\text{kerg}}{\text{cm}^3}$ for crystalline Co_2FeSi with a film thickness of 18.5 nm[162]. For some samples in this series an additional uniaxial anisotropy was observed, which can originate from miscut substrates[163,164].

5.5. Conclusion

In summary, highly-epitaxial and single crystalline $Fe_{1+x}Co_{2-x}Si$ films were grown on MgO (100) substrates. Moreover, the films exhibit a high degree of atomic ordering. The integration the Co-Fe-Si films as an electrode into magnetic tunnel junctions resulted in high TMR ratios for all stoichiometries, which is an important factor for the application in spintronic devices. Large effect amplitudes allow for an accurate read-out signal in magnetic memories, e.g. MRAMs. Moreover, very small Gilbert damping parameters varying from $0.0012\pm^{0.0007}_{0.0001}$ to $0.0019\pm^{0.0007}_{0.0001}$ were found for all stoichiometries. Co_2FeSi

exhibits a damping parameter of $0.0018 \pm^{0.0034}_{0.0004}$. This makes these materials ideal candidates for the application in STT assisted magnetization switching in MRAMs, as low damping parameters result in low switching current densities.

The results of the magnetic measurements indicate that the phase transition from the $L2_1$ to the X_a structure takes place gradually at stoichiometries $x \geq 0.5$, while an opposite behavior is observed for $x \leq 0.25$.

This chapter presented a detailed investigation of the magnetic properties of the Co-Fe-Si films, which are suitable to be used as electrodes in spintronic devices. The following chapter will focus on different class of materials - antiferromagnets - for the improvement of the functionality of such devices. These materials can, for example, be used for the fabrication of a reference layer, which can also be used in MRAMs or in different memory technologies.

6 Exchange Bias in Bismuth and Lanthanum Ferrites

The last chapter presented a detailed investigations of the magnetization dynamics of $Fe_{1+x}Co_{2-x}Si$ Heusler compounds, which exhibit high TMR ratios and low Gilbert damping parameters. Thus, they are ideally-suited for the use in spintronic devices such as STT-MRAMs based on $Fe_{1+x}Co_{2-x}Si$ films, which would show high effect-amplitudes and low switching currents.

This chapter focuses on a different material class for the improvement of spintronic devices, i.e. antiferromagnetic multiferroics such as $BiFeO_3$ and $LaFeO_3$ thin films. Antiferromagnetic materials can be used to generate an exchange bias in a ferromagnetic layer, which can also be employed as a reference layer, e.g., in MRAMs. Moreover, as antiferromagnets are nearly unaffected by external magnetic fields, antiferromagnetic spintronics have gained much interest during the past years for future applications[8].

Multiferroic materials are materials that simultaneously exhibit a spontaneous electric and magnetic ordering[165]. A coupling between both properties can be used, for example, to switch the magnetization direction of an exchange coupled ferromagnetic layer with the help of an electric field. This effect was recently reported for $BiFeO_3$ films. High Néel temperatures for $BiFeO_3$ and $LaFeO_3$ crystals and high ferroelectric transition temperatures make these materials interesting for their application in devices.

This chapter demonstrates that $BiFeO_3$ crystals with high epitaxy can be prepared using reactive co-sputtering from elemental Bi and Fe targets. Furthermore, detailed investigations about the optimization of the growth process are given. Moreover, the chapter will show how antiferromagnetic ordering of the $BiFeO_3$ films is used to generate an exchange bias in ferromagnetic Co-Fe layers. Hence, the corresponding results will be discussed. The results presented in this section are published in Reference[16].

The second part deals with the deposition of $LaFeO_3$ films and the investigation of exchange biased ferromagnetic layers using the antiferromagnetic $LaFeO_3$ films. Finally, a GMR device containing a pinned electrode using a $LaFeO_3$ film is presented as proof of principle that these materials are good candidates for future devices.

6.1. Exchange Bias in $BiFeO_3$/Co-Fe Systems

The first part of this section focuses on the preparation of crystalline $BiFeO_3$ films and the determination of the optimal growth conditions. $BiFeO_3$ films were reported to be grown using different deposition methods, such as chemical solution deposition, pulsed laser deposition, or sputtering from elemental Bi-Fe-O targets. However, there are - to the best of my knowledge - no publications describing the preparation of $BiFeO_3$ films using reactive sputtering in a mixture of an oxygen/argon atmosphere from elemental Fe and Bi targets. Thus, this section will discuss the determination of the optimal growth conditions for the $BiFeO_3$ samples deposited using reactive co-sputtering form elemental Bi and Fe targets. Moreover, XAS and XLD measurements were performed to gain insights into the electronic and magnetic structure of the $BiFeO_3$ films, respectively.

The second part of this section presents detailed investigations of exchange biased ferromagnets using $BiFeO_3$ films.

6.1.1. Sample Preparation

This section describes how the thin $BiFeO_3$ films for this thesis were prepared. Crystalline substrates are suitable to allow a coherent and epitaxial growth of the films. According to the $BiFeO_3$ crystal structure, introduced in Section 3.2.1, an $SrTiO_3$ (100) substrate, a perovskite itself, is the ideal choice as the crystal structure of $SrTiO_3$ is cubic with a lattice parameter of 3.91 Å. The lattice parameter of $BiFeO_3$ crystals in the pseudocubic representation of the unit cell, which is used in this section, is 3.965Å. The resulting lattice mismatch between both parameters is less than 0.7 %, which promotes an epitaxial growth of the $BiFeO_3$ films.

The films were deposited on heated $SrTiO_3$ substrates using co-sputtering from elemental Bi and Fe targets in an atmosphere of a mixture of argon and oxygen. The resulting sputtering pressure was in the order of magnitude of 10^{-3} mbar. In order to determine the correct sputtering powers for Bi and Fe

(and the ferromagnetic Co-Fe layers), X-ray fluorescence spectroscopy was used. Unfortunately, the utilized setup could not be used to determine the amount of oxygen in the samples, as it is very challenging to detect light elements like oxygen. In order to obtain information about the amount of oxygen in the films, a series of samples was grown at different oxygen partial pressures, which were investigated using XRD techniques. The oxygen partial pressure, at which the samples show the highest crystallinity was kept constant for the growth of further samples. Afterwards, XRD was also used to investigate the influence of the deposition temperature on the crystallography of the $BiFeO_3$ films in order to determine the optimal growth conditions.

Keeping these optimized parameters fixed, ferromagnetic Co-Fe layers were deposited on top of the $BiFeO_3$ films to investigate the exchange bias properties of this multilayer structure. To achieve a pinning between the antiferromagnet and the ferromagnet, the Co-Fe layers were deposited at a substrate temperature of 175°C followed by a field-cooling in a magnetic field of 150 Oe in the [100] direction of the $BiFeO_3$. This temperature was found to be high enough to pin the Co-Fe layer. Higher deposition temperatures for the Co-Fe layer led to excessive interdiffusion.

Finally, all samples were capped with an insulating 2 nm thick MgO layer to protect the specimen from degradation without effecting the electric properties of the sample. Figure 6.1 shows a sketch of the grown multilayer systems, used for the investigations of the exchange bias effect.

The following section will present the results of XRD investigations on the samples, which were recorded to determine the best growth conditions for single-crystalline $BiFeO_3$ films.

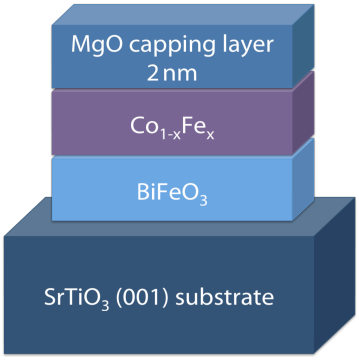

Figure 6.1 | Sketch of the grown $BiFeO_3$/Co-Fe multilayers.

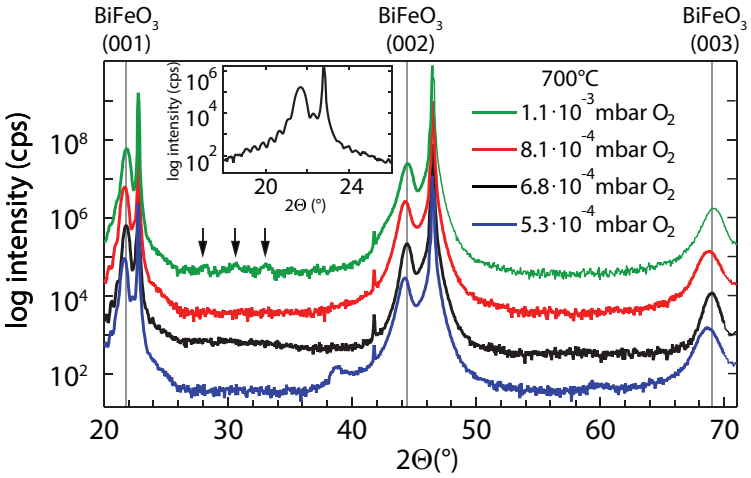

Figure 6.2 | XRD patterns for $BiFeO_3$ films grown at a substrate temperature of 700°C with various oxygen partial pressures. The pattern of the film grown at a high oxygen partial pressure shows several features, marked by the arrows, indicating the presence more phases. The inset shows a magnification of the $BiFeO_3$ (001) peak with pronounced Laue-oscillations at an oxygen partial pressure of $6.8{\cdot}10^{-4}$ mbar.

6.1.2. Crystallographic Properties

In order to determine the optimal growth conditions during sputtering, the substrate was heated to 700°C and the oxygen partial pressure was varied from $5.3{\cdot}10^{-4}$ mbar to $1.1{\cdot}10^{-3}$ mbar, while the Ar partial pressure remained constant at $1.5 \cdot 10^{-3}$ mbar for all samples. The corresponding XRD patterns are presented in Figure 6.2. Films deposited with a small oxygen partial pressure of $5.3{\cdot}10^{-4}$ mbar show a reflection around $2\Theta = 39°$, which may be caused by a small amount of a Fe-O phase inside the films. At oxygen partial pressures of $8.1 \cdot 10^{-4}$ mbar no secondary phases are visible in the XRD patterns. The film grown at a high oxygen partial pressure of $1.1 \cdot 10^{-3}$ mbar seems to be over-oxidized and the XRD pattern shows additional features (marked by arrows). The $BiFeO_3$ film grown at $6.8 \cdot 10^{-4}$ mbar O_2 exhibits the sharpest peaks and pronounced Laue-oscillations indicating a high crystallinity, as shown in the inset in Figure 6.2, with an out-of-plane lattice parameter of 4.08 Å. Supposing an epitaxial matching of the in-plane $BiFeO_3$ lattice parameter to the $SrTiO_3$ substrate and assuming the volume of the $BiFeO_3$ unit cell remains constant upon strain, the expected lattice parameter is $c = 4.05$ Å, which is very close to the measured one. Thus, the oxygen partial pressure of $6.8 \cdot 10^{-4}$ mbar was kept constant.

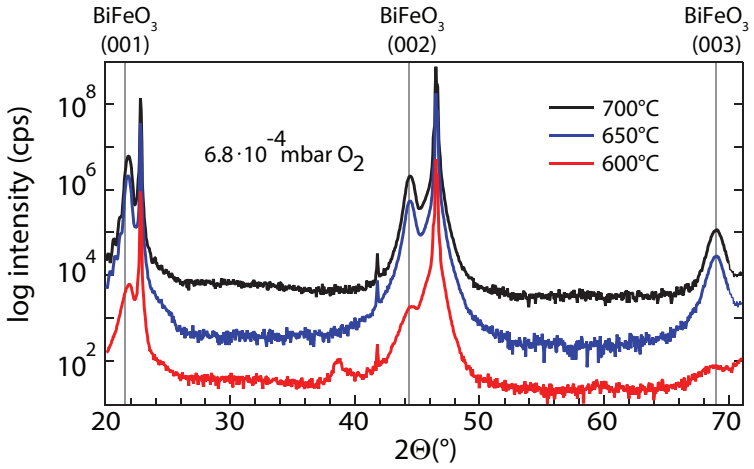

Figure 6.3 | XRD patterns for $BiFeO_3$ films grown at different substrate temperatures and an O_2 partial pressure of $6.8 \cdot 10^{-4}$ mbar.

For a further determination of the optimal growth conditions the substrate temperature was varied. The resulting XRD patterns are presented in Figure 6.3. The crystallization of $BiFeO_3$ starts at 600°C, resulting in small $BiFeO_3$ peaks. Again, the reflection caused by the secondary phase can be found at $2\Theta = 39°$. At higher deposition temperatures the lattice parameter decreases, as the peak positions shift to higher angles, and approaches the expected values. At a deposition temperature of 750°C the $BiFeO_3$ film starts to evaporate as is indicated by greatly reduced film thickness, obtained from XRR measurements, for otherwise unchanged deposition conditions.

Consequently, an O_2 partial pressure of $6.8 \cdot 10^{-4}$ mbar and a deposition temperature of 700°C are chosen as ideal growth parameters for epitaxial $BiFeO_3$ films for further experiments presented in the following sections.

The next section will discuss the electronic structure of the $BiFeO_3$ crystal.

6.1.3. X-Ray Absorption Spectroscopy

The $BiFeO_3$ film that shows the highest crystallinity was used to determine element-specific electronic and magnetic properties using X-ray absorption techniques. The measurements were done at room temperature in surface-sensitive total electron yield[166], with a magnetic field of 0.5 T, which was applied parallel to the plane of incidence of the beam. The linear (circular) polarization degree was 100% (90%) and the X-ray angle of incidence to the sample surface was

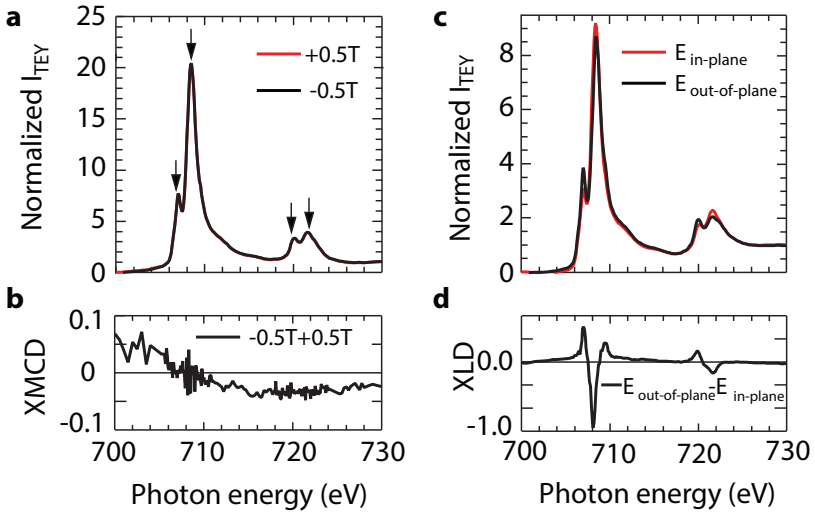

Figure 6.4 | a XAS measurements with both circular polarization with **b** corresponding XMCD and **c** XAS measurements with electric field component in- and out-of-plane with respect to the film and **d** XLD difference.

30° for all measurements. As discussed in Section 3.2.1, the Fe atoms are responsible for the magnetism as they couple antiferromagnetically. Accordingly, scans around the Fe $L_{2,3}$ absorption edge were conducted at beamline 4.0.2 of the Advanced Light Source in Berkeley, CA, USA. Figure 6.4a presents normalized XAS scans at the Fe $L_{2,3}$ absorption edge of the $BiFeO_3$ film. The two-peak structure is clearly visible at both the L_2- and L_3- edge, as expected for a trivalent Fe state (marked by the arrows)[167]. However, no difference was found between XAS with magnetization parallel or antiparallel to the beam. The XMCD is virtually zero as depicted in Figure 6.4c. Thus, the investigated $BiFeO_3$ film shows no ferromagnetic order and contains no parasitic phases such as ferrimagnetic γ-Fe_2O_3, which is not easily detectable in thin films using XRD measurements[167,168]. In order to test the films for antiferromagnetism two XAS scans with the beam polarization vector parallel or perpendicular to the film plane were performed. The results are presented in Figure 6.4b, where a clear difference between both orientations is visible as shown in Figure 6.4d. The observed XLD can be of structural or magnetic origin and these two possibilities cannot be distinguished from our measurements. However, our XLD spectra resemble very closely in shape and signal those measured by Béa *et al.*[169]. The antiferromagnetic order in their $BiFeO_3$ films was confirmed by neutron diffraction experiments. Another evidence for the antiferromagnetic

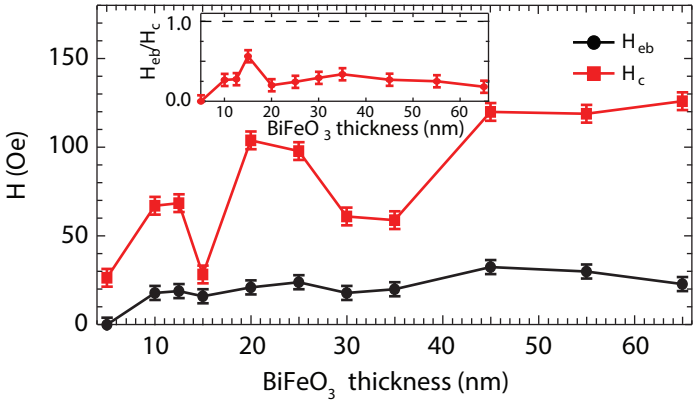

Figure 6.5 | Exchange bias as a function of $BiFeO_3$ film thickness with a 3 nm $Co_{60}Fe_{40}$ layer. The H_{eb}/H_c ratio is presented in the inset.

ordering of the films is given by an induced exchange bias in the $BiFeO_3$/Co-Fe multilayers, which will be discussed in the following section.

6.1.4. Magnetic Properties

In this section the magnitude of the exchange bias effect in the $BiFeO_3$/Co-Fe layers as a function of both layer thicknesses, i.e., the layer thickness of the $BiFeO_3$ as well as the Co-Fe thickness, is presented. At first, the influence of the $BiFeO_3$ layer thickness on the exchange bias is investigated. For this series, a 3 nm thick $Co_{60}Fe_{40}$ film is used as ferromagnetic layer. The magnetic properties of the Co-Fe layer - the shift of the hysteresis H_{eb} - and the coercive field H_c are determined by room-temperature MOKE measurements. The resulting properties are presented in Figure 6.5. The error margins are based on small variations of the magnetic field values. A positive exchange bias is observed for all samples where the hysteresis is shifted toward the negative field cooling direction. Both fields generally increase with increasing film thickness. A maximum exchange bias field H_{eb} = 33 Oe was found for 45 nm thick $BiFeO_3$ layer. The apparently non-systematic behavior of the coercive field may be related to problems with the heat transfer between the substrate and the holder, which in some cases led to not-precisely determinable lower substrate temperatures. Nevertheless, a thickness as low as 12.5 nm $BiFeO_3$ generates an exchange bias of H_{eb} = 19 Oe and a coercive field of H_c = 69 Oe. In general, small film thicknesses are interesting for commercial application as the short deposition time shortens the fabrication process and leads to lower-cost products. This

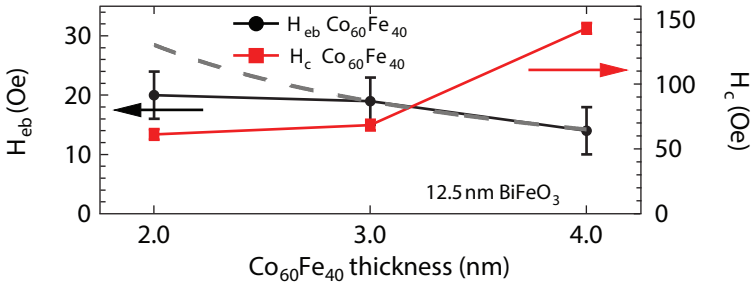

Figure 6.6 | Echange bias for a 12.5 nm $BiFeO_3$ film with different $Co_{60}Fe_{40}$ film thicknesses.

thickness is used to study the influence of different Co-Fe film thicknesses and Co-Fe stoichiometries. In the following, the dependence of the thickness of the ferromagnet on the amplitude of the exchange bias is investigated.

Figure 6.6 shows the resulting H_{eb} and H_c as a function of $Co_{60}Fe_{40}$ thickness. A maximum exchange bias is found for a 2 nm thick $Co_{60}Fe_{40}$ film with H_{eb} = 20 Oe and H_c = 61 Oe, while the coercivity increases with an increasing ferromagnet thickness up to H_c = 143 Oe at a thickness of 4 nm $Co_{60}Fe_{40}$. As introduced in Equation 2.11 the exchange bias is usually given by the proportionality $H_{eb} \propto 1/t_{FM}$, as indicated by the dashed line in Figure 6.6. This dependence cannot be found in the investigated samples. A similar behavior was found in MnN/CoFe bilayers[170]. Moreover, $Co_{60}Fe_{40}$ films thinner than 2 nm show no hysteresis with vanishing coercivity and no shift of the magnetization curve. This is probably responsible for the flattening of the H_{eb} curve

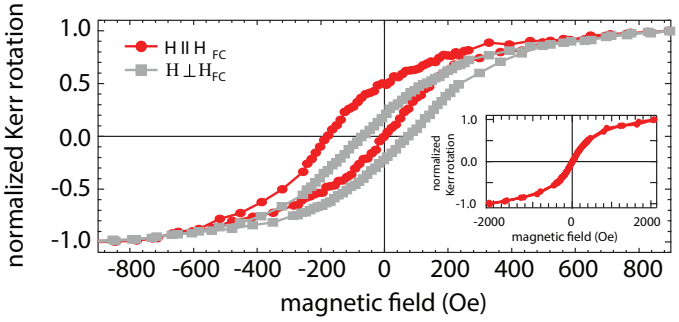

Figure 6.7 | Hysteresis for a 12.5 nm $BiFeO_3$/2 nm Co film for parallel and perpendicular alignment with respect to the field-cooling direction H_{FC}. The inset shows a MOKE measurement for a 12.5 nm $BiFeO_3$/1.5 nm Co bilayer.

Table 6.1 | Maximum exchange bias fields and coercive fields H_{eb} and H_c for various stoichiometries of a 2 nm thick ferromagnet on a 12.5 nm $BiFeO_3$ film, determined from MOKE measurements.

Composition	H_{eb} (Oe)	H_c (Oe)
Fe	-	-
$Co_{60}Fe_{40}$	20	61
$Co_{90}Fe_{10}$	36	27
Co	92	89

around 2 nm. The inset in Figure 6.7 shows a MOKE measurement of a 12.5 nm $BiFeO_3$/1.5 nm Co bilayer.

For the application of exchange biased ferromagnetic films in spintronic devices the ratio H_{eb}/H_c should be larger than unity. If this condition is given it is possible to easily obtain distinctive magnetization directions. As presented in the inset in Figure 6.5 this is not fulfilled in the $BiFeO_3/Co_{60}Fe_{40}$ bilayers. In order to increase the amplitude of the exchange bias, the stoichiometry of the Co-Fe layer was shifted to a higher amount of Co, while a $BiFeO_3$ film thickness of 12.5 nm was kept constant. The resulting exchange bias and coercive fields observed for different compositions of the ferromagnetic layer are summarized in Table 6.1. Hence, the exchange bias can be increased by using ferromagnetic layers with a higher amount of Co and reaches its maximum for a pure Co film with H_{eb} = 92 Oe and H_c = 89 Oe, while for pure Fe films no ferromagnetic hysteresis can be observed, likely due to oxidation of the Fe film. Figure 6.7 exemplarily shows the MOKE measurements for such a 12.5 nm $BiFeO_3$/2 nm Co film, for which no training effect was observed after 100 loops.

In this case the ratio H_{eb}/H_c is larger than unity, which makes this bilayer stack interesting for spintronic devices. Moreover, large exchange energies are desirable. According to Equation 2.11 the exchange energy can be calculated within the Meiklejohn-Bean model to $J_{eff} = t_{FM} M_{FM} H_{eb} \approx 0.02 \frac{erg}{cm^2}$. Along with a critical $BiFeO_3$ film thickness of $t_{crit} \approx 10$ nm, the effective unidirectional anisotropy constant is $K_{eff} = J_{eff}/t_{crit} \approx 2 \cdot 10^4 \frac{erg}{cm^3}$. These values are much smaller than, for example, for Mn_3Ir with $J_{eff} > 1 \frac{erg}{cm^2}$ and $K_{eff} = 2 \cdot 10^6 \frac{erg}{cm^3}$ [171], that is widely used as an antiferromagnet, but too expensive for commercial applications.

A comparison of the exchange bias amplitudes measured in this work with the results published by other groups show, that the effect amplitudes for crystalline films are similar. Béa *et al.*[169] found slightly smaller exchange bias fields for

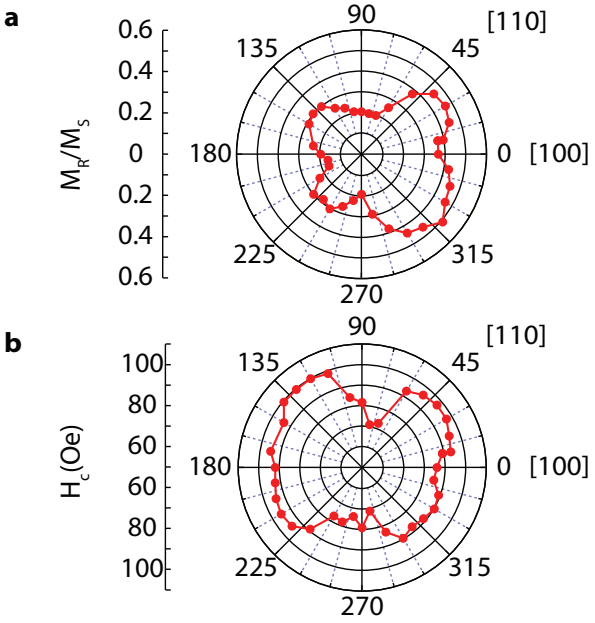

Figure 6.8 | MOKE **a** squareness M_R/M_S and **b** coercive field H_c for 12.5 nm $BiFeO_3$/2 nm Co layer system as a function of the in-plane rotational angle. The magnetic field during field-cooling was applied along the [100] direction.

single crystalline 35 nm $BiFeO_3$ films with 5 nm $Co_{72}Fe_8B_{20}$ of H_c = 42 Oe and H_{eb} = 62 Oe. Measurements of a 200 nm $BiFeO_3$/5 nm $Ni_{81}Fe_{19}$ bilayer by Dho *et al.*[172] revealed an exchange bias in the same order of magnitude of H_{eb} = 80 Oe but with a lower coercivity of H_c = 22 Oe. However, polycrystalline $BiFeO_3$ films are reported to generate a much larger exchange bias effect than single crystalline films. Chang *et al.*[173] found exchange bias fields of up to H_{eb} = 400 Oe coercive fields of H_c = 1.2 – 3.6 kOe.

This section presented the maximum exchange bias values that were obtained by measurements of the hysteresis loops along the field-cooling direction. The following section presents research of the in-plane magnetic properties in different directions.

In-Plane Anisotropy Distribution

For an additional confirmation of the presence of the exchange bias effect in $BiFeO_3$/Co stacks, in-plane MOKE rotation measurements were performed.

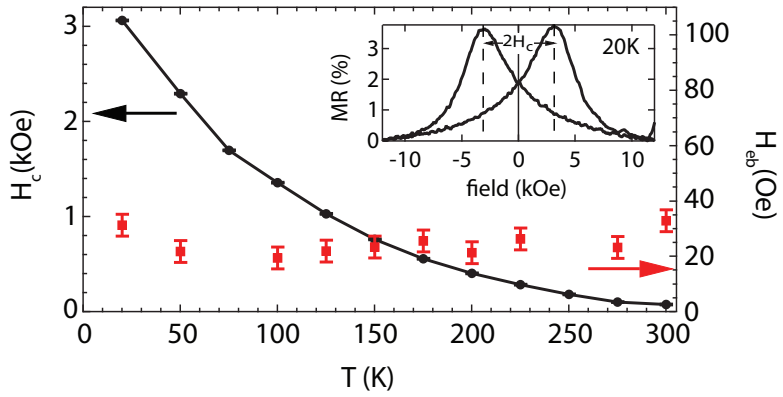

Figure 6.9 | Coercive field H_c and exchange bias field H_{eb} versus measurement temperature for a 12.5 nm $BiFeO_3$/2 nm Co bilayer obtained by AMR measurements. The inset shows AMR measurement at 20 K. The MR is normalized by $MR=(R(H)-R_{min})/R_{min}\cdot 100\%$.

Therefore, several hysteresis loops were recorded in steps of 10°. The resulting averaged squareness M_R/M_S, along with the coercive field H_c versus rotational angle are presented in Figure 6.8a and b, where the field-cooling direction is in [100] direction of the $BiFeO_3$/Co films, which is defined as 0°. The squareness shows a pronounced unidirectional anisotropy with a superimposed fourfold anisotropy. This indicates that the $BiFeO_3$ film induces a body centered tetragonal structure (bct) in the Co films[174]. The corresponding coercive field versus rotational angle measurements (see Figure 6.8b) show the butterfly-like shape typical for an exchange bias system with a weak superimposed fourfold anisotropy. As expected, the coercive field is small for angles perpendicular to the field-cooling direction: in the [010] and [0$\bar{1}$0] directions. These graphs visualize the presence of an exchange bias effect in the ferromagnetic layer, as all expected features are present.

So far, the exchange bias effect has only been studied at room temperature. Thus, the following section concentrates on the temperature-dependence of the effect size.

Temperature-Dependence Of The Exchange Bias

In order to obtain information about the pinning of the ferromagnetic Co layer (in a 12.5 nm $BiFeO_3$/2 nm Co stack), measurements of the AMR effect were conducted at a Hall-bar geometry with a width of 183 μm and a length of 622 μm. Because the $BiFeO_3$ layer and the $SrTiO_3$ substrate are insulating,

the resistivity is directly provided by the Co layer and depends on the magnetic properties of the film, as introduced in Section 2.4.1. During measurement, the field-cooling direction was aligned parallel to the applied magnetic field and the probe current. The inset in Figure 6.9 shows the AMR curve measured at 20 K. The peak positions were determined by an interpolation of the data points of the maxima and to determine the coercive field H_c, as well as the exchange bias field H_{eb}. Accordingly, the results are presented in Figure 6.9. The coercivity increases from H_c = 78 Oe at 300 K to H_c = 3.1 kOe at 20 K. This behavior is very similar to the temperature-dependence measured in NiFe/PtPdMn and NiFe/NiMn systems by Hou *et al.*[175]. The shift of the AMR curves determines the exchange bias to approximately H_{eb} = 20 Oe, which remains constant for all temperatures. The rotation of the sample by 180° degrees results in a corresponding shift to negative values and H_{eb} = −20 Oe.

6.1.5. Summary and Conclusion

In summary, highly epitaxial $BiFeO_3$ films were grown using reactive magnetron co-sputtering from elemental Bi and Fe targets. As presented above, the crystallization of $BiFeO_3$ crystals needs a high deposition temperature. A significant crystallization was found for temperatures around 600°C. The preparation of the $BiFeO_3$ films was very challenging, as the evaporation temperatures of Bi atoms is around 330°C at a pressure of 10^{-7} mbar and 520°C at 10^{-3} mbar[176]. Consequently, the Bi atoms start to evaporate off the $SrTiO_3$ substrates at temperatures for which the crystallization of the $BiFeO_3$ takes place. Thus, the sputtering rate has to be high enough to compensate this process. Moreover, the variation of the oxygen partial pressure, as well as the deposition temperature, revealed that both parameters have to be chosen correctly for the growth of single-crystalline films. Films grown at the optimal deposition conditions show well-pronounced Laue-oscillations in the XRD patterns, confirming the high epitaxial order of the $BiFeO_3$ films. Moreover, XAS measurements confirmed that the Fe atoms are in a trivalent oxidation state, as expected for $BiFeO_3$ crystals.

The magnetic ordering of the $BiFeO_3$ films is antiferromagnetic, as seen by XLD measurements along with the large exchange bias induced in all ferromagnetic Co-Fe layers. Moreover, the unidirectional anisotropy could be nicely illustrated with in-plane rotational MOKE measurements. As presented above, the non-systematic $BiFeO_3$ thickness dependence of both the exchange bias field and the coercivity points to variations between the grown samples as the measured dependence should be smoother. The most probable origin of this

unexpected dependence is the heat transfer between the $SrTiO_3$ substrate and the sample carrier. This would, consequently, lead to a temperature variation over the sample and thus to regions with different crystallographic ordering. For the application of $BiFeO_3$ films in devices, another challenging task is inducing a pinning in the ferromagnetic layer. For this thesis this was realized by the deposition of the ferromagnet at 175°C in a magnetic field with subsequent (field-)cooling, as this was much more effective than an *ex situ* field-cooling, as strong interdiffusion or oxidation of the ferromagnet reduces the exchange bias amplitude. This sensitivity to the temperature made further investigations, such as reverse field-cooling experiments, nearly impossible. This has to be improved before a commercial application could be reasonable. Nevertheless, a pinning was found down to film thicknesses of the $BiFeO_3$ of 12.5 nm and by using pure 2 nm Co layers the exchange bias could be tuned to H_{eb} = 92 Oe along with a coercivity of H_c = 89 Oe. As the exchange bias field is larger than the coercivity, this layer stack is - in principle - interesting for the application of $BiFeO_3$ films in devices.

6.2. Exchange Bias in $LaFeO_3$/Co-Fe Bilayers

While the last section dealt with the preparation of $BiFeO_3$ thin films and their ability to generate an exchange bias, this section will focus on $LaFeO_3$. The $LaFeO_3$ films are also grown using reactive co-sputtering from elemental La and Fe targets. In analogy to the last section, ferromagnetic Co-Fe films were deposited on top of the $LaFeO_3$ films and exchange biased using the antiferromagnetic $LaFeO_3$ films. This section will present detailed investigations of the pinned ferromagnetic films and is organized as follows. The first part will focus on the preparational details in order to determine the optimal growth conditions. The second part presents detailed investigations of the exchange bias effect in $LaFeO_3$/Co multilayers using the magneto-optic Kerr effect along with a discussion of the influence of the annealing temperature and the blocking temperature. Moreover, the temperature-dependence of the magnetic properties is determined using measurements of the AMR effect will be presented. Finally, the applicability of $LaFeO_3$ films in spintronic devices is demonstrated.

6.2.1. Sample Preparation

This section deals with the preparation details of thin $LaFeO_3$ films. As discussed in Section 3.2.2 the properties of $LaFeO_3$ and $BiFeO_3$ are very similar, including the lattice parameter, as the ionic radii for Bi and La are nearly the same. Because the crystal structure of the ferroelectric phase of $LaFeO_3$ is the same as the paraelectric phase of the $BiFeO_3$, it can as well be described as pseudocubic, rhombohedral, or hexagonal. In this section the pseudocubic representation of the unit cell is used, in which the lattice parameter of $LaFeO_3$ is

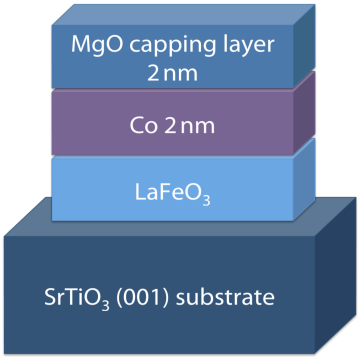

Figure 6.10 | Sketch of the grown $LaFeO_3$/Co multilayers.

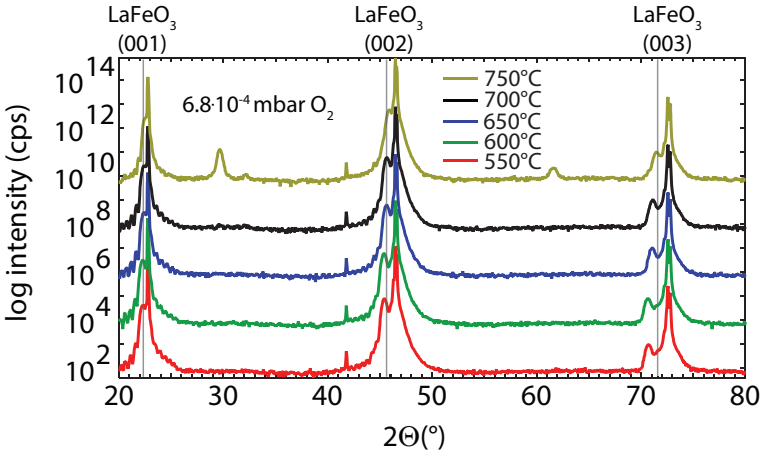

Figure 6.11 | XRD pattern of $LaFeO_3$ films grown at different substrate temperatures for an oxygen partial pressure of $6.8 \cdot 10^{-4}$ and an argon pressure of $1.5 \cdot 10^{-3}$.

3.93 Å[124]. Thus, cubic $SrTiO_3$ (100) substrates, which have a lattice parameter of 3.91 Å, are an ideal choice for an epitaxial growth of the $LaFeO_3$ films. For the investigations of the exchange bias effect, bilayers consisting of $LaFeO_3$ and Co-Fe layers were prepared, in which the Co-Fe was deposited *in situ* and, afterwards, annealed *ex situ* in a magnetic field. A sketch of the investigated films systems in shown in Figure 6.10. The following section describes the influence of the deposition conditions on the crystallinity of the $LaFeO_3$ films.

6.2.2. Crystallographic Properties

Similar to the deposition of the $BiFeO_3$ films, X-ray fluorescence spectroscopy was used in order to determine the correct sputtering powers for La and Fe. For the determination of the optimal growth parameters for epitaxial $LaFeO_3$ films both the deposition temperature and the oxygen partial pressure were varied. At first, the substrate temperature was varied while the oxygen partial pressure was held constant at $6.8 \cdot 10^{-4}$ mbar and the argon partial pressure at $1.5 \cdot 10^{-3}$ mbar. Figure 6.11 shows the resulting XRD patterns of the $LaFeO_3$ films with a thickness of approximately 20 nm grown at different substrate temperatures. Pronounced $LaFeO_3$ (00*l*) with *l*=1, 2, 3,.. peaks are located at the lower angle region of the $SrTiO_3$ (00*l*) substrate peaks, respectively, and can be found for all deposition temperatures between 550°C and 750°C. The XRD patterns of samples that were grown at deposition temperatures lower than or equal to 700°C

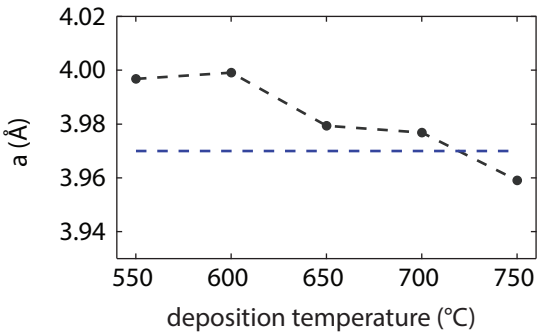

Figure 6.12 | $LaFeO_3$ lattice parameter in c direction for films grown at different substrate temperatures for a fixed oxygen partial pressure of $6.8{\cdot}10^{-4}$ and an argon partial pressure of $1.5{\cdot}10^{-3}$. The expected lattice parameter is given by the dashed line.

exhibit no additional reflections, while for a substrate temperature of 750°C additional peaks at $2\Theta = 26.6°$, $2\Theta = 32.3°$, and $2\Theta = 61.6°$ are found. This is an indication that at this temperature the film decomposes into phases of $LaFeO_3$ and some Fe-O compositions. Additionally, at this temperature the intensity of the Laue oscillations at the $LaFeO_3$ (001) peak are less pronounced and for or the (002) peak they disappear completely. In contrast, Laue oscillations at the (001) and (002) peak of $LaFeO_3$ are clearly visible for films grown between 550°C and 750°C. In comparison to the $BiFeO_3$ growth, the temperature has less influence on the crystallinity. In the following the variation of the lattice parameter is discussed in order to gain insights into the crystallinity. Assuming an epitaxial matching of the $LaFeO_3$ lattice parameter to the in-plane lattice of the $SrTiO_3$ along with a constant volume of the unit cell upon stain, this leads to an out-of-plane lattice parameter of 3.97Å. The lattice parameter of the films is calculated using the (003) peak positions. The resulting lattice parameter in the out-of-plane direction as a function of deposition temperature is given in Figure 6.12. The lattice parameter in c direction is 4.0Å for the film grown at a substrate temperature of 550°C and decreases with increasing temperature. At 750°C it is 3.96Å, which is even smaller than the theoretically-expected value, illustrated by the dashed line. Thus, a deposition temperature of 750°C is too high for the growth of the $LaFeO_3$ films. Consequently, a substrate temperature of 700°C is kept fixed for the deposition of $LaFeO_3$ films for magnetic measurements.

For further optimization of the crystallinity of the $LaFeO_3$ films, the oxygen partial pressure was varied at the previously determined optimum substrate temperature of 700°C. The Ar partial pressure during sputtering was $1.5{\cdot}10^{-3}$ mbar

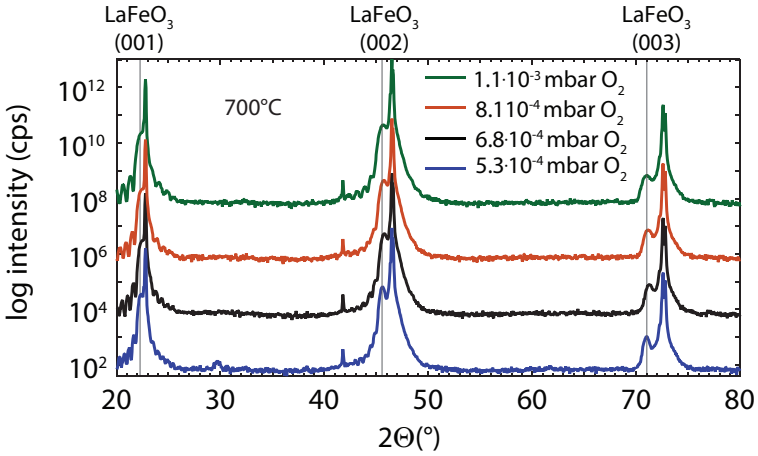

Figure 6.13 | XRD pattern of $LaFeO_3$ films grown with different oxygen partial pressures at a substrate temperature of 700°C. The Ar partial pressure remains constant at $1.5 \cdot 10^{-3}$.

in all cases. Figure 6.13 displays the resulting XRD patterns, in which all films show intense $LaFeO_3$ (00*l*) reflections. The XRD patterns of the films grown at a low oxygen partial pressure of $5.3 \cdot 10^{-4}$ mbar O_2 show an additional reflection at $2\Theta = 29.6°$, which can be assigned to Fe-O compounds. No secondary phases are observed for films grown between $6.8 \cdot 10^{-4}$ mbar and $1.1 \cdot 10^{-3}$ mbar. A high epitaxial ordering is found for all samples in this series, as Laue oscillations are present for all samples at both the $LaFeO_3$ (001) and (002) peaks. The film thickness decreases with increasing oxygen partial pressure, which was confirmed using X-ray reflectivity measurements. This can also be seen in the frequency change of the Laue oscillations, as the crystalline volume is decreased, as well as the peak broadening for thinner films. In order to determine the optimal oxygen partial pressure during growth, the influence on the lattice parameter is investigated and presented in Figure 6.14. As can be seen the variation of the lattice parameter with the different oxygen partial pressures is small. The lattice parameter that matches the expected parameter of 3.97Å is found for films grown at an oxygen partial pressure of $6.8 \cdot 10^{-4}$ mbar. The lattice parameter increases with both lower and higher oxygen partial pressures to slightly larger lattice parameters. Consequently, the influence of the oxygen partial pressure has a smaller effect on the crystallographic quality of the films than the deposition temperature. An oxygen partial pressure of $6.8 \cdot 10^{-4}$ mbar O_2 along with an argon partial pressure of $1.5 \cdot 10^{-3}$ mbar and a substrate temperature of 700°C

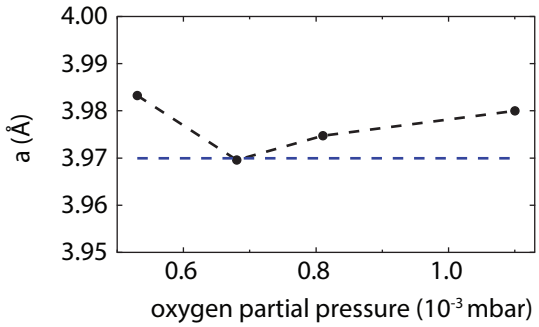

Figure 6.14 | $LaFeO_3$ out-of-plane lattice parameter for films grown at a substrate temperatures of 700°C at different oxygen partial pressures and an argon partial pressure of $1.5 \cdot 10^{-3}$. The dashed line represents the expected lattice parameter.

was chosen for the growth of further $LaFeO_3$ films. These optimized films are used for more detailed investigations.

Measurements of the off-specular $LaFeO_3$ (224) peak revealed that the pseudocubic unit cell perfectly aligns with the cubic $SrTiO_3$ unit cell and show a fourfold symmetry, indicating an epitaxial growth.

Another indication for high epitaxy in the films is given by the presence of Laue oscillations. Figure 6.15 presents an XRD scan at small angles measured with a fixed divergence of the beam (1/32°). The first part of the scan is a representation of the X-ray reflectivity data containing the Kiessig fringes, while the higher angle part shows the Laue oscillations around the $LaFeO_3$ (001) peak in the left shoulder of the $SrTiO_3$ (001) peak. The intensity is presented as a function of the scattering vector $q = 4\frac{\pi}{\lambda}\sin(\theta)$ with $\lambda = 1.5419$Å in order to allow a comparison of the oscillation frequency of the Kiessig fringes and the Laue oscillations. Although, the oscillations are of totally different origins it is possible to make a quantification of the degree of epitaxy. The frequency of the Kiessig fringes only depends on the thickness of the investigated material and is completely independent from the structure of the material. Whereas Laue oscillations depend on the number of scattering planes in the film. The frequency of the Kiessig fringes Δd_{XRR} gives a total $LaFeO_3$ film thickness of 17.5 nm, while the frequency of the Laue oscillations Δd_{Laue} at the (001) peaks indicate that about 90% of the film thickness show highly epitaxial growth leading to Laue oscillations. The deviation from the nominal film thickness of 17.5 nm can be related to surface roughness or to distortions at the interface between $LaFeO_3$ and $SrTiO_3$.

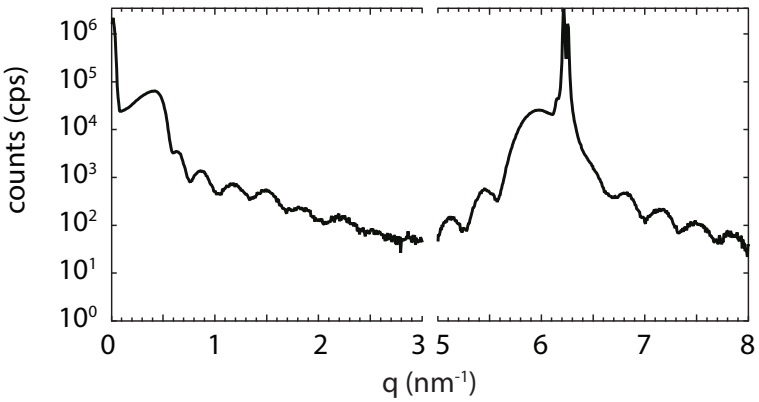

Figure 6.15 | XRD patterns at low angles for a $LaFeO_3$ film deposited at optimal growth conditions, i.e. 700°C, $6.8 \cdot 10^{-4}$ O_2 along with an argon partial pressure of $1.5 \cdot 10^{-3}$ Ar.

After the optimal growth conditions were determined for the growth of highly epitaxial films, the next section focusses on bilayers containing $LaFeO_3$/Co layers for the investigation of the exchange bias effect.

6.2.3. Magnetic Properties

In order to investigate the magnetic structure of the $LaFeO_3$ films and to test them for antiferromagnetism, ferromagnetic Co films were deposited *in situ* on top of the $LaFeO_3$ films. The bilayers were capped with a 2 nm thick MgO. Afterwards, the samples were annealed *ex situ* in a vacuum furnace for 15 min at 300°C in a magnetic field of 6.5 kOe to achieve a pinning of the ferromagnetic Co layer. The bilayers were investigated using the magneto-optic Kerr effect to determine the magnetic parameters, i.e., the loop shift H_{eb} and the coercivity H_c of the Co layer. First, the influence of the $LaFeO_3$ film thickness on the exchange is investigated. The results of the exchange bias field H_{eb} along with the coercive field H_c as a function of the $LaFeO_3$ film thickness with 2 nm Co films on top are presented in Figure 6.16. The coercivity is large for all film thicknesses and shows a dip at a $LaFeO_3$ film thickness of 30 nm. This dependence is unusual for exchange biased systems, as the coercivity is generally small at low antiferromagnet film thicknesses followed by a strongly decreasing and finally saturating curve, as shown in Figure 2.7. The shift of the hysteresis, denoted by H_{eb}, can already be observed at a $LaFeO_3$ thickness of 10 nm with an exchange bias field of 24 Oe. With increasing $LaFeO_3$ thickness, H_{eb}

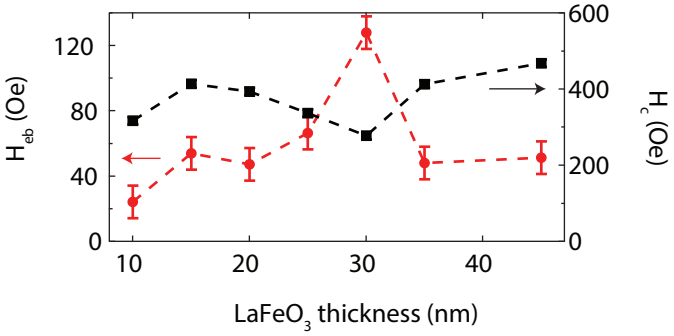

Figure 6.16 | H_{eb} and H_c as a function of the $LaFeO_3$ film thickness with a 2 nm thick Co film.

increases as well. The exchange bias field reaches a maximum value of 128 Oe for a $LaFeO_3$ thickness of 30 nm along with a coercive field of H_c=300 Oe. A corresponding hysteresis loop of this sample is presented in Figure 6.17. For thicker films the exchange bias fields drop significantly to similar values compared to those before the bump and remain constant for 35 nm and 45 nm thick $LaFeO_3$ films. This dependence is surprising, as this is an unexpected behavior for a H_{eb} versus antiferromagnet thickness-dependence. The usually-observed dependence is presented in Figure 2.7, in which H_{eb} strongly increases at low film thicknesses until H_{eb} reaches a maximum and then slightly decreases. The reason for this dependence remains unclear, as all samples were grown using the same deposition conditions subsequently in a short period of time.

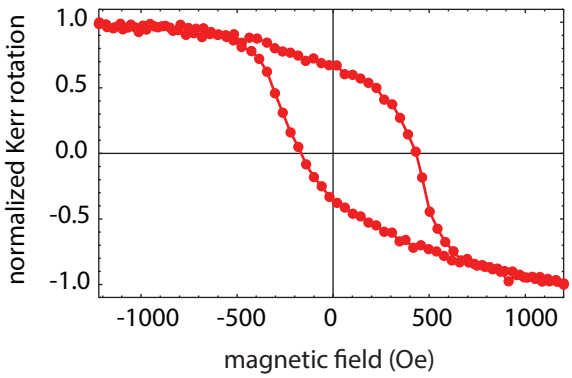

Figure 6.17 | MOKE measurement for a 30 nm thick $LaFeO_3$ film with a 2 nm thick Co bilayer.

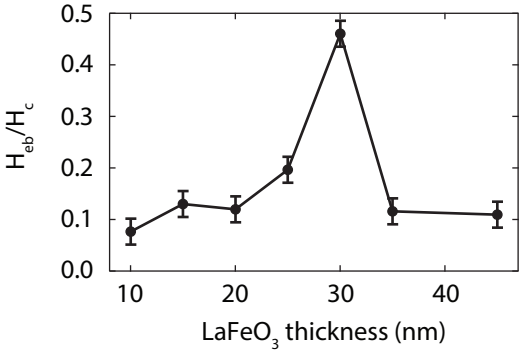

Figure 6.18 | The H_{eb} over H_c ratio as a function of $LaFeO_3$ film thickness.

According to Equation 2.11, the exchange energy can also be calculated for the $LaFeO_3$/Co bilayers. As H_{eb} is slightly larger when compared to the $BiFeO_3$/Co systems, the exchange energy and the effective unidirectional anisotropy constant are very similar to the $BiFeO_3$/Co films with $J_{eff} \approx 0.03 \frac{erg}{cm^2}$ and $K_{eff} \approx 3 \cdot 10^4 \frac{erg}{cm^3}$.

The exchange bias fields determined in this thesis are large in comparison to results published by other groups. Seo *et al.*[120] found a maximum exchange bias in $SrTiO_3$ (100)/$LaFeO_3$/Co bilayers of H_{eb}=12 Oe and a coercive field around $H_c \approx 800$ Oe.

As the coercivity in the bilayers grown in this work is very large for all thicknesses compared to the hysteresis shift, the ratio H_{eb}/H_c is smaller than unity (Figure 6.18). This makes the $LaFeO_3$ films non-ideal candidates for spintronic applications, however, they can still be used in devices that contain a pinned layer, as presented later in this section. As the ratio H_{eb}/H_c is the highest at an $LaFeO_3$ film thickness of 30 nm, bilayers of 30 nm thick $LaFeO_3$/2 nm Co are used for further detailed investigations.

In the following section, the influence of the *ex situ* annealing temperature and the determination of the blocking temperature are presented in detail. For these measurements the specimen were vacuum annealed *ex situ* in a furnace in a magnetic field. As the heating times become important, the temperature versus annealing time dependence is briefly discussed. Figure 6.19 presents the sample carrier temperature as a function of annealing time for a 15 min annealing process at 300°C. It is clearly visible that the ramping time is included in the 15 min. It takes 3 min to heat the sample carrier to 300°C. Thus, the effective time during which the sample was heated to the setpoint is a few minutes lower than specified.

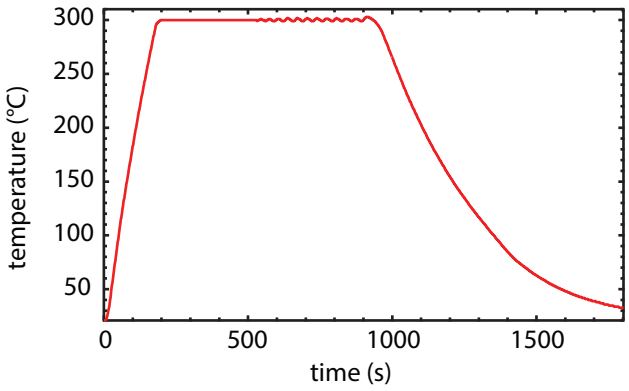

Figure 6.19 | Temperature versus time-dependence for a 300°C and a 15 min annealing process.

To study the influence of the *ex situ* annealing temperature on the strength of the exchange biasing of the Co layer, the bilayer was successively annealed at various temperatures for 15 min for each temperature in a magnetic field of 6.5 kOe. The magnetic field was applied in the same direction in all cases along the measuring direction. The resulting shifts of the hysteresis and the coercivity as a function of the annealing temperature derived from MOKE measurements are presented in Figure 6.20. In the as-prepared state, the bilayer already shows an exchange bias of H_{eb} = 41 Oe accompanied by an increased coercivity of H_c = 275 Oe. As the annealing temperature is increased, more and more magnetic domains are pinned and the shift of the hysteresis H_{eb} increases almost linearly up to H_{eb} = 133 Oe at a temperature of 130°C, while the coercive field H_c shows no strong variation with annealing temperature. Annealing at higher temperatures leads to decreasing H_{eb} and H_c, as excessive oxidation or diffusion takes place until the Co layer does not show any ferromagnetic behavior and, thus, H_{eb} and H_c drop to zero.

When heating a 30 nm $LaFeO_3$/2 nm Co bilayer for 15 min at 300°C in a magnetic field of 6.5 kOe it shows the same coercivity and shift of the hysteresis as the sample that was successively annealed up to 130°C. However, longer heating times (over 15 min) at 300°C also lead to a reduction of H_{eb} and H_c. In the following section the samples for magnetic measurements were heated at 300°C for 15 min.

Not only the process of heating the samples for long times or at high temperatures led to decreasing amplitudes of the magnetic properties, but the activation energy at room temperature leads to degradation of the magnetism and the

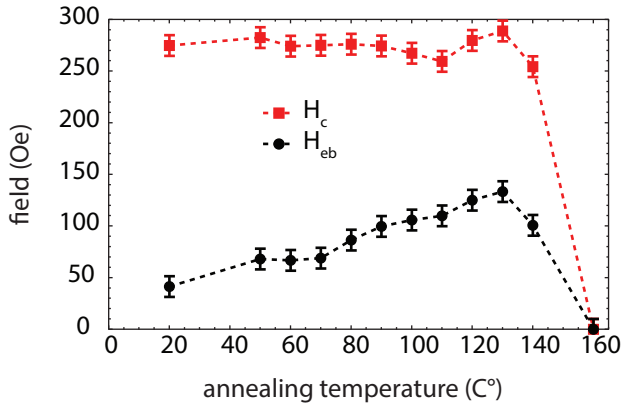

Figure 6.20 | H_{eb} and H_c as a function of the the post-annealing temperature. The heating time was 15 min and the applied magnetic field was 6.5 kOe.

pinning of the Co layer. Nevertheless, the following section will present an estimation of the blocking temperature of the thin $LaFeO_3$ films.

Blocking Temperature

Despite the temperature-induced oxidation or diffusion of the bilayers, an approximation of the blocking temperature is presented in this section by the conduction of a reverse field-cooling experiment[177] using a 30 nm $LaFeO_3$/2 nm Co sample. At first, the samples were annealed at 300°C for 15 min in order to induce a pinning of the Co layer. Afterwards, the direction of the magnetic field was applied in the opposite direction and the samples were heated to various temperatures in successive processes. Because of the influence of the annealing time and temperature on the exchange bias, each data point refers to a new specimen that was field-cooled in a reversed magnetic field only once. The resulting shift of the hysteresis as a function of reverse field-cooling temperature is shown in Figure 6.21.

For samples that were annealed at 20°C, i.e. room temperature, the hysteresis is shifted to negative field values of H_{eb}=126 Oe, i.e. to the values presented in the previous sections. With higher annealing temperatures and the magnetic field applied in the opposite direction to the initial field-cooling procedure, the shift of the hysteresis H_{eb} decreases and vanishes at an annealing temperature of 110°C. With higher annealing temperatures, the hysteresis shifts to the positive fields and H_{eb} increases to 65 Oe for a reverse field-cooling temperature of 300°C. Here, the influence of the heating time on the exchange coupling

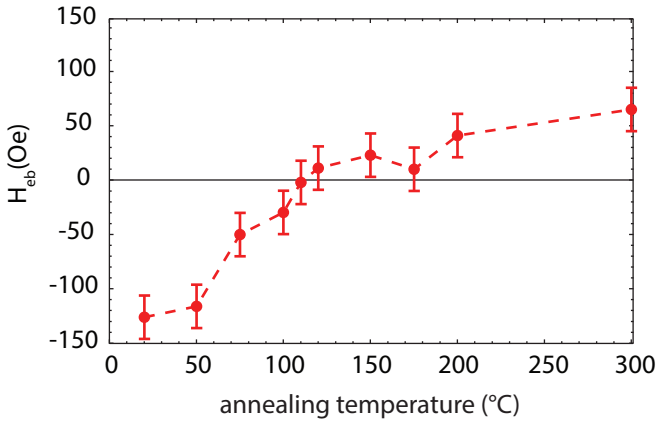

Figure 6.21 | Reverse cooling experiment: each data point refers to a sample that was annealed for 300°C for 15 min in 6.5 kOe to induce a pinning in the 30 nm $LaFeO_3$/2 nm Co bilayer and was, afterwards, heated for 15 min at various temperatures in a reversed magnetic field of the same strength.

between both films can be seen clearly, as $|H_{eb}|$ at 20°C and 300°C should be equal. Moreover, the temperature-induced degradation results in a flattening of the curve as indicated by different slopes for temperatures lower/higher than 110°C. The curve strongly increases for low temperatures, while the slope is lower at higher temperatures. The zero-crossing of the curve defines the median blocking temperature of the 30 nm $LaFeO_3$/2 nm Co bilayer to be $\langle T_B \rangle = 110\,°C$. As mentioned above, this value is an approximation to the actual blocking temperature.

This section presented investigations of the influence of annealing temperatures on the exchange bias in the $LaFeO_3$/Co bilayers and the determination of the optimal temperatures, as well as the blocking temperatures. The following section will present a discussion of the induced unidirectional anisotropy.

In-plane Anisotropy Distribution

This section presents in-plane rotational MOKE measurements in order to investigate the magnetic anisotropy distribution in the pinned Co layer. For this type of measurement, the sample was mounted on a rotating sample holder and hysteresis loops were recorded in steps of 10°. The resulting magnetic parameters, such as coercivity and remanence, are averaged over two or more hysteresis loops. Figure 6.22a presents the squareness ratio M_R/M_S as a function of rotational angle, where the 0° direction is parallel to the direction of the magnetic field that

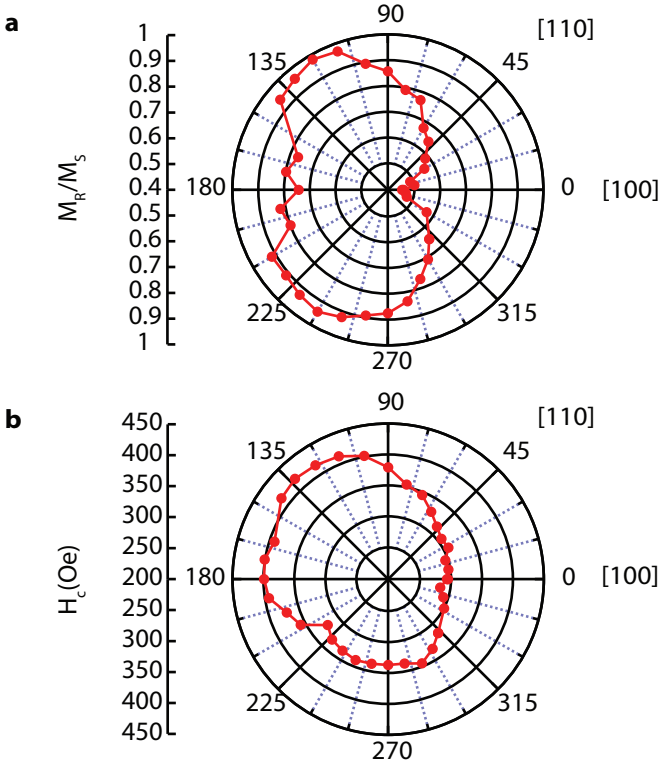

Figure 6.22 | Polar plot of **a** the squareness M_R/M_S and **b** the coercive field H_c as a function of the in-plane rotational angle for a 30 nm thick $LaFeO_3$ film with a 2 nm thick Co film.

was applied during the post-annealing process as well as to the $LaFeO_3$ [100] direction. The squareness data show a uniaxial anisotropy with two bumps along the 90° and 270° direction. Moreover, the curve exhibits a pronounced shift along the 180°-135° direction, i.e. antiparallel to the field-cooling direction, visualizing the presence of the unidirectional anisotropy induced in the Co layer. The corresponding coercive field H_c is presented in Figure 6.22b. The coercivity shows no uniaxial magnetic anisotropy and no distinctive features, as seen in the squareness. Even so, the pinning of the Co layer results in a pronounced unidirectional anisotropy component that causes a shift of the curve along the 180°-135° direction, as seen in the squareness data.

Moreover, these type of measurements directly yield the loop shift H_{eb} as a function of a rotational angle. The corresponding loop shifts versus in-plane rotational angle are presented in Figure 6.23. The curve shows a nearly-cosinuidal

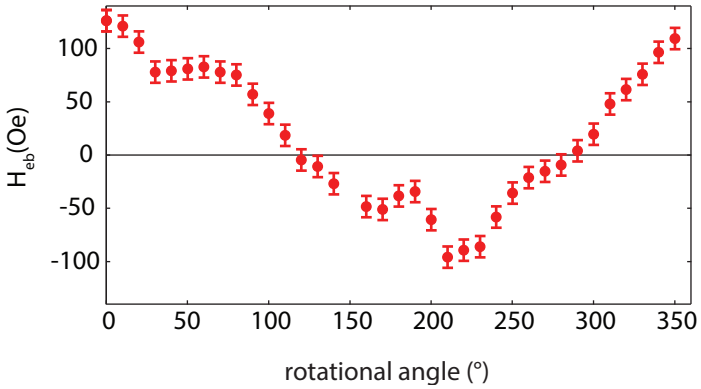

Figure 6.23 | The shift of the hysteresis H_{eb} as a function of the in-plane rotational angle.

angle dependence. At an orientation of 0°, i.e. along the field-cooling direction, the loop shift is maximal. With increasing rotational angle H_{eb} decreases to 0, where the field-cooling direction and the measuring direction are orthogonal. A further increase of the angle shifts H_{eb} to negative values. At an angle of 180°, the loop shift should be minimal. However, the determined H_{eb} versus rotational-angle shows a bump around 180°. Consequently H_{eb} is not minimal and does not exhibit the same but rather a negative amplitude comparable to 0°. This might be caused by a movement of the laser spot over the sample due to a misalignment of the sample. This leads to the assumption, that the bilayer shows inhomogenities resulting in different magnetic parameters. For larger angles the loop shift increases until it nearly reaches the same value as at 0°. Hence, the H_{eb} versus angle curve, in general, shows the expected dependence.

These sections presented the magnetic properties of the bilayers measured at room temperature, which is why the following section deals with the temperature-dependence of the magnitude of the exchange bias.

Temperature-Dependent AMR Measurements

In order to determine the coercivity H_c as well as the loop shift H_{eb} as a function of temperature, a 2 nm thick Co film on a 30 nm thick $LaFeO_3$ layer was patterned into a Hall bar structure with a length of 545 μm and a width of 196 μm, at which the AMR effect was measured as a function of temperature. For the measurements the probe current was applied parallelly to both the field-cooling direction and the applied magnetic field. Figure 6.24a shows the AMR curve measured at 20 K. The data points of each maximum were interpolated

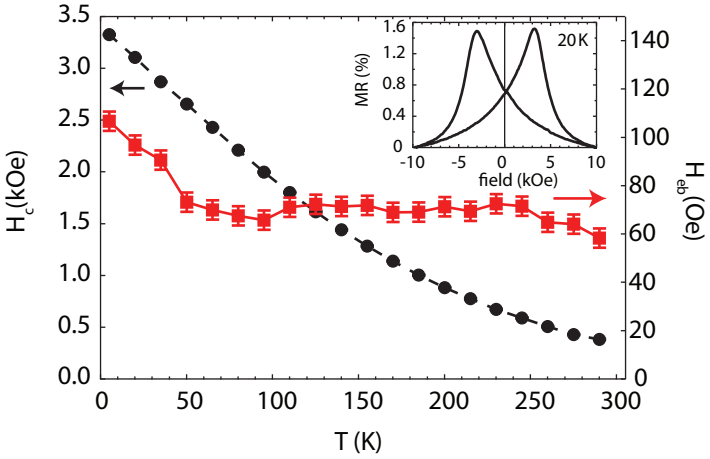

Figure 6.24 | Shift of the AMR curve, denoted by H_{eb} (red curve), and coercive field H_c (black curve) as a function of temperature. The inset shows the AMR measured at 20 K.

for an accurate determination of the field positions and the error margins in the graph. Accordingly, the coercive field H_c and the shift of the curve H_{eb} are determined. The resulting temperature-dependence of the loop shift H_{eb} is presented in Figure 6.24b. The curve starts at room temperature with H_{eb}=58 Oe, which is about half of the magnitude of the exchange bias found in the previous sections. This decrease might be related to the aging process/oxidation of the Co layer even at room temperature. Moreover, this indicates that there are areas of the sample, which might show smaller loop shifts and, thus, the resulting loop shift is reduced. H_{eb} remains nearly constant between room temperature and 50 K, where it starts to increase until it reaches its maximum of 107 Oe at 5 K. The corresponding temperature dependent coercivity is shown in Figure 6.24: It increases from 0.38 kOe at 290 K to 3.3 kOe at 5 K. As the anisotropy of the ferromagnet increases with lower temperatures, the coercive field also increases. This H_{eb} versus temperature-dependence looks similar to the one determined for the 12.5 nm $BiFeO_3$/2 nm Co bilayer in Figure 6.9, as both Co layers have a thickness of 2 nm.

Seo *et al.*[120] conducted measurements of the AMR effect in bilayers of $LaFeO_3$ 30 nm/Fe 8 nm on $MgAl_2O_4$ (100) substrates and found the same temperature-dependence of H_{eb} and H_c. Seo *et al.* found much smaller coercivities, which is caused by larger thicknesses of the ferromagnet in their work, along with slightly smaller exchange bias fields of around 20 Oe.

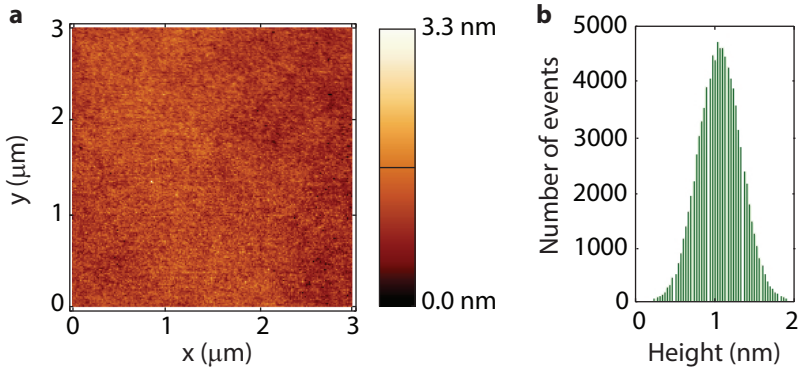

Figure 6.25 | a Surface topology of a 30 nm $LaFeO_3$/2 nm $Co_{70}Fe_{30}$/2 nm MgO film determined by AFM and **b** corresponding histogram of heights.

This section about the temperature-dependence of the magnetic properties completes the investigations of the exchange bias effect in the $LaFeO_3$/Co systems. The following section introduces investigations concerning the integration of $LaFeO_3$ films in devices.

6.2.4. $LaFeO_3$ in Devices

This section will present the ability to use the $LaFeO_3$ films in spintronic devices. For the application in devices it is necessary to have well-defined interfaces and smooth surfaces of the films. Thus, AFM measurements were performed on a 30 nm thick $LaFeO_3$ film with a 2 nm thick $Co_{70}Fe_{30}$ bilayer with 2 nm MgO capping to determine the surface morphology of the films. Here, a ferromagnetic $Co_{70}Fe_{30}$ layer was used instead of a Co layer as this results in smoother surfaces and promotes a better growth, for example for GMR devices. Figure 6.25a shows a representative AFM image of the surface. The surface is very smooth and shows no features. The RMS roughness of the film is 0.27 nm with a maximum roughness depth of 2 nm calculated using the histogram representation of the heights shown in Figure 6.25b. Hence, the roughness of the films is sufficient low enough to make them applicable for devices.

The next paragraph presents the investigations of a GMR element containing a $LaFeO_3$ film, which is used to induce an exchange bias in one of the electrodes allowing an antiparallel magnetization alignment. The fabricated GMR device consists of a layer stack as follows: $SrTiO_3$ (001)/15 nm $LaFeO_3$/2.75 nm $Co_{70}Fe_{30}$/2.2 nm Cu/2.75 nm $Co_{70}Fe_{30}$. Here, $Co_{70}Fe_{30}$ electrodes were used, as the effect amplitude could be strongly enhanced due to a better growth in

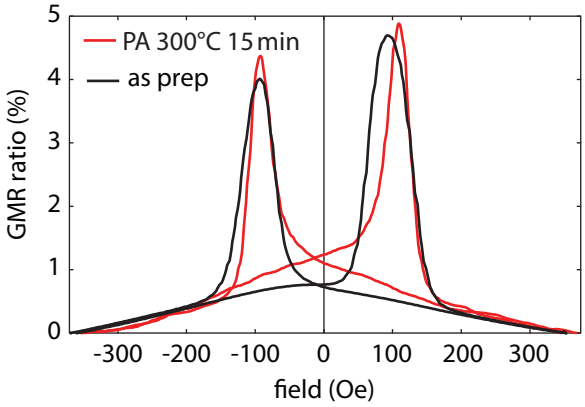

Figure 6.26 | GMR major loops for the as-prepared (black curve) and annealed (red curve) (for 15 min at 300°C in a magnetic field of 6.5 kOe) GMR stack with a $Co_{70}Fe_{30}$ electrode pinned by a $LaFeO_3$ film.

comparison to pure Co layers. A reference MOKE measurement of a 30 nm $LaFeO_3$/2 nm $Co_{70}Fe_{30}$ bilayer showed an exchange bias of H_{eb}=42 Oe and a coercivity of H_c=341 Oe. The sample was heated for 15 min at 300°C. Hence, the amplitude of the exchange bias is smaller when using a $Co_{70}Fe_{30}$ layer instead of a pure Co layer, but results in a better growth of the GMR structure.

For the growth of the GMR stacks and in order to choose a spacer thickness leading to an antiparallel alignment of the magnetization directions via the RKKY interaction, a Cu thickness of 2.2 nm was found to be optimal. The thickness for both ferromagnetic $Co_{70}Fe_{30}$ electrodes is the same in order to exclude different coercivities caused by different film thicknesses.

Figure 6.26 shows the resulting current in plane GMR measurements, where the current was applied parallel to both the pinning direction and the applied magnetic field. In the graph, the black curve represents the as-prepared stack, while the red curve represents the measurement of the annealed stack with an annealing temperature of 300°C for 15 min in a magnetic field during heating and cooling of 6.5 kOe. The measurement of the GMR effect for the as-prepared sample results in two relatively-broad peaks caused by the antiparallel magnetic alignment of the $Co_{70}Fe_{30}$ electrodes. Both peaks are centered around zero. Thus, the antiparallel magnetization alignment is achieved by different coercivities of the ferromagnetic layers. At small applied magnetic fields, the magnetization direction of the pinned bottom layer does not change, while the upper layer switches its magnetization direction. Large fields result in a parallel magnetization direction of both electrodes, when the externally applied field is

large enough to switch the pinned $Co_{70}Fe_{30}$ layer. The resulting GMR ratio is 4%. After annealing the layer stack, the peaks become sharper and more intense, leading to a slightly larger GMR ratio of 4.9% caused by a better antiparallel alignment of the magnetic electrodes. The field-cooling/annealing induces a small shift of the hysteresis while the coercivity remains constant. This results in a shift of the peaks to higher field values. Surprisingly, the resistance at zero field is higher for the annealed sample than for the as-prepared one, indicating a better parallel alignment for the as-prepared sample, in zero field.

6.2.5. Summary and Conclusion

In summary, highly-textured and single-crystalline $LaFeO_3$ films were grown using reactive sputtering from elemental La and Fe targets. Moreover, it was demonstrated that the films were highly epitaxial through nearly the whole film thickness. The optimization of the growth conditions revealed that neither the oxygen partial pressure nor the deposition temperature play such a crucial role as, for example, in the case of the $BiFeO_3$ films. A good crystallization of $LaFeO_3$ crystals is found for all temperatures and all oxygen partial pressures. The dependence on the lattice parameter is also small. The handling of the elemental La sputtering target is more challenging in comparison to the other used targets in this work, as it is highly reactive and rapidly forms a La_2O_3 tarnish. This effect also takes place inside the sputtering chamber when sputtering in the argon/oxygen atmosphere. Thus, it usually takes a while until an equilibrium at the surface of the sputtering target is reached between sputtering and oxidation of the La.

Furthermore, the antiferromagnetic structure of the $LaFeO_3$ films was confirmed as they were used to induce an exchange bias effect in the ferromagnetic Co-Fe films. A maximum loop shift of H_{eb}=133 Oe along with a coercivity of H_c=300 Oe was found for a 30 nm thick $LaFeO_3$ film with a 2 nm thick Co bilayer. Similar to the findings for the $BiFeO_3$ films, the exchange bias as a function of the thickness of the antiferromagnet shows a non-expected behavior. As discussed above, the influence of the deposition temperature is not pronounced, this behavior might not be related to problems with the heat transfer between the sample carrier and the substrate. The samples in this series were subsequently grown in a short period of time. To confirm the presence of the peak around 30 nm $LaFeO_3$ the series must be prepared again. In any case, for all film thicknesses high exchange bias values were found and the coercivity was larger than the loop shift. Nevertheless, by the fabrication of a GMR device containing an $LaFeO_3$ layer to pin the ferromagnetic Co-Fe

layer, the applicability of $LaFeO_3$ films for spintronic devices was proven. The pinning of the films could be induced using *ex situ* vacuum annealing, but again, a strong sensitivity of the magnetic properties on the temperature was found. The heating process and the impact of room temperature for a few weeks can destroy the ferromagnetic properties of the Co-Fe layer. This might be attributed to an excess of oxygen in the oxide films. This challenge has to be overcome before these films can be integrated into commercial devices. Nevertheless, the blocking temperature of the $LaFeO_3$ films was estimated to be in the range of 110°C.

Detailed investigations about the crystallographic properties, including the determination of the optimal growth conditions of $LaFeO_3$ crystals along with various investigations of the exchange bias effect in $LaFeO_3$/Co-Fe bilayers were presented in this section. The integration of $LaFeO_3$ films in a GMR device completes the section.

6.3. Comparison between $BiFeO_3$/Co-Fe and $LaFeO_3$/Co-Fe Systems

As both $BiFeO_3$ and $LaFeO_3$ films are very similar in their crystallographic structure and both materials are antiferromagnetic, this section will present a comparison between both systems.

Both oxides were grown via sputtering from elemental targets in an atmosphere of a mixture of oxygen and argon. For both materials the deposition temperature and the oxygen partial pressure were varied. The $BiFeO_3$ films were more sensitive to the oxygen partial pressure, as too low or too high pressure results in a under- or over-oxidation of the films. In the case of the $LaFeO_3$ films, no strong variations depending on the oxygen partial pressure were found. These findings are very similar to the deposition temperature, as the XRD patterns for the $LaFeO_3$ films are nearly unaffected with changing substrate temperatures. The crystallization of the $BiFeO_3$ films starts at temperatures around 600°C, at which the $BiFeO_3$ peaks are less intense. Hence, the deposition temperature is a crucial parameter for the growth of crystalline $BiFeO_3$ films.

Both materials can be used to induce an exchange bias in ferromagnetic Co-Fe layers. In both cases loop shifts in the same order of magnitude were observed, while the coercivity is very different for both bilayers. The maximum exchange bias in a 12.5 nm $BiFeO_3$/2 nm Co layer was H_{eb} = 92 Oe and H_c = 89 Oe. A 30 nm $LaFeO_3$/2 nm Co bilayer generated a maximum exchange bias of H_{eb} = 133 Oe and H_c = 300 Oe. As the ratio H_{eb}/H_c is an important

factor for the application in devices, $BiFeO_3$ films would be more suited for applications as $LaFeO_3$ films. The AMR measurements show an identical H_c versus temperature-dependence for both systems, as both Co layers are of the same thickness. A slight increase in the loop shift was found for low temperatures in the $LaFeO_3$/Co bilayer, while it was nearly constant for the $BiFeO_3$/Co bilayers.

Moreover, both materials exhibit a non-systematic or unexpected H_{eb} and H_c versus antiferromagnet thickness behavior. The reason for this could be a heat transfer between sample carrier and substrate, but it remains unclear.

However, the $BiFeO_3$/Co-Fe samples exhibit a very pronounced influence of the temperature, as an annealing of the samples or even the influence of the room temperature can lead to a strong decrease of the ferromagnetic properties of the Co-Fe films. This effect can also be observed for $LaFeO_3$/Co-Fe, but the decrease of the magnetic properties can be observed at higher temperatures or longer annealing times. Nevertheless, the room temperature has an impact on these samples as well, but less pronounced than for the $BiFeO_3$ systems. The higher temperature-stability of the $LaFeO_3$/Co-Fe samples allowed investigations of the *ex situ* temperatures on the magnetic properties as well as an approximation of the Blocking temperature of the $LaFeO_3$ film.

Rotational in-plane MOKE measurements revealed - in both cases - a pronounced unidirectional anisotropy in the Co films. The thin Co film grown on the $BiFeO_3$ layers revealed a fourfold anisotropy indicating a growth in the body centered tetragonal structure[174] compared to the uniaxial anisotropy measured in the thin Co films on $LaFeO_3$ layers. While the $LaFeO_3$ and the $BiFeO_3$ thin films have a very similar crystal structure with similar lattice parameters, the Co film was deposited on heated $BiFeO_3$ layers while it was deposited on $LaFeO_3$ layers at room temperature. This could explain the different crystallographic types of Co. Unfortunately, the Co films are too thin to investigate their orientation using the available XRD setup.

The easier treatment of the $LaFeO_3$ films is such that an *ex situ* annealing could be applied to induce an exchange bias as well as the smooth surfaces when using a $Co_{70}Fe_{30}$ layer, which was used for the integration into devices. This proof of the principle for the applicability in spintronic devices completes the investigations of the ferromagnetic Bi- and La-based ferrites.

7 Conclusion & Outlook

This thesis aimed at the investigation of improved materials for spintronic devices. Particularly, ferromagnetic Co-Fe-Si Heusler films and ferroelectric $BiFeO_3$ and $LaFeO_3$ films are promising to enable new techniques or improve recently-introduced devices in spintronics. Thus, these materials are intensively studied with a focus on their crystallographic and magnetic properties. Finally, a successful implementation of these materials into devices is demonstrated.

The results showed that the integration of $Fe_{1+x}Co_{2-x}Si$ layers as electrodes in MTJs offers an alternative to Co-Fe-B electrodes regarding high TMR effect amplitudes and low damping parameters. High TMR ratios were found for all stoichiometries in the series ranging from Co_2FeSi to Fe_2CoSi. The highest TMR ratio was found at the intermediate stoichiometry $Fe_{1.75}Co_{1.25}Si$ with 159% at room temperature and 262% at 15 K, respectively. Such high effect amplitudes are essential for spintronic devices and allow for an accurate read-out and, thus, reduce the required amplification in the application-specific integrated circuit (ASIC)[178].

Moreover, very small Gilbert damping parameters ranging from $0.0012\pm^{0.0007}_{0.0001}$ to $0.0019\pm^{0.0007}_{0.0001}$ were found for all Co-Fe-Si Heusler compounds. The lowest damping was again found for $Fe_{1.75}Co_{1.25}Si$, with $\alpha = 0.0012\pm^{0.0007}_{0.0001}$. A low magnetization damping is substantial for the use of STT assisted switching, as this leads to low switching current densities. This makes the complete series, but especially the compound $Fe_{1.75}Co_{1.25}Si$, an ideal electrode for STT-MRAMs. The high effect amplitudes and small damping parameters can be related to the good crystalline ordering, as well as the high degree of epitaxy of the films.

In the future, the ability of STT assisted switching of the MTJs including the Co-Fe-Si films, has to be proven. For the integration of thin $Fe_{1+x}Co_{2-x}Si$ films in commercial devices, the need of single-crystalline substrates, such as MgO

substrates, has to be overcome. The deposition process of Co-Fe-Si films grown on Si substrates using a V[179] or TiN[180] with MgO buffer layer should be optimized in order to obtain a similar film quality. Moreover, the post-annealing temperatures of 500°C are challenging and too high for the ASIC, but an often used solution is the separation of the TMR cells and the ASIC into two different circuit boards.

The thin $BiFeO_3$ and $LaFeO_3$ films have proven to provide an exchange bias that is sufficiently-high for their implementation in future devices. To achieve this goal, highly epitaxial antiferromagnetic $BiFeO_3$ and $LaFeO_3$ films are grown using reactive co-sputtering from elemental Bi, La, and Fe targets. Both materials can be used to induce an exchange bias in a coupled ferromagnetic layer. The highest exchange bias fields along with the smallest coercivity of H_{eb} = 92 Oe and H_c = 89 Oe were found for a 12.5 nm $BiFeO_3$/2 nm Co bilayer. As the loop shift is larger than the coercivity, this bilayer is interesting for spintronic applications. In the $LaFeO_3$/Co-Fe bilayers, the coercivity is larger than the loop shift with maximum values of H_{eb}=133 Oe along with a coercivity of H_c=300 Oe, which was found for a 30 nm thick $LaFeO_3$ film with a 2 nm thick Co layer. The integration of $LaFeO_3$ films in current-in-plane GMR stacks proved their ability in spintronic devices, as the loop shift is large enough to obtain an antiparallel magnetic alignment. Nevertheless, the application of $BiFeO_3$ and $LaFeO_3$ films for their use in MRAMs or current-perpendicular-to-plane GMR stacks is challenging, as the oxides are insulating and the thin ferromagnetic layers would lead to a high resistivity of the supply line. The thickness of the metallic films can be increased by using an artificial antiferromagnet as en electrode. A possible stack could be like the following: $SrTiO_3$ (001)/15 nm $LaFeO_3$/2.75 nm $Co_{70}Fe_{30}$/0.9 nm Ru/3 nm $Co_{70}Fe_{30}$/2.2 nm Cu/2.75 nm $Co_{70}Fe_{30}$. The thickness of the Ru layer should be chosen in order to achieve either a ferromagnetic or antiferromagnetic coupling using the RKKY interaction. Another possibility is the doping with elements such as Ca in order to increase the electrical conductivity[181].

Another obstacle is the temperature-induced instability, which was observed for the $BiFeO_3$/Co and $LaFeO_3$/Co bilayers. This has to be overcome for their integration in spintronic devices.

One of the most interesting properties of the ferrite films is their ferroelectric behavior. Future studies should aim at exploiting these properties. The easiest experimental approach to study the influence of an externally-applied electric field on the electric polarization and, hence, the magnetization, is sandwiching the $BiFeO_3$ and $LaFeO_3$ films between two conducting layers. To maintain high-quality ferroelectric films, the choice of a matching conducting buffer

layer is crucial. A possible candidate is $SrRuO_3$[182], a perovskite itself with a lattice parameter of 3.93Å in the pseudocubic notation. This value is very similar to the ones of the ferroelectric $BiFeO_3$ and $LaFeO_3$.[1] By the use of a Sawyer-Tower circuit[183], the ferroelectric materials can be investigated in order to test the films for polarization switching. Since it is not known if $BiFeO_3$ and $LaFeO_3$ are actually ferroelectric, these measurements are of large interest for future investigations. Afterwards, the ferroelectric films should be integrated in magnetic tunnel junctions as ferroelectric and insulating barriers, referred to as the ferroelectric tunnel junction (FTJ)[10,11]. Spintronic devices such as MRAMs on the basis of FTJs are of tremendous impact, as they are predicted to increase significantly the signal amplitude along with a non-destructive read-out and low power consumption, but without the disadvantages of FeRAMS, such as the limitation of the miniaturization of devices. Moreover, FTJs can be used for memristive devices.

[1] A corresponding sputtering target for these kinds of measurements for this dissertation was ordered, but, unfortunately, it was not in the desired quality to grow the $SrRuO_3$ layers.

A Deformation Mode Transitions in Amorphous - Cu45Zr55/ Crystalline - Cu Multilayers

Although the main topic of this thesis is the study of materials for spintronic applications, this chapter will focus on a different topic: the study of the mechanical behavior of bulk metallic glasses. This research was performed during a two-month stay in the course of a summer internship program at the MINT Center and the Department of Metallurgical and Materials Engineering at the University of Tuscaloosa, Alabama, USA, in 2014.

The growth of the films and the subsequent investigations of the mechanical properties along with the application of the electron imaging techniques were performed by myself, whereas the theoretical modeling was performed by Chuang Deng, Department of Mechanical Engineering, University of Manitoba, Winnipeg, Canada. A publication based on these results was submitted to Thin Solid Films and is currently under review. As this topic is only secondary, a detailed presentation of the fundamentals is not provided. In fact, there are many books offering a good understanding of the basics of bulk metallic glasses, the Nanoindentation technique, and the molecular dynamics' simulation, such as References[184,185].

Metallic glasses (MGs) are featured with their exceptional mechanical properties, such as high strength and hardness. However, they suffer from negligible ductility due to strain-localization and further shear banding, which results in catastrophic failure[186,187]. When crystalline phases are incorporated into the glassy matrix, these phases are able to mitigate the catastrophic shear band behaviors with improvements in ductility and toughness[188–191]. This enhanced mechanical performance highlights the importance of the interplay of distinct deformation mechanisms between the amorphous and crystalline phases. The coupled deformation behaviors hinge on the intrinsic material properties, including the crystalline and amorphous phase states, the crystalline-amorphous

interface, the microstructural length scale setting by the inter-phase spacing, and the extrinsic loading conditions with respect to the interfaces. To delineate these factors in MG composites, the amorphous-crystalline multilayered structure presents a model system. The use of multilayers allows for a controlled growth of crystalline and amorphous phases and thus a systematic study of deformation behaviors[192–195]. Recent studies on such amorphous/nanocrystalline (e.g., CuZr/Cu) multilayers have revealed that when the layer thickness is carefully tuned, a multilayer structure can suppress the formation of catastrophic shear bands and enable plastic co-deformation of both phases. In these studies, the CuZr and Cu layers usually remained of equal thickness, allowing for the transition of deformation behaviors to emerge from the length scale effect of both the amorphous and crystalline phases[193,196]. To date, the influence of the crystalline layer thickness on the shear band morphology of the amorphous phase is not fully clarified.

For this research, multilayers of amorphous Cu45Zr55 (at/%) and nanocrystalline Cu of varying thicknesses were grown and investigated in terms of shear band propagation. A transition of deformation modes from shear banding to co-deformation of the amorphous and crystalline phases was observed as the thickness of crystalline Cu layer increased from 5 nm to 150 nm. This transition was signified by a diminishing of "pop-in" or serrated flow events in the load-displacement curves for the nanoindentation tests. Further confirmation was noted by the deformation patterns around the indents as viewed by scanning electron microscopy (SEM) images. To better understand the underlying deformation mechanisms for this transition, molecular dynamics (MD) simulations were employed, with particular emphasis on the roles played by the crystalline-amorphous interfaces in shear banding as the crystalline layer thickness varies.

A.1. Preparation and Characterization Techniques

The films were deposited in a UHV dc-magnetron sputtering system with a base pressure of about $1 \cdot 10^{-8}$ Torr. The Cu45Zr55/Cu multilayers were grown from elemental Cu and Zr targets at room temperature on Si (100) substrates. Energy-dispersive X-ray spectroscopy and X-ray reflectivity were performed to monitor the stoichiometry and the film thickness, respectively. The total film thickness was about $4\mu m$ in all cases to minimize substrate effects during nanoindentation as well as to ensure that reasonable indentation data could be measured from at least two bilayers[197]. The thickness for the Cu45Zr55 layers was fixed at 150 nm, while the thickness of the Cu layers was 5 nm, 12.5 nm,

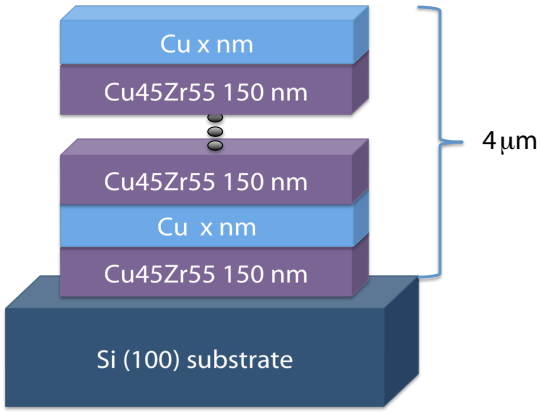

Figure A.1 | Sketch of the grown CuZr / Cu multilayers with a total film thickness of 4 μm.

25 nm, 50 nm, 100 nm, and 150 nm. See Figure A.1 for an illustration of the grown multilayer systems.

Nanoindentation was conducted using an Agilent Nano Indenter G200 with a Berkovich diamond indenter tip. To measure Young's modulus and the hardness, continuous stiffness measurements (CSM) were performed[198]. This technique superimposes a small oscillating force with small amplitude to the force of the tip. This provides an accurate and constant measurement of the contact stiffness. To image the microstructure of the indents, a dual beam Focus Ion Beam (FIB) with Field Emission Gun SEM (Tescan LYRA FIB-FESEM) was used. To look at the cross section of the deformed multilayer structure, both a FIB lift out transmission electron microscopy (TEM) foil and a SEM sub-surface viewing prospective was prepared. A thin Pt bar was deposited across the indent to prevent/reduce Ga+ implantation damage in the film during milling. For the SEM imaging, a single trench was then milled normal to the Pt bar to reveal the layered structure and shear bands. For the TEM foil, a secondary trench was milled on the other side of the Pt bar whereupon a thin foil under the bar was extracted. In both preparation methods, the cross-section was ion-polished with low ion currents and acceleration voltages to clean the surface from any milling damage that occurred at higher energy settings.

A.2. Theoretical Approach

To unveil the mechanisms, the MD simulations of nanoindentation on the Cu45Zr55/Cu multilayered structures were performed by using LAMMPS[185] with an embedded atom method potential for a Cu-Zr system developed by Mendelev *et al.*[199]. The simulated Cu45Zr55 metallic glass was created by following a heating-and-quenching procedure[199]. The amorphous-crystalline multilayered structure was then constructed with alternating Cu45Zr55 (10 nm) and crystalline Cu layers (2 nm and 10 nm). Grain boundaries perpendicular to the amorphous-crystalline interface were also created in the crystalline Cu layer to make the simulation more realistic to the experimentally synthesized microstructure. The width and thickness of the simulation box, i.e. the dimensions parallel to the amorphous-crystalline interface, was fixed, respectively, at 102 nm and 1.6 nm while the total height was 48 nm and 40 nm, respectively, for the structures with 2 nm and 10 nm Cu layer thicknesses. The MD simulation systems were smaller when compared to the experiments to accommodate for a reasonable computational volume. As will be shown below, this smaller model system was found to be sufficient in capturing the deformation mode transitions that was helpful in understanding the experimental findings. The time step for the MD simulations was 5 fs. Periodic boundary conditions were applied along the directions parallel to the amorphous-crystalline plane while the sample surface (the direction perpendicular to the amorphous-crystalline interface) was kept free. Nanoindentation loading was simulated by moving a cylindrical virtual indenter of radius R=40 nm at a constant velocity of 5 m/s towards the sample surface[200]. Several atom layers at the bottom were fixed during the indentation. A canonical ensemble (NVT) was maintained during the indentation process with T=10 K. Here the low temperature of T=10 K was chosen to ensure clear shear localization in the amorphous layer[200].

A.3. Crystallographic Structure

Figure A.2 shows X-ray diffraction scans for the pure 4 μm thick Cu45Zr55 sample, the 4 μm Cu layer, and the various multilayers. The Cu45Zr55 layers exhibited a diffuse peak near $2\Theta = 43.3°$, confirming the amorphous structure. The thin Cu layers exhibited a strong (111), fiber texture with minor (200) and (220) reflections noted as larger film thicknesses. The grain structure can be seen in the cross-sectional SEM images (ref. to Figure A.4c).

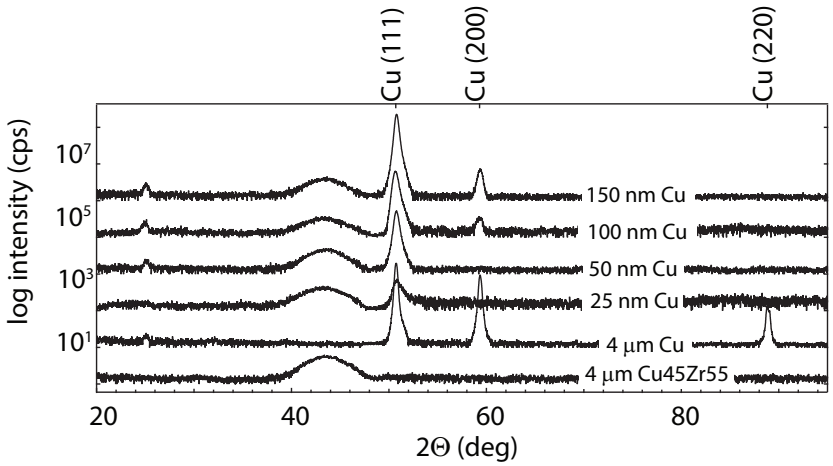

Figure A.2 | XRD pattern of the multilayers, the 4 μm Cu and the 4 μm Cu45Zr55 films.

A.4. Mechanical Behavior

Figure A.3b shows representative load versus displacement curves for the 4 μm thick amorphous Cu45Zr55 film along with the multilayers at Cu thicknesses of 5 nm, 12.5 nm, 25 nm, and 50 nm Cu layers. Each measurement was taken at a strain rate of 0.01 s^{-1}. As the thickness of the Cu layer increased, a transition from serrated to smooth responses was found. For the amorphous film, the load-displacement curve was serrated and featured discrete "pop-in" events. The serrations of the amorphous films have contributed to the formation and propagation of shear bands[187], which has been previously noted (and seen but not shown) as steps in the pile-up regions around the indent impression[192]. The load-displacement results for the multilayer with the 5 nm Cu layers revealed a behavior very similar to that of the single amorphous Cu45Zr55 film's curve. At a Cu layer thickness of 12.5 nm, less serrated flow was visible and the curve became smoother. Only a few "pop-in" events were visible. With increasing Cu layer thicknesses from 25 nm to 50 nm, the number of displacement bursts decreased and the "pop-in" events became even less pronounced. Thus, it was expected that near a Cu layer thickness of 25 nm, the shear banding behavior changes in the 150 nm amorphous Cu45Zr55 layer of the multilayer.

The hardness data is shown in Figure A.3b. The hardness decreased with increasing Cu layer thickness, i.e. 5 nm to 150 nm, which can be generally attributed to the increased amount of softer Cu layers[192]. Interestingly, when

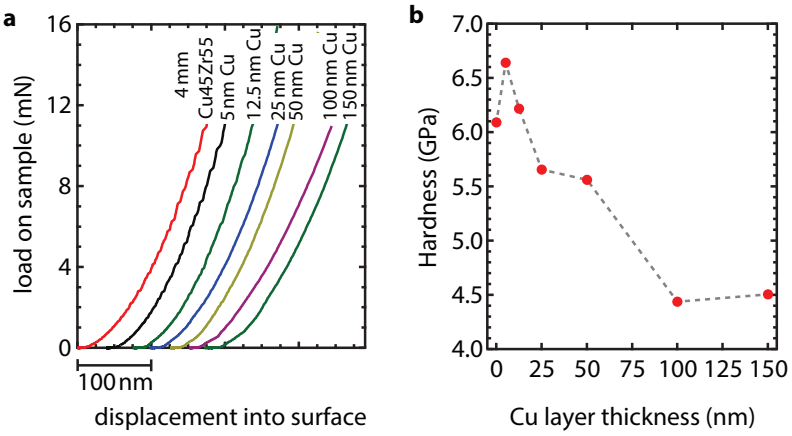

Figure A.3 | a Load on sample as a function of the displacement for the 4 μm Cu45Zr55 film and for the multilayers with 5 nm, 12.5 nm, 25 nm, and 50 nm Cu interlayers at a strain rate of 0.01 s^{-1}. **b** Hardness for all Cu layer thicknesses and the 4 μm Cu45Zr55 film measured at a strain rate of 0.01 s^{-1}.

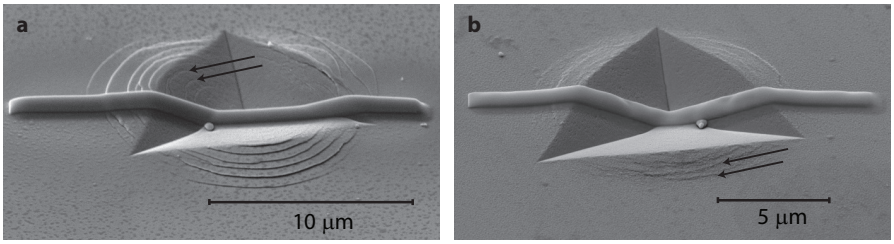

Figure A.4 | a SEM image shows piled up material of indent in the 4 μm Cu45Zr55 amorphous film with Pt bar. **b** The SEM image of the indent in the multilayer with 150 nm Cu interlayer and Pt bar.

the Cu layers were 5 nm and 12.5 nm thick, the hardness had larger value than that of the single amorphous phase film. This augmentation can be directly related with the shear banding behaviors. When the Cu layer was very thin, shear bands could propagate through the Cu layer and continue deep into the sample[192]. These types of "sheared Cu" layers could serve as an additional obstacle along the shear band path, which increased the hardness or difficulty to propagate the bands because of the extra energy necessary to shear though these particular crystalline layers.

The SEM images of the indents on the surface of the films are shown in Figure A.4. The depth of indentation was 2 μm for all SEM images. A series of steps around the periphery of the indenter tip reflected the burst of localized strain

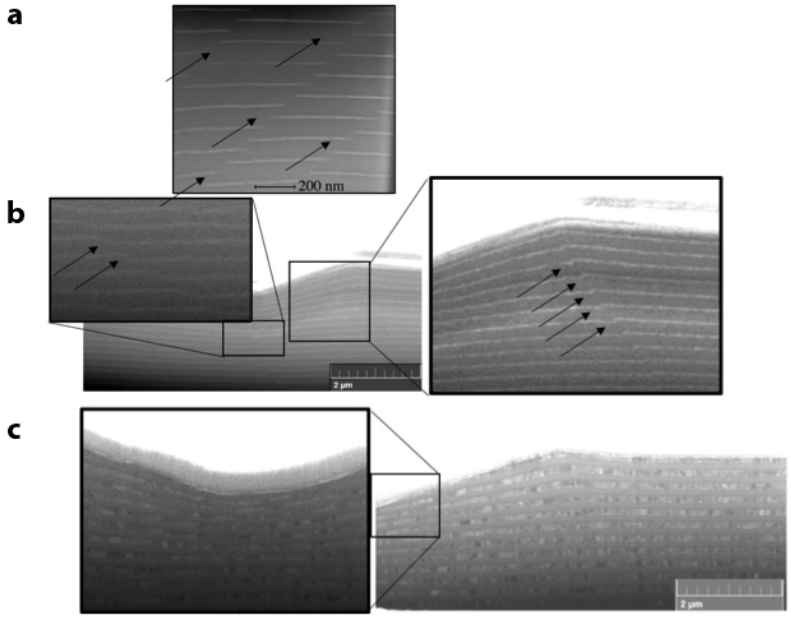

Figure A.5 | a TEM image of shear bands in the sample with 5 nm thick Cu interlayers underneath the indent. Note the arrows highlighting the split in the Cu layers and location of the shear band. **b** SEM cross-sectional image of the indentation at the 25 nm Cu layered sample. The magnified image near and under the indent reveals bent, but not broken, Cu layers indicated by the arrows. **c** SEM cross-sectional image of the 150 nm Cu layered sample. Here, the Cu layer does not appear to be bent or sheared but undergoing continuous co-deformation with the amorphous phase.

and usually pointed to the existence of shear bands in amorphous metals[201]. The 4 μm Cu45Zr55 sample revealed significant deformed material close to the residual imprint of the tip. Discrete steps with large spacing, indicated by the arrows in the image, were clearly visible in the deformed surface (Figure A.4a). Figure A.4b shows the indent into the 150 nm Cu multilayered sample with the Pt bar over its surface. Here, a piled-up region of material around the indenter was observed but with a qualitatively larger number of smaller steps, which were less spaced between each step. This indicated that the formation and propagation of catastrophic shear bands were suppressed when the thickness of the inserting Cu layers was increased.

Figure A.5a is a TEM image of shear bands in the sample for 5 nm thick Cu layers after indentation. It can be clearly seen that at this thinnest Cu layer

thickness, the shear band physically separated the Cu layers and continued to propagate through the sample. Upon increasing the Cu layer thickness to 25 nm, the Cu layers were no longer split but bent, evident by the arrows pointing to the localized deformation in the SEM micrograph of Figure A.4b. The inset images of Figure A.5b are regions next to and under the indent. Upon increasing the Cu layer thickness to 150 nm, the Cu layers were neither broken nor locally bent in response to the shear band propagation and both phases appeared to co-deform. These microstructure responses are consistent with the serrated to continuous flow noted in the indentation responses in Figure A.3b.

A.5. Theoretical Modeling

Thus, a transition effect of Cu's influence on shear band propagation can be concluded from these experiments. To understand this transition, a series of MD simulations were performed. Though these simulations are for slightly-different layer thicknesses than the experiments, as noted above, because of computational limitations for such large layers, they still provide useful insights into the mechanisms that give rise to the transition. As can be seen in the simulation images of Figures A.6a and A.6c, the plastic events in all multilayers were first initiated by shear transformation zones (STZs) in the top-most amorphous layer. How the STZs propagate was found to be dependent on the Cu layer thickness, as noted in our experiments. For a 2 nm Cu layer, the STZs became activated in the subsequent amorphous layers below the Cu layer before dislocations were nucleated in the crystalline layer. This can be seen by the highly-localized strain region within that second amorphous layer while the Cu layer was still intact above the region. Figure A.6b revealed that upon further indenting, the localized shear in the amorphous layers on either side of the Cu layer appeared to result in a spatial correlation that then lead to the shearing of the Cu layer and propagation of the shear bands. The further propagation of the shear bands into the film followed the same behavior. This can be inferred from the localized higher shear strain seen in the amorphous layers on either side of the subsequent Cu layer.

Since grain boundaries can also serve as stress concentrator and dislocation nucleation sources in polycrystalline metals, these features were added to the model. As can be seen in Figure A.6c, in the 10 nm Cu layer, with the grain boundaries (GB) highlighted by the arrows, no direct evidence of dislocation strain localization associated was observed in these grain boundaries upon indention. However, the STZs were localized in the amorphous layers. Upon further indentation of the 10 nm Cu layer, Figure A.6d, the onset of strain

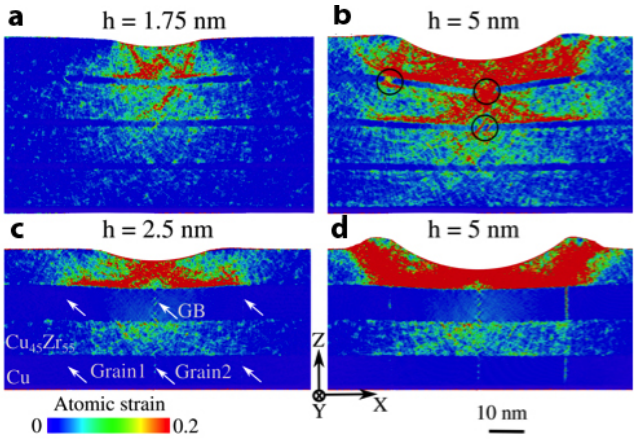

Figure A.6 | a and **b** show the atomistic configuration of the multilayer with 2 nm Cu layer at indentation depth h=1.75 nm and 5 nm, respectively. **c** and **d** demonstrate the atomistic configuration of the multilayer with 10 nm Cu layer at indentation depth h=2.5 nm and 5 nm, respectively. The white arrows indicate the location of grain boundaries in all Cu layers. The black circles highlight the plastic deformation in the 2 nm Cu layer. The atom colors correspond to their local von Mises strain[202]. The orientations of grain 1 and 2 along the x-, y-, z-directions are [110], [-110], [001] and [001], [1-10], [110], respectively.

localization in the subsequent amorphous layer under the Cu layer was observed, as described in the preceding paragraph. However, it was significantly less than that observed for the thinner 2 nm Cu layer simulation, as shown in Figure A.6b. For an equivalent indent depth between the 2 nm and 10 nm Cu layers, the propagation of the shear band was halted for the thicker Cu layer evident by the increased strain within the upper-most amorphous layer and a reduction of such an effect in the subsequent layers below the Cu interlayer. This suggested that the Cu layers appeared to break down the spatial correlation of STZs along the shear path between the two amorphous layers that were separated by the Cu interlayer.

The serrated-to-smooth transition, as shown in Figure A.3b, may be a result of the STZ events confined into the top few layers as the Cu thickness increased, as they can now act as a strong barrier to this spatial correlation of STZs at the amorphous-crystalline interfaces (as shown in Figure A.5b) and further suppress the formation of shear bands. The highly-localized deformation can be attributed to the reduced hardness as a consequence of strain-softening accompanied with STZs[203,204].

A.6. Conclusion

The systematic study of the role of different Cu layer thicknesses (5-150 nm) in a fixed 150 nm layer thickness of amorphous Cu45Zr55/Cu multilayer revealed a suppression of shear band propagation. At 5 nm Cu layer thicknesses, the shear bands were able to clearly separate the Cu layers. Upon increasing the Cu thickness to 25 nm, the shear band was able to locally bend the Cu at the shear propagation locations but not physically split the Cu layer. Finally, at 150 nm of Cu, the two phases co-deformed with no clear evidence of shear propagation through the multilayer structure. MD simulations reveal that upon indentation, strain localization formed in the upper-most amorphous layer and its progression is dependent on the mode of deformation of the Cu layer and its thickness. This creates a deformation-based transition. The MD simulations also revealed, for very thin Cu layers, that the strain-localization in the amorphous layer on either side of the Cu layer created a spatial correlation condition that sheared the Cu layer from both sides. If the Cu layer became sufficiently thick, it suppressed the formation and continual propagation of these shear bands further into the thickness of the multilayer and both layers co-deformed in response to the indentation load.

B Bibliography

[1] S. A. Wolf *et al.*, *Science* **2001**, *294*, 1488.

[2] G. Binasch *et al.*, *Phys. Rev. B* **1989**, *39*, 4828.

[3] M. N. Baibich *et al.*, *Phys. Rev. Lett.* **1988**, *61*, 2472.

[4] M. Julliere, *Phys. Lett. A* **1975**, *54*, 225.

[5] S. Tehrani *et al.*, *IEEE Trans. Magn.* **1999**, *35*, 2814.

[6] J. Slonczewski, *J. Magn. Magn. Mater.* **1996**, *159*, L1.

[7] Spin-Torque MRAM Technology, **2016**, `http://www.everspin.com/spin-torque-mram-technology` (visited on 09/01/2016).

[8] T Jungwirth *et al.*, *Nat. Nanotech.* **2016**, *11*, 231.

[9] Cypress Semiconductor, `http://www.cypress.com` (visited on 09/01/2016).

[10] E. Tsymbal *et al.*, *Ferroelectric and multiferroic tunnel junctions*, *Vol. 37*, Cambridge University Press, New York, USA, **2012**, p. 138.

[11] E. Tsymbal, A Gruverman, *Nat. Mater.* **2013**, *12*, 602.

[12] I. Galanakis, P. H. Dederichs, N. Papanikolaou, *Phys. Rev. B* **2002**, *66*, 174429.

[13] C. Sterwerf, *Diploma thesis in Physics - Integration of Co_2FeSi and Fe_2CoSi*, **2012**.

[14] C. Sterwerf *et al.*, *IEEE Trans. Magn.* **2013**, *49*, 4386.

[15] C. Sterwerf *et al.*, *J. Appl. Phys.* **2016**, *120*, 083904.

[16] C. Sterwerf *et al.*, *IEEE Trans. Magn.* **2016**, *52*, 1.

[17] J Nogués, I. K. Schuller, *J. Magn. Magn. Mater.* **1999**, *192*, 203.

[18] A. Berkowitz, K. Takano, *J. Magn. Magn. Mater.* **1999**, *200*, 552.

[19] T Zhao *et al.*, *Nature materials* **2006**, *5*, 823.

[20] J. R. Teague, R Gerson, W. J. James, *Solid State Commun.* **1970**, *8*, 1073.

[21] S. Acharya *et al.*, *Mater. Lett.* **2010**, *64*, 415.

[22] J. Coey, *Magnetism and Magnetic Materials*, Cambridge University Press, **2010**.

[23] *Radio Frequency Techniques, in: Ultrathin Magnetic Structures II*, (Eds.: B. Heinrich, J. Bland), Springer, **1994**, p. 195.

[24] M. A. Ruderman, C. Kittel, *Phys. Rev.* **1954**, *96*, 99.

[25] T. Kasuya, *Prog. Theor. Phys.* **1956**, *16*, 45.

[26] K. Yosida, *Phys. Rev.* **1957**, *106*, 893.

[27] T. Moriya, *Phys. Rev.* **1960**, *120*, 91.

[28] Dzyaloshinskii, *J. Exp. Theor. Phys.* **1957**, *5*, 1259.

[29] J. Lindner, M. Farle in *Magnetic Heterostructures: Advances and Perspectives in Spinstructures and Spintransport*, (Eds.: H. Zabel, S. D. Bader), Springer Berlin Heidelberg, Berlin, Heidelberg, **2008**, p. 45.

[30] M. Farle, *Rep. Prog. Phys.* **1998**, *61*, 755.

[31] F. Radu, H. Zabel, *Springer Tracts Mod. Phys.* **2008**, *227*, 97.

[32] W. H. Meiklejohn, C. P. Bean, *Phys. Rev.* **1956**, *102*, 1413.

[33] W. H. Meiklejohn, C. P. Bean, *Phys. Rev.* **1957**, *105*, 904.

[34] J. Nogués *et al.*, *Phys. Rep.* **2005**, *442*, 65.

[35] D. Lederman *et al.*, *Phys. Rev. B* **1993**, *48*, 8365.

[36] M. Tsunoda *et al.*, *J. Magn. Magn. Mater.* **1997**, *171*, 29.

[37] Y. Tsuchiya *et al.*, *Mater. Trans. JIM* **1997**, *38*, 91.

[38] J. Nogués *et al.*, *Appl. Phys. Lett.* **1996**, *68*, 3186.

[39] A. Hoffmann, *Phys. Rev. Lett.* **2004**, *93*, 097203.

[40] Schlenker, C., Paccard, D., *J. Phys. France* **1967**, *28*, 611.

[41] W. H. Meiklejohn, *J. Appl. Phys.* **1962**, *33*, 1328.

[42] J. Nogués *et al.*, *Phys. Rev. Lett.* **1996**, *76*, 4624.

[43] C. Leighton *et al.*, *Phys. Rev. B* **1999**, *60*, 12837.

[44] C. Binek, A. Hochstrat, W. Kleemann, *J. Magn. Magn. Mater.* **2001**, *234*, 353.

[45] R. Jungblut *et al.*, *J. Appl. Phys.* **1994**, *75*, 6659.

[46] L. Néel, *Ann. Phys. (France) 1* **1967**, *61*, 469.

[47] L. Néel, *C.R. Acad. Sci. Paris Serie C* **1967**, *1002*, 264.

[48] D. Mauri *et al.*, *J. Appl. Phys.* **1987**, *62*, 3047.

[49] M. Kiwi *et al.*, *Solid State Commun.* **2000**, *116*, 315.

[50] M. Kiwi *et al.*, *Europhys. Lett.* **1999**, *48*, 573.

[51] M. Kiwi *et al.*, *Appl. Phys. Lett.* **1999**, *75*, 3995.

[52] J. Geshev, *Phys. Rev. B* **2000**, *62*, 5627.

[53] J.-V. Kim *et al.*, *Phys. Rev. B* **2000**, *61*, 8888.

[54] J.-V. Kim, R. L. Stamps, *Phys. Rev. B* **2005**, *71*, 094405.

[55] A. P. Malozemoff, *Phys. Rev. B* **1988**, *37*, 7673.

[56] A. P. Malozemoff, *J. Appl. Phys.* **1988**, *63*, 3874.

[57] A. P. Malozemoff, *Phys. Rev. B* **1987**, *35*, 3679.

[58] N. C. Koon, *Phys. Rev. Lett.* **1997**, *78*, 4865.

[59] T. C. Schulthess, W. H. Butler, *Phys. Rev. Lett.* **1998**, *81*, 4516.

[60] R. Castillo, *Functional Nanostructures Fabricated by Focused Electron/Ion Beam Induced Deposition*, Springer International Publishing, **2013**.

[61] R. C. O'Handley, *Modern Magnetic Materials*, John Wiley and Sons, Inc, **2000**.

[62] S. M. Thompson, *J. Phys. D: Appl. Phys.* **2008**, *41*, 093001.

[63] W. Thomson, *Proc. R. Soc. Lond.* **1856**, *8*, 546.

[64] J Smit, *Physica* **1951**, *17*, 612.

[65] T. G. S. M. Rijks *et al.*, *Phys. Rev. B* **1995**, *51*, 283.

[66] N. F. Mott, *Proc. Phys. Soc. Lond.* **1935**, *47*, 571.

[67] N. F. Mott, *Proc. R. Soc. London Ser. A* **1936**, *153*, 699.

[68] *Relaxation in Magnetic Materials for Spintronics, in: Handbook of Nanomagnetism*, (Eds.: C. Mewes, T. Mewes), Pan Stanford, **2015**, p. 74.

[69] B. Hillebrands, K. Ounadjela, *Spin Dynamics in Confined Magnetic Structures I*, Springer Berlin Heidelberg, **2003**.

[70] L. D. Landau, E. Lifshitz, *Phys. Z. Sowjetunion* **1935**, *8*, 101.

[71] J. Mallinson, *IEEE Trans. Magn.* **1987**, *23*, 2003.

[72] B Heinrich, J. F. Cochran, *Adv. Phys.* **1993**, *42*, 523.

[73] M. Lines, A. Glass, *Principles and Applications of Ferroelectrics and Related Materials*, OUP Oxford, **1977**.

[74] Y. Xu, *Ferroelectric Materials and Their Applications*, Elsevier Science, **2013**.

[75] P. Chandra, P. B. Littlewood in *Physics of Ferroelectrics: A Modern Perspective*, Springer Berlin Heidelberg, Berlin, Heidelberg, **2007**, p. 69.

[76] A. Zeleny, J. Valasek, *Phys. Rev.* **1934**, *46*, 450.

[77] J. Valasek, *Physical Review* **1921**, *17*, 475.

[78] S. R. Miller *et al.*, *Phys. Rev.* **1962**, *126*, 528.

[79] A. Sawada, Y. Takagi, *J. Phys. Soc. Jpn.* **1972**, *33*, 1071.

[80] R. S. PEASE, G. E. BACON, *Nature* **1954**, *173*, 443.

[81] F. Y. Wu, *Phys. Rev.* **1968**, *168*, 539.

[82] L. Landau, *Z. Sowjetunion* **1937**, *11*, 26.

[83] L. Landau, *Z. Sowjetunion* **1937**, *11*, 545.

[84] V. L. Ginzburg, *Zh. Eksp. Teor. Fiz.* **1945**, *15*, 739.

[85] V. L. Ginzburg, *Zh. Eksp. Teor. Fiz.* **1949**, *19*, 36.

[86] A. Devonshire, *Lond. Edinb. Dubl. Phil. Mag.* **1949**, *40*, 1040.

[87] A. Devonshire, *Lond. Edinb. Dubl. Phil. Mag.* **1951**, *42*, 1065.

[88] F. Heusler, *Verh. der Deutsch. Phys. Ges.* **1903**, *5*, 220.

[89] F. Heusler, *Verh. der Deutsch. Phys. Ges.* **1903**, *5*, 219.

[90] A. J. Bradley, J. W. Rodgers, *Proc. R. Soc. London Ser. A* **1934**, *144*, 340.

[91] O Heusler, *Ann. Phys. (Leipzig)* **1934**, *411*, 155.

[92] S. Wurmehl *et al.*, *Phys. Rev. B* **2005**, *72*, 184434.

[93] H. Luo *et al.*, *J. Phys. D: Appl. Phys.* **2007**, *40*, 7121.

[94] T Graf, C Felser, S. S. P. Parkin, *Prog. Solid. State. Ch.* **2011**, *39*, 1.

[95] M. Meinert *et al.*, *Phys. Rev. B* **2012**, *86*, 245115.

[96] H. C. Kandpal, G. H. Fecher, C. Felser, *J. Phys. D: Appl. Phys.* **2007**, *40*, 1507.

[97] T. Wolfram, S. Ellialtioglu, *Electronic and Optical Properties of d-Band Perovskites*, Cambridge University Press, **2006**.

[98] B. Sanyal, O. Eriksson, *Advanced Functional Materials: A Perspective from Theory and Experiment*, Elsevier Science, **2012**.

[99] V. M. Goldschmidt, *Naturwissenschaften* **1926**, *14*, 477.

[100] N. F. Atta, A. Galal, E. H. El-Ads, *Perovskite Materials - Synthesis, Characterisation, Properties, and Applications*, **2016**.

[101] F. Kubel, H. Schmid, *Acta Crystallogr. Sec. B* **1990**, *46*, 698.

[102] J.-G. Park *et al.*, *J. Phys. Condens. Matter* **2014**, *26*, 433202.

[103] L. M. Volkova, D. V. Marinin, *J. Supercond. Nov. Magn.* **2011**, *24*, 2161.

[104] G. Catalan, J. F. Scott, *Adv. Mater.* **2009**, *21*, 2463.

[105] F. I. C. f. Cockrell School of Engineering, Tolerance Factor Calculator, `http://www.me.utexas.edu/~benedekgroup/ToleranceFactorCalculator/` (visited on 09/01/2016).

[106] J. Moreau *et al.*, *J. Phys. Chem. Solids* **1971**, *32*, 1315.

[107] M. Graf *et al.*, *Phys. Rev. B* **2014**, *90*, 184108.

[108] D. C. Arnold *et al.*, *Phys. Rev. Lett.* **2009**, *102*, 027602.

[109] A. Stroppa, S. Picozzi, *Phys. Chem. Chem. Phys.* **2010**, *12*, 5405.

[110] S. V. Kiselev, R. P. Ozerov, G. S. Zhdanov, *Sov. Phys. Dokl.* **1963**, *7*, 742.

[111] G. A. Smolenski, I. E. Chupis, *Sov. Phys. Uspekhi* **1982**, *25*, 475.

[112] I Sosnowska, T. P. Neumaier, E Steichele, *J. Phys. C* **1982**, *15*, 4835.

[113] R. Przeniosło, M. Regulski, I. Sosnowska, *J. Phys. Soc. Jpn.* **2006**, *75*, 084718.

[114] L. W. Martin *et al.*, *J. Phys. Condens. Matter* **2008**, *20*, 434220.

[115] C. Ederer, N. A. Spaldin, *Phys. Rev. B* **2005**, *71*, 060401.

[116] J. T. Heron *et al.*, *Phys. Rev. Lett.* **2011**, *107*, 217202.

[117] D. Treves, *Phys. Rev.* **1962**, *125*, 1843.

[118] R. D. Lock, J. M. Lucas, *J. I. Electron Rad. Eng.* **1972**, *42*, 435.

[119] C. Chen, *Magnetism and Metallurgy of Soft Magnetic Materials*, Dover Publications, **2013**.

[120] J. W. Seo *et al.*, *J. Phys. Condens. Matter* **2008**, *20*, 264014.

[121] K. K. Bhargav, S. Ram, S. B. Majumder, *J. Appl. Phys.* **2014**, *115*, 204109.

[122] I. S. Lyubutin, T. V. Dmitrieva, A. S. Stepin, *J. Exp. Theor. Phys.* **1998**, *88*, 590.

[123] W. Koehler, E. Wollan, *J. Phys. Chem. Solids* **1957**, *2*, 100.

[124] A. Scholl *et al.*, *Science* **2000**, *287*, 1014.

[125] L. Spieß, *Röntgendiffraktometrie für Materialwissenschaftler, Physiker und Chemiker*, ger, Teubner, Wiesbaden, **2005**, XII, 523 S. : Ill., graph. Darst.

[126] B. Cullity, S. Stock, *Elements of X-ray Diffraction*, Prentice Hall, **2001**.

[127] H Kiessig, *Ann. Phys. (Leipzig)* **1931**, *402*, 769.

[128] L. G. Parratt, *Physical Review* **1954**, *95*, 359.

[129] J. W. Criss, L. S. Birks, *Anal. Chem.* **1968**, *40*, 1080.

[130] S. Khim, *Izv. Akad. Nauk Kaz. SSR* **1966**, *3*, 97.

[131] J. Stöhr, H. Siegmann, *Magnetism: From Fundamentals to Nanoscale Dynamics*, *Vol. 152*, Springer, **2006**.

[132] J. C. Lang, *X-ray Magnetic Circular Dichroism*, John Wiley & Sons, Inc., **2002**.

[133] Y. Idzerda *et al.*, *Nuclear Instruments and Methods in Physics Research Section A: Accelerators Spectrometers Detectors and Associated Equipment* **1994**, *347*, 134.

[134] M Kallmayer *et al.*, *J. Phys. D: Appl. Phys.* **2007**, *40*, 1552.

[135] B. T. Thole *et al.*, *Phys. Rev. Lett.* **1992**, *68*, 1943.

[136] P. Carra *et al.*, *Phys. Rev. Lett.* **1993**, *70*, 694.

[137] P Kuiper *et al.*, *Phys. Rev. Lett. Letters* **1993**, *70*, 1549.

[138] A. Hubert, R. Schäfer, *Magnetic Domains: The Analysis of Magnetic Microstructures*, Springer, **1998**.

[139] R. Schäfer, *Investigation of Domains and Dynamics of Domain Walls by the Magneto-optical Kerr-effect*, John Wiley & Sons, Ltd, **2007**.

[140] J. K. LL.D., *Philos. Mag.* **1877**, *3*, 321.

[141] W. Voigt, *Handbuch der Elektrizität und des Magnetismus, Magnetooptik, ed. by L. Graetz, Vol. IV*, Johann Ambrosius Barth, Leipzig., **1920**.

[142] M. Freiser, *IEEE Trans. Magn.* **1968**, *4*, 152.

[143] R. Atkinson, P. H. Lissberger, *Appl. Opt.* **1992**, *31*, 6076.

[144] H Suhl, *Physical Review* **1955**, *97*, 555.

[145] C. Kittel, *Phys. Rev.* **1948**, *73*, 155.

[146] X Liu, Y Sasaki, J. K. Furdyna, *Phys. Rev. B* **2003**, *67*, 205204.

[147] B Heinrich, J. F. Cochran, R Hasegawa, *J. Appl. Phys.* **1985**, *57*, 3690.

[148] H Lee *et al.*, *J. Phys. D: Appl. Phys.* **2008**, *41*, 215001.

[149] R. D. McMichael, D. J. Twisselmann, A. Kunz, *Phys. Rev. Lett.* **2003**, *90*, 227601.

[150] Y. Kasatani *et al.*, *Appl. Phys. Express* **2014**, *7*, 123001.

[151] G. M. Müller *et al.*, *Nature Materials* **2009**, *8*, 56.

[152] C Liu *et al.*, *Appl. Phys. Lett.* **2009**, *95*, 022509.

[153] Y. Cui *et al.*, *Appl. Phys. Lett.* **2013**, *102*, 162403.

[154] Y. Cui *et al.*, *J. Appl. Phys.* **2014**, *116*, 073902.

[155] H Lee *et al.*, *Appl. Phys. Lett.* **2009**, *95*, 082502.

[156] P Landeros, R. E. Arias, D. L. Mills, *Phys. Rev. B* **2008**, *77*, 214405.

[157] M. J. Hurben, C. E. Patton, *J. Appl. Phys.* **1998**, *83*, 4344.

[158] R. D. McMichael, M. D. Stiles, P. J. Chen, *J. Appl. Phys.* **1998**, *83*, 7037.

[159] G Woltersdorf, B Heinrich, *Phys. Rev. B* **2004**, *69*, 184417.

[160] I. Barsukov *et al.*, *Phys. Rev. B* **2012**, *85*, 014420.

[161] N. Pachauri *et al.*, *J. Magn. Magn. Mater.* **2016**, *417*, 137.

[162] M Hashimoto *et al.*, *Appl. Phys. Lett.* **2005**, *87*, 102506.

[163] M Rickart *et al.*, *J. Phys. D: Appl. Phys.* **2005**, *38*, 1047.

[164] M. Rickart *et al.*, *Phys. Rev. B* **2004**, *70*, 060408.

[165] W Eerenstein, N. D. Mathur, J. F. Scott, *Nature* **2006**, *442*, 759.

[166] Y. U. Idzerda *et al.*, *Nucl. Instrum. Methods Phys. Res. Sect. A* **1994**, *347*, 134.

[167] H. Béa *et al.*, *Phys. Rev. B* **2006**, *74*, 020101.

[168] C. P. Hunt, B. M. Moskowitz, S. K. Banerjee, *Magnetic Properties of Rocks and Minerals. Rock Physics & Phase Relations: A Handbook of Physical Constants*, *Vol. 3*, Wiley Online Library, **1995**, p. 189.

[169] H. Béa *et al.*, *Appl. Phys. Lett.* **2006**, *89*, 242114.

[170] M. Meinert *et al.*, *Phys. Rev. B* **2015**, *92*, 144408.

[171] M. J. Carey, N Smith, B. A. Gurney, *J. Appl. Phys.* **2001**, *89*, 6579.

[172] J Dho, M. G. Blamire, *J. Appl. Phys.* **2009**, *106*, 073914.

[173] H. W. Chang *et al.*, *J. Appl. Phys.* **2012**, *111*, 07B105.

[174] M. Pires *et al.*, *J. Magn. Magn. Mater.* **2011**, *323*, 789.

[175] C. Hou *et al.*, *Phys. Rev. B* **2000**, *63*, 024411.

[176] A. K. Fischer, *The Journal of Chemical Physics* **1966**, *45*, 375.

[177] J. P. Nozières *et al.*, *J. Appl. Phys.* **2000**, *87*, 3920.

[178] D. M. Ceatano *et al.* in 11th European Conference on Non-Destructive Testing (ECNDT 2014), **2014**.

[179] D. Ebke *et al.*, *Appl. Phys. Lett.* **2006**, *89*, 162506.

[180] A. Niesen *et al.*, *J. Appl. Phys.* **2015**, *118*, 243904.

[181] C.-H. Yang *et al.*, *Nature materials* **2009**, *8*, 485.

[182] G. Koster *et al.*, *Rev. Mod. Phys.* **2012**, *84*, 253.

[183] J. K. Sinha, *J. Sci. Instrum.* **1965**, *42*, 696.

[184] C. Suryanarayana, A. Inoue, *Bulk Metallic Glasses*, CRC Press, **2011**.

[185] S. Plimpton, *J. Comput. Phys.* **1995**, *117*, 1.

[186] A. Greer, Y. Cheng, E. Ma, *Mater. Sci. Eng. R-Rep.* **2013**, *74*, 71.

[187] C. A. Schuh, T. C. Hufnagel, U. Ramamurty, *Acta Mater.* **2007**, *55*, 4067.

[188] D. C. Hofmann *et al.*, *Nature* **2008**, *451*, 1085.

[189] C. Fan, R. T. Ott, T. C. Hufnagel, *Appl. Phys. Lett.* **2002**, *81*, 1020.

[190] J. Qiao, H. Jia, P. K. Liaw, *Materials Science and Engineering: R: Reports* **2016**, *100*, 1.

[191] C. C. Hays, C. P. Kim, W. L. Johnson, *Phys. Rev. Lett.* **2000**, *84*, 2901.

[192] W. Guo *et al.*, *Acta Mater.* **2014**, *80*, 94.

[193] A. Donohue *et al.*, *Appl. Phys. Lett.* **2007**, *91*, 241905.

[194] J.-Y. Kim, D. Jang, J. R. Greer, *Adv. Funct. Mater.* **2011**, *21*, 4550.

[195] J. Zhang *et al.*, *Acta Mater.* **2012**, *60*, 7183.

[196] Y. Wang *et al.*, *Proc. Natl. Acad. Sci. USA* **2007**, *104*, 11155.

[197] ASTM Standard Test Method E 384 "Standard Test Method for Mircohardness of Materials", ASTM Annual Book of Standards, Vol. 03.01, Philadelphie, PA, 1993, **1993**.

[198] X. Li, B. Bhushan, *Mater. Charact.* **2002**, *48*, 11.

[199] M. Mendelev *et al.*, *Philos. Mag.* **2009**, *89*, 967.

[200] C. Deng, C. A. Schuh, *Appl. Phys. Lett.* **2012**, *100*, 251909.

[201] C. Schuh, T. Nieh, *Journal of Materials Research* **2011**, *19*, 46.

[202] F. Shimizu, S. Ogata, J. Li, *Mater. Trans.* **2007**, *48*, 2923.

[203] F. Spaepen, *Acta Metall.* **1977**, *25*, 407.

[204] N. Wang, F. Yan, L. Li, *J. Non-Cryst. Solids* **2015**, *428*, 146.

C Publications and Conferences

Publications

- 08/2016 **C. Sterwerf**, S. Paul, B. Khodadadi, M. Meinert, J. Schmalhorst, M. Buchmeier, C. K. A. Mewes, T. Mewes, G. Reiss, "Low Gilbert damping in Co_2FeSi and Fe_2CoSi films", Journal of Applied Physics, 120(8), 083904 (2016)
- 07/2016 **C. Sterwerf**, M. Meinert, E. Arenholz, J. Schmalhorst, G. Reiss, "Room temperature exchange bias in $BiFeO_3$ / Co-Fe bilayers", IEEE Transactions on Magnetics, 52(7), 4800204 (2016)
- 07/2016 **C. Sterwerf**, T. Kaub, C. Deng, G. B. Thompson, L. Li, "Deformation mode transitions in amorphous - Cu45Zr55/crystalline - Cu multilayers", submitted to Thin Solid Films (2016)
- 07/2016 A. Niesen, **C. Sterwerf**, M. Glas, J. Schmalhorst, G. Reiss, "Structural, magnetic and electrical properties of sputter deposited Mn-Fe-Ga thin films", IEEE Transactions on Magnetics, 52(7), 2600404 (2016)
- 03/2014 M. Veis, L. Beran, R. Antos, D. Legut, J. Hamrle, J. Pistora, **C. Sterwerf**, M. Meinert, J. Schmalhorst, T. Kuschel, "Magneto-optical spectroscopy of Co_2FeSi Heusler compound", Journal of Applied Physics 115(17), 17A927 (2014)

- 11/2013 M. Glas, **C. Sterwerf**, J. Schmalhorst, D. Ebke, C. Jenkins, E. Arenholz, G. Reiss, "X-ray absorption spectroscopy and magnetic circular dichroism studies of $L1_0$- Mn-Ga thin films", Journal of Applied Physics, 114(18), 183910 (2013)
- 07/2013 **C. Sterwerf**, M. Meinert, J. Schmalhorst, G. Reiss, "High TMR ratio in Co_2FeSi and Fe_2CoSi based magnetic tunnel junctions", IEEE Transactions on Magnetics, 49(7), 4386 (2013)
- 11/2012 J. Rogge, P. Hedwig, **C. Sterwerf**, A. Hütten, "Co_2FeSi based magnetic tunnel junctions with BaO barrier", IEEE Transactions on Magnetics, 48(11), 3825 (2012)

Conference Contributions

- 03/2012 Poster at the DPG Frühjahrstagung 2012 in Berlin
- 01/2013 Poster at the 12th Joint MMM/Intermag Conference 2013 in Chicago, IL, USA
- 03/2013 Talk at the DPG Frühjahrstagung 2013 in Regensburg
- 03/2014 Talk at the DPG Frühjahrstagung 2014 in Dresden
- 03/2015 Talk at the DPG Frühjahrstagung 2015 in Berlin
- 01/2016 Talk at the 13th Joint MMM/Intermag Conference 2016 in San Diego, CA, USA

D Acknowledgements

First of all, I would like to express my gratitude to my advisor Prof. Dr. Günter Reiss for allowing me to work in his laboratory, as well as reviewing and supervising my thesis. His sincere guidance helped me throughout my research and the writing of this thesis. I also want to thank Dr. Jan Schmalhorst and Jun.-Prof. Dr. Markus Meinert for their encouragement and their insightful comments. My sincere thanks to all present and past members of the Center for Spinelectronic Materials and Devices for sharing their knowledge and a pleasant working atmosphere.

Moreover, I want to express my thanks to Dr. Karsten Rott, for maintaining the lab equipment as well as for his support and expertise in technical questions. Without his helpful advice it would not be possible to conduct this research. Furthermore, I would like to thank Aggi Windmann for the settlement of formalities.

I would like to acknowledge the opportunity to work at the Advanced Light Source[1] in Berkeley, CA, USA, and thank Dr. Elke Arenholz for her support while there.

A special mention goes to my colleagues and friends: Dr. Alexander Böhnke, Lars Helmich, Alessia Niesen, Dr. Manuel Glas, Dr. Daniel Meier, Dr. Christoph Klewe, Marianne Bartke, and Dr. Niclas Teichert for a great working atmosphere.

Furthermore, I express my gratitude to Dr. Tim Mewes and Dr. Gregory B. Thompson from the MINT Center and the Department of Metallurgical and Materials Engineering for the opportunity to participate in the MINT

[1]The Advanced Light Source is supported by the Director, Office of Science, Office of Basic Energy Sciences, of the U.S. Department of Energy under Contract No. DE-AC02-05CH11231.

Center summer school at the University of Alabama, Tuscaloosa, AL, USA in 2014. I would like to thank my colleagues in Tuscaloosa for their hospitality, the positive atmosphere, and the good collaboration.

Last but not the least, I want to express my very profound gratitude to my friends and family for their faith and support. This accomplishment would not have been possible without them. Thank you.